Understanding the Interaction of Bacteria, Algae, and Biomolecules at Electrode Surfaces

By

Meng-Hsuan Lin

B.S, Chung Yuan Christian University

M.S, National Yang Ming University

THESIS

Submitted in partial fulfilment of the requirements for the degree of Doctor of Philosophy in

Chemical Engineering in the Graduate College of the

University of Illinois at Chicago, 2020

Chicago, Illinois

Defense Committee:

Dr. Brian P. Chaplin, Chair and Advisor, Department of Chemical Engineering
Dr. Gang Cheng, Department of Chemical Engineering
Dr. Shafigh Mehraeen, Department of Chemical Engineering
Dr. Vivek Sharma, Department of Chemical Engineering
Dr. Ian Papautsky, Richard and Loan Hill Department of Bioengineering

This thesis work is dedicated to my families, who have always stood by my side during the challenges of graduate school and life with their unconditional loves and supports.

ACKNOWLEDGEMENTS

I am very privileged to have the opportunity to pursue my Ph.D. degree at a university as friendly, diverse and collaborative as the University of Illinois at Chicago (UIC). As a first generation college graduate in a middle-class family with a grandmother raised during the Japanese colonial period, who believed higher education and expressing personal opinions were unnecessary for girls, I knew my parents worked hard to provide my sisters and I a childhood they did not have. After finishing my masters, I blindsided them by preparing and applying for international Ph.D. programs. Initially, they were reluctant with the decision until several passionate discussions happened. During these years, I sincerely appreciate their unconditional supports, loves and encouragement. They are my rock emotionally and financially; they listen my struggles, keep my optimistic attitude going and try to pick me up every time when I feel down.

I would like to express my gratitude and appreciation to my advisor, **Dr. Brian P. Chaplin** for having me in his lab, providing his guidance and supporting my studies over the years. As an advisor, water science expert and educator, Dr. Chaplin is a rigorous researcher, a problem solver, a precise writer, and a communicator. Under his guidance, I have learned how to perform research as a scientist and realized that I can always do better and think deeper while solving problems. Beyond that, he may or may not know that he reshaped me as a person, encouraging my personal growth not only for hard skills but also soft skills. I might have frustrated him the most during these years, but I sincerely appreciate his consistent challenges and patience.

I would also like to thank my thesis committee members, **Dr. Gang Chang, Dr. Ian Papautsky, Dr. Shafigh Mehraeen and Dr. Vivek Sharma** for their valuable time, meaningful suggestions, constructive comments and critical insights. My gratitude is extended for their advise on research and course works.

Over the years, **Yin Jing** had impact by assisting me to build up fundamental knowledge in research and also personal suggestions to build up my life in Chicago. I would also like to thank my friends who walk with me on this track and encourage each other. **Samuel T. Plunkett,** as a friend and lab member**,** has given his time to discuss research, course work, coffee breaks and summer tennis in order to keep each other on track for our individual research goals. **Chang Liu, Huifeng Wang, Tongshuai Wang, Aaditya Pendse** and I have encouraged each other during our challenging graduate school lives. Importantly, thanks to previous lab members and undergraduates, **Lun Guo, Pralay Gayen, Sasmita Nayak, Saurabh Misal, Raquel Malerba, Nina Jasmine Malapit, Jenine Agoncillo, Mark Sovereign and Claudia Cerna** who I have enjoyed working with and learning from. I thank them for sharing hard work and gratitude all the time. Also thanks to **Nabil Shaikh, Suzane Carneiro, Shirin Saffar, Soroush Almassi, Yusra Khalid, and Thi Xuan Huong Le** for their supports.

I extend my deepest thanks to my extended families and **Jason V. Spataro** for walking besides me, dealing with my unstable mental/psychological issues during the journey and bringing me positive energy through grandma's cookie baking with coffee and Spargas pizza/pasta.

Finally, I would like to acknowledge the support from the National Science Foundation for funding my research projects and conference expenses. Without this funding, my Ph.D. research would likely not be a possible.

CONTRIBUTION OF AUTHORS

Chapter 1 represents an overview of my dissertation, which also includes the research objectives and an overall outline of this dissertation. Chapter 2 is a literature review where the state of knowledge is presented and the significant research questions are highlighted. Chapter 3 includes a published work entitled "*Role of Near-Electrode Solution Chemistry on Bacteria Attachment and Poration at Low Applied Potentials"* published in *Environmental Science and Technology*, which I was the first author and major contributor of the research. Dr. Shafigh Mehraeen derived and coded the mathematical model, Dr. Gang Cheng gave guidance on bacteria related experiments, Dr. Cory Rusinek manufactured and provided the Boron-Doped Diamond (BDD) electrodes and Dr. Brian P. Chaplin conceived the project and contributed to the manuscript revision and scientific discussion. Extending the work from Chapter 3, Chapter 4 contains a published work entitled *"Bacteria poration on modified boron-doped diamond electrode surfaces induced by divalent cation chelation"* published in *Environmental Science Water Research & Technology*, which I was the first author and worked with the same group of co-authors as listed in Chapter 3. Chapter 5 contains a manuscript entitled *"Chlorinated Byproduct Formation during the Electrochemical Advanced Oxidation Process at Magnéli Phase Ti_4O_7 Electrodes"* that is under review at *Environmental Science and Technology*, which I was the first author and major contributor. Devon Manley Bulman and Dr. Christina K. Remucal performed the LC-MS measurements and analysis for chlorinated and organic byproducts. Dr. Brian P. Chaplin conceived the project, contributed to the manuscript revision and scientific discussion. Chapter 6 contains a study focused on *anodic potential effect of algae photosynthetic activity* which I was the first author and major contributor of the research. Dr. Gang Cheng provided access to his microscope and Dr. Brian P. Chaplin conceived the project and contributed to the manuscript revision and

scientific discussion. Chapter 7 contains major conclusions of the dissertation and the future directions of this field are also discussed.

TABLE OF CONTENT

LIST OF FIGURES

LIST OF TABLES

LIST OF ABBREVIATIONS

BDD	Boron-Doped Diamond
COD	Chemical Oxygen Demand
CV	Cycle Voltammetry
$Cl^{\bullet}$	Chlorine Radical
DBPs	Disinfection Byproducts
DFT	Density Functional Theory
EAOP	Electrochemical Advanced Oxidation Process
EDTA	Ethylenediaminetetraacetate
EO	Electro-Oxidation
H_2O_2	Hydrogen Peroxide
IrO_x	Iridium Oxide
LPS	Lipopolysaccharide
LC-MS	Liquid Chromatography–Mass Spectrometry
MEAs	Microelectrode Arrays
MCL	Maximum Contaminant Level
MCLG	Maximum Contaminant Level Goal
$OH^{\bullet}$	Hydroxyl Radical
OTE	Optical Transparent Electrode
OCP	Open Circuit Potential
POA1	Pseudomonas Aeruginosa
REM	Reactive Electrochemical Membrane
ROS	Reactive Oxygen Species
SECM	Scanning Electrochemical Microscopy
NOM	Natural Organic Matter
UME	Ultramicroelectrode
US EPA	US Environmental Protection Agency

XPS	X-ray Photoelectron Spectroscopy
XRD	X-ray Powder Diffraction

SUMMARY

This dissertation focused on understanding the mechanisms of biofouling control, chlorinated byproduct formation and algae photosynthetic activity at electrode surfaces as a function of electrode potential and solution conditions. Specific goals of this work were to 1) elucidate mechanisms of microorganism poration and attachment on conductive boron-doped diamond (BDD) and modified BDD surfaces, 2) develop micro-scale analytical techniques to study near surface chemistry and their effect on microorganism poration/attachment, 3) study organic and inorganic chlorinated byproduct formation during the electrochemical advanced oxidation process at Magnéli phase Ti_4O_7 electrodes, and 4) investigate the effect of anodic potentials on microalgae photosynthetic activity at modified BDD surfaces.

These goals were accomplished through a combination of carefully designed experimental analysis and theoretical techniques. For microorganism related studies, a IrO_x ultramicroelectrode (UME) was fabricated and scanning electrochemical microscopy (SECM) was used to study the real-time near surface solution pH and reactive oxygen species (ROS) detection and use this information to interpret electrode-mediated bacteria inactivation. X-ray photo electron spectroscopy (XPS) was used to characterize surface modifications on the BDD electrodes. A mathematical reactive transport model was developed to interpret the SECM data for a better understanding of the near-electrode chemistry. Hydrogen peroxide (H_2O_2) was the primary oxidant formed under cathodic conditions, and a combination of H_2O_2, $Cl^{\bullet}$, $HO_2^{\bullet}$ $Cl_2^{\bullet-}$, and Cl_2 formation likely contributed to bacteria poration at potentials as low as 0.5 V vs Ag/AgCl. Compared to current proposed mechanisms of biofilm control with electrochemical methods, this study focused on low applied potentials (e.g., −0.2 to 1 V versus Ag/AgCl) on the electrode surface and real time

near surface measurements, which provided insights on the physicochemical properties of the initial stages of biofouling control.

Chelation-induced biofilm control has also been studied in a solution phase for destabilization bacteria and reducing their viability. Chelators show a significant impact for antibacterial purposes by extracting divalent ions (Mg^{2+} and Ca^{2+}) from the lipopolysaccharides (LPS) of the cell membrane. Based on the first study, the BDD surface was modified with an N-propyl-2-hydroxyacetamide group, which provided a surface with chelation ability for biofilm control. In this study, Pseudomonas aeruginosa (PAO1) was used as a model pathogenic organism and low potentials (e.g., −0.2 to 1 V versus Ag/AgCl) were applied on the electrodes. Results suggested that divalent ions from the outer membrane of PAO1 were chelated by N-propyl-2-hydroxyacetamide functional groups that were immobilized on a BDD optically transparent electrode (termed OH-BDD/OTE). Two- to three-fold higher percentage of porated bacteria were observed on the OH-BDD/OTE compared with BDD/OTE under applied anodic potentials between 0.1 to 0.5 V vs. Ag/AgCl. Zeta potential measurements of the PAO1 bacteria as a function of chelators and Mg^{2+} concentrations were performed to support the chelation hypothesis. A mathematical model was built on the nonlinear Poisson–Boltzmann equation to interpret experimental data.

Natural organic matter (NOM) is also commonly found in surface and ground waters, as a result of a complex matrix of organic substances combining different hydrological, biological and geological interactions. Phenolic compounds play a central role in the structure of NOM and many industrial contaminants present in natural waters. NOM can react with chlorine and form halogenated byproducts which can contaminate drinking water and increase documented health risks, such as bladder cancer and birth defects. Electrochemical advanced oxidation processes

(EAOPs) have recently been studied as possible new modular technologies for water treatment. In our study, resorcinol was used as a model organic compound, and it was oxidized in the presence of varying concentrations (1 and 5 mM) of sodium chloride (NaCl) and as a function of electrode potential. A Magnéli phase Ti_4O_7 electrode was used as a reactive electrochemical membrane (REM) and characterized by X-ray diffraction (XRD). Electro-oxidation was performed using a flow-through electrochemical cell with the presence of NaCl and resorcinol under a constant flow rate and different electrode potentials. High-performance liquid chromatography (HPLC), ionic chromatography (IC) and liquid chromatography–mass spectrometry (LC-MS) were used to determine the possible inorganic, organic and chlorinated byproducts. Furthermore, the chlorinated byproducts were proposed based on the chromatography results and density functional theory (DFT) simulations.

For the fourth study, microalgae photosynthetic response under applied anodic potentials were investigated. Microalgae are a microorganism which can be harvested as a promising source for green energy but harmful for water systems. Electrochemical methods have been studied for algae inhibition under anodic current densities (e.g. 10 mA/cm^2) for water purification purposes. Moreover, anodic oxidation process has been studied for lipid extraction for biofuel production. Applied anodic potentials might have an impact on microalgae photosynthetic ability and viability during the harvesting process. Hence, monitoring microalgae photosynthetic activity provides the insight for a comprehensive understanding of the correlation between electrode potentials and algae viability. The modified BDD used in the first study (APTES-BDD/OTE) was used as a conductive electrode for algae attachment. SECM was used for surface mapping and measuring algae photosynthetic activity using soluble redox couples as electron shuttles. Photosynthetic activity was measured as a function of the anodic potentials on the electrode.

In summary, work from this dissertation advanced knowledge in the area of biological/electrode interactions with respect to water treatment applications. For biofilm control at the electrode surfaces, results indicated that applied potentials can caused H_2O_2 and Cl-based oxidants formation at the electrode surface which contributed to bacterial poration. Moreover, electrode modification may be a viable method to prevent biofouling of electrode surfaces that are operated at low applied potentials. The formation of Cl-based oxidants and $OH^{\bullet}$ at the electrode surface can react with organic contaminants and form halogenated byproduct during EAOPs. Results indicated that chlorinated byproducts should be carefully monitored during EAOPs and multi-barrier treatment approaches are likely necessary to prevent halogenated byproducts in the treated water. In addition, photosynthetic activity measurement gives insights for monitoring algae harvesting, biomass separation and cell treatment processes for biofuel production by reactive electrochemical membrane.

1. Introduction

1.1 Background

The interaction between microorganisms and surfaces has become a focal point of scientific investigations in both natural and engineered settings. For example, bacteria can often have negative impacts in several industries, such as water treatment and distribution, food and beverage processing, cooling towers, and medical device implants [1]. These industries spend significant time and resources to combat the growth of biofilms on pipes, heat exchangers, membranes, medical tools and implants, and other surfaces [1–3]. In addition, the control of biofouling or the treatment of water containing biomolecules often results in toxic byproduct formation, which is especially problematic for drinking water treatment. The beneficial use of biological organisms also demands a greater understanding of their interaction with surfaces. For example, algae are currently used as a precursor to biofuel production, where their separation from aqueous streams is necessary. Given the array of situations directly or indirectly affected by microbiological species, a deeper understanding of the mechanisms of microbial attachment and inactivation are needed, so that strategies can be developed to prevent or control the biofouling of surfaces and to properly utilize them as a resource.

Microorganism attachment to surfaces is a two phases process. The initial step involves adhesion, which is a rapid and reversible process. It is primarily driven by physicochemical interactions that consist of hydrophobic, hydrodynamic, and electrostatic interactions. Generally, organisms move to a surface due to Brownian motion, van der Waals attraction, or gravitational forces. The second step is irreversible attachment. This step is slower than the former and is driven by molecular-specific surface reactions that develop over time[4, 5]. To prevent bacteria adhesion, surface structure design [6, 7], polymer brush coatings [8], nanoparticle deposition (e.g., TiO_2,

ZnO and Ag) [7], and electrochemical techniques have been studied [7–10]. Electrochemical techniques offer economic and technical advantages over traditional methods, as chemical reagents are not needed for biofouling control. However, the mechanisms for bacteria inactivation on conductive surfaces under low applied potentials is not fully understood and represents a gap in understanding of biofouling control.

The reactive conditions that are present during electrochemical biofouling control or algae removal processes have the potential for toxic byproduct formation. Natural organic matter (NOM), which refers to a wide spectrum of biologically-derived compounds, is found in all natural waters and is abundant in biological feedstocks. NOM is generally non-toxic at low concentrations, but its reaction with disinfectants or other halogen ions has been shown to form toxic halogenated byproducts, which can increase risk of cancer or cause liver, kidney or central nervous system problems [13–16]. Also, the USEPA has set maximum contaminant levels (MCLs) in drinking water for trihalomethanes (THMs) and haloacetic acids (HAAs) at a combined concentration of 80 $\mu g\ L^{-1}$ for four regulated THMs and 60 $\mu g\ L^{-1}$ for five regulated HAAs. Recent work has shown the EAOPs result in removing various organic contaminants with high rate constants and low energy consumption [17–20]. However, work has not yet been done to establish the potential for halogenated byproduct formation of Ti_4O_7 electrodes during their use in EAOPs. Therefore, a goal of this dissertation was to investigate both inorganic and organic chlorinated byproduct formation during EAOPs using Ti_4O_7 anodes.

Algae are a large and diverse group of photosynthetic aquatic organisms in nature which can convert solar energy into chemical energy and reduce CO_2. Bioelectricity can be directly extracted from the photosynthetic electron transport chain (photosystem I and II) before the algae convert CO_2 into polysaccharides (sugars) and triacylglycerides (fats) [21]. Also, these molecules

are the raw materials for producing bioethanol and biodiesel fuels [22]. Algae harvesting and biolipid extraction are important steps for biofuel production but these processes can be energy-intensive and time-consuming, which include mechanical and non-mechanical techniques [23], [24] . Algae blooms can also have ecological, aesthetic, and human health impacts if present in reservoirs, lakes, and streams [25]. Reactive electrochemical membranes are a possible filtration system that can simultaneously harvest and pretreat algae for lipid extraction [23]. Therefore, a deeper understanding of the impact of anodic potentials on algae photosynthetic activity is necessary.

1.2 Research Objectives

The overall goal of this research was to better understand the interactions of bacteria, algae, and biomolecules at electrode surfaces. Specifically, scanning electrochemical microscopy (SECM) techniques were developed to determine near surface pH, and ROS (O_2, H_2O_2, $HO^{\bullet}$) formation in the micrometer-scale range above the electrodes. Also, it was used for mapping the attached microalgae and for measurement of photosynthetic activity. Methodologies are presented that consist of experimental studies complemented by mathematical transport modeling and quantum chemical calculations. Moreover, biomolecule oxidation on the electrodes was studied and possible organic and inorganic byproducts were proposed according to chromatography analysis results and density functional theory (DFT) simulations. The specific research objectives are as follows:

1) *Determine the Mechanisms of Bacteria Inactivation and Attachment on the Conductive Electrodes at Low Applied Voltages*

Biofilm growth is of critical concern in drinking water systems which can affect the performance of water treatment membranes [20, 26] , capacitive deionization electrodes [27], and other treatment technologies. Moreover, it is also a significant health concern. Electrochemical techniques are effective biofouling control strategies compared with other traditional methods such as chemical sterilization [28, 29], surface modification [20, 30] or nanoparticle deposition [7], [31]. Although electrochemical methods have been studied to prevent bacteria attachment or inactivation [10, 32–34], the mechanisms for bacteria poration at low applied potentials are not clearly understood.

The objectives of this study were to investigate the mechanisms of bacteria poration at electrified interfaces at low applied potentials (<|1.0| V/Ag/AgCl) and provide insights into attachment and poration mechanisms. Optical transparent boron-doped diamond (BDD/OTE) and positively charged functionalized surfaces were fabricated. SECM was utilized to monitor the near-surface pH and formation of ROS resulting from electrochemical reactions. Moreover, mathematical modeling was used to interpret the experimental results based on the reaction-diffusion model. The model simulated the reaction of H_2O_2 and $Cl^{\bullet}$ and their diffusion between the electrode and UME tip surface under steady state conditions. Thus, the work in particular focused on bacteria inactivation and attachment on polarized electrode surfaces, and thus seeks to determine mechanisms responsible for inactivation of bacteria for applications related to biofouling control.

2) *Elucidate the mechanisms for bacteria poration at functionalized electrode surfaces as a function of electrode potential*

Extending work from *research objective 1,* an N-propyl-2-hydroxyacetamide group functionalized BDD optically transparent electrode (OH-BDD/OTE) was designed. However, use

of the OH-BDD/OTE resulted in a higher proportion of bacteria inactivation than the other OTEs under low applied potentials between -0.2 and 1.0 V vs. Ag/AgCl. For example, two- to three-fold higher percentage of porated bacteria were observed on the OH-BDD/OTE compared with BDD/OTE under applied anodic potentials between 0.1 to 0.5 V vs. Ag/AgCl. The results suggested that N-propyl-2-hydroxyacetamide groups provide distinct chelation sites on the OH-BDD/OTE that inactivated bacteria by extracting divalent ions from the cell membrane. Based on this hypothesis, DFT calculations indicated that the chelation mechanism was thermodynamically favorable. Also, both experimental studies and mathematical models were conducted to support this hypothesis. Zeta potential measurements were made during the addition of chelators to solution in the presence of different Mg^{2+} concentrations (i.e.,0–30 mM). Nonlinear Poisson–Boltzmann equation model was used to interpret the experimental results of cell surface charges and divalent ions binding sites. Results supported the chelation mechanism for bacteria poration, which indicates that electrode modification may be a viable method to prevent biofouling of electrode surfaces that are operated at low applied potentials.

3) *Chlorinated byproduct formation during the electrochemical advanced oxidation process at Magnéli Phase Ti_4O_7 electrodes*

Chemical disinfection (e.g. chlorine) is widely used for the provision of safe drinking water. Although it is effective for disinfection, byproducts are formed from reactions between the chemical oxidants and naturally occurring organic and inorganic precursors, such as NOM [35–37]. NOM can produce byproducts associated with unintended health consequences. Research has shown that hypohalous acids (chlorine, bromine, iodine) can react with NOM through oxidation reactions and form toxic byproducts [38].

Oxidant (e:g., HOCl) + Precursor (e:g:; NOM)→ Byproducts (e:g:; $CHCl_3$)

In this study, we simplify this relatively complex system by performing electrochemical oxidation experiments with a model organic compound (i.e., resorcinol) that contain key functional groups that are representative of NOM in the presence of chloride electrolytes, and byproduct formation were studied. BDD electrodes are currently considered to be the state-of-the-art electrode for water treatment for electrochemical advanced oxidation processes (EAOPs), because they generate high yields of $OH^{\bullet}$ and are corrosion resistant and commercially available [39, 40]. However, the application of BDD electrodes for treatment of chloride-containing waters results in the formation of THMs and HAAs byproducts, which EPA has set MCLs in drinking water of 80 μg L^{-1} for four regulated THMs and 60 μg L^{-1} for five regulated HAAs.

The primary objective of this work was to investigate both inorganic and organic chlorinated byproduct formation during EAOPs using a Magnéli phase Ti_4O_7 reactive electrochemical membrane (REM). Porous Magnéli phase Ti_4O_7 electrodes are high surface area, stable anode materials [44, 45] that are capable of direct oxidation of contaminants [43] and formation of $OH^{\bullet}$ [42]. Resorcinol was oxidized in the presence of NaCl (1 and 5 mM) as a function of electrode potential. Inorganic and organic byproduct formation was characterized using ion chromatography (IC) and liquid chromatography–mass spectrometry (LC-MS), respectively. The stability and probable fate of resorcinol and chlorinated byproducts were investigated using DFT methods. This work is the critical first step in understanding halogenated byproduct formation on Ti_4O_7 electrodes.

4) Evaluation of the effects of electrode potential on the photosynthetic activity of algae

Our previous work has resulted in the development of an innovative Ti_4O_7 REM filtration system for algae harvesting, separation and pretreatment for lipid extraction. This application can

be potentially used for biofuel production and biomass separation. The preliminary results suggested that anodic oxidation of algae using a Ti_4O_7 REM can increase the lipid extraction efficiency and prevent membrane fouling. However, reducing algae photosynthetic activity is possible after REM treatment. In addition, charge transfer from algae's photosynthetic transport chain to a soluble redox species provides the opportunity for determining algae viability [3, 6]. Of particular interest in the proposed work is the viability and photosynthetic ability of algae under conditions that are representative of electrochemical separation or treatment conditions. The overall objective of this research is to characterize the effects of a variety of electrode potentials pertinent to electrochemical algae biofuel separations and water treatment using SECM.

1.3 Outline

To better understand the interaction of bacteria, algae, and biomolecules at electrode surfaces, this dissertation consists of experimental studies that are complemented by mathematical transport modeling and quantum chemical calculations. The dissertation is organized as follows. **Chapter 2** summarizes the state of the art of knowledge of the interaction of biomolecules with electrode surfaces for environment applications. Specifically discussed are biofilm control methods, mechanisms of electrochemical disinfection method, application of SECM on microbiology and electrochemical advanced oxidation processes for water treatment. **Chapter 3** presents the work that was published in Environmental Science and Technology in 2020 entitled "*Role of Near-Electrode Solution Chemistry on Bacteria Attachment and Poration at Low Applied Potentials*" with co-authors Shafigh Mehraeen, Gang Cheng, Cory Rusinek, and Brian P. Chaplin. This paper addresses *research objective 1*, investigating the mechanisms of bacteria inactivation and attachment on conducive surfaces. Specifically, bacteria attachment and inactivation were investigated on optically transparent conductive electrodes and SECM was used to characterize

the near electrode surface chemistry. A reactive transport model was used to interpret and understand the near surface chemistry. **Chapter 4** contains a study that was published in The Royal Society of Chemistry, Environmental Science Water Research & Technology entitled "*Bacteria poration on modified boron-doped diamond electrode surfaces induced by divalent cation chelation*" with the same co-authors as Chapter 3. This paper addresses *research objective 2*, and uses the modified electrode developed in *research objective 1* to understand the mechanism of chelation effect on the electrode surface. Both experimental and theoretical methods were conducted to support the hypothesis of bacteria poration by the electrode functional groups. **Chapter 5** consists of a study "*Chlorinated Byproduct Formation during the Electrochemical Advanced Oxidation Process at Magnéli Phase Ti_4O_7 Electrodes"* with co-authors Devon Manley Bulman and Dr. Christina K. Remucal, which is under review at Environmental Science and Technology. This study addresses *research objective 3* and focuses on both organic and inorganic byproduct formation during electrochemical oxidation at Magnéli phase Ti_4O_7 electrodes, which includes DFT simulations that helped to interpret the experimental results. **Chapter 6** consists of an unpublished study "*Investigation the Effect of Microalgae Photosynthetic Activity under Different Anodic Potentials"* with co-authors Gang Cheng and Brian P. Chaplin. This study *addresses research objective 4.* SECM techniques were used for characterizing algae photosynthetic current responses under different anodic potentials. Specifically, the correlation between algae viability and photosynthetic activity with respect to the applied anodic potentials on the transparent conductive electrode were investigated. **Chapter 7** summaries the major findings of the dissertation and discusses future related research directions.

2. Literature Review

This chapter provides a review of published literature related to the interaction of biomolecules with electrode surfaces as it pertains to environment applications. Specifically, literature was reviewed on the electrochemical disinfection of microorganisms and biofilm control, electrochemical methods to measure protoplast photosynthetic activity, scanning electrochemical microscopy (SECM) application in microbiology, and organic/inorganic byproducts formation.

2.1 Electrochemical Disinfection of Microorganisms and Biofilm Control

Biofouling and biofilm formation have detrimental consequences in food processing [45], heat exchanger performance [46], ships hulls [47], medical device [48] and water treatment [3]. The formation of biofilms can adversely affect processes, health, safety and the equipment surfaces. Several strategies have been used for biofilm control, such as chemical agents (biocides and disinfectants) [29], antibiotics, and surface modification with polymers, nanoparticles, or the formation of composite membrane [8]. Pressure-driven membrane processes such as microfiltration (MF), ultrafiltration (UF), nanofiltration (NF) and reverse osmosis (RO) have been widely used for water treatment and desalination in past decades [7, 49]. However, these strategies are not ideal because of cell resistance to biocides and antibiotics [50], membrane fouling, and chemical agents toxicity to the environment risks [51]. Due to these limitations, an alternative microbial control strategy is needed to control this persistent issue. Factors influencing bacteria adhesion to surfaces are surficial chemical composition (surface hydrophobicity and charge), surface roughness, and environmental conditions (e.g., temperature, pH, flow conditions) [5].

Electrochemical techniques have promise for biofilm control on electrically conductive surfaces. The conductive surfaces act as an electrode and prevent or delay biofilm formation under

applied potentials or currents. Mechanisms for preventing biofilm formation using electrolysis methods can be summarized as follows: electric field effects [33, 34] electroporation [12, 32], electrostatic interaction [50, 52] between bacteria and surfaces, and reactive oxygen species (e.g. $^{\bullet}O_2^-$, H_2O_2, $^{\bullet}OH$) formation [10, 53]. The inhibition of microbial attachment on conductive surfaces under low-magnitude applied voltages has been previously investigated, and mechanisms responsible for preventing initial bacteria attachment have been proposed. Ronen et al. [10] proposed that hydrogen peroxide (H_2O_2) production cause cell apoptosis while the applied potentials are greater than 1 V v.s Ag/AgCl. Huo et al. [32] proposed that cell inactivation occurred on a carbon nanotube (CNT) sponge under an applied potential of 2 V/Ag/AgCl, due to an electric field enhancement by the nanoscopic topography of the CNT sponge, which caused E. coli cell membrane electroporation. The survival percentage of the bacteria on the CNT dropped to nearly 0% after 5 to 10 s of electrolysis time. Pandit et al. [33] mentioned that the high production of endogenous ROS affected the redox potential across the cell membrane and disrupted redox homeostasis, thereby inhibiting bacterial growth. They researched the mechanisms of Pseudomonas aeruginosa (POA1) biofilm formation on conductive surfaces with an applied voltage window ±|0.9| V/Ag/AgCl and noted that H_2O_2 generation might inhibit both planktonic and sessile communities of POA1 but ultimately had an insignificant effect on biofilm growth.

2.2 Impact of Chelator on Cell Membrane Destabilization

Chelators have been used in food, medical devices and water industries to prevent illnesses caused by bacteria and biofilm formation. Food-grade chelators such as citrate, phosphate, ethylene glycol-bis(β -aminoethyl ether)-N,N,N',N'-tetraacetic acid (EGTA), ethylenediaminetetra-acetate (EDTA), sodium lactate/bacteriocin and hexametaphosphate have been examined to overcome the penetration barrier in E. coli [54]. In addition, EDTA is a chelating

agent used wildly to lyse the cell outer membrane by removing either Ca^{2+}, Mg^{2+} or other divalent ions from the bacterial cell lipopolysaccharide (LPS) molecules and cause cell lysis or loss of viability [55, 56]. Studies have shown that gram-negative bacteria exposed to EDTA have increased permeability, released periplasmic enzymes, cell membrane associated proteins, and phospholipids [57, 58].

In addition, some mild acid based chelating agents (glycolic acid, gluconic acid, ethylenediaminetetraacetic acid, and citric acid) can also be used in the closed dyeing process of polyester fabrics with metal sensitive dispersive dye [59] for removing hardness of water by bonding with Ca^{2+} and Mg^{2+} ions and other heavy metal ions in hard water [60]. Glycolic acid is also one of the US food and drug administration (FDA) approved chelators for pharmaceutical used for inhibiting tyrosinase and inducing lamellar body secretion [61]. All chelators listed above have been utilized in the solution phases, but comprehensive considerations are still needed on their immobilization on surfaces/solid phases for further application purposes.

2.3 Disinfection Toxic By-Product Formation

Natural organic matter (NOM) is a complex matrix of organic substances commonly found in surface and ground waters via various biological, geological and hydrological cycles. The combination of climatic, hydrological, biological, geological and chemical factors were reported to be the main reasons for (1) the variations of NOM in water sources and (2) its increasing amounts recurrently monitored around the world during the past 10-20 years [62]. The NOM is nontoxic, but it could become a carrier of toxic organic and inorganic pollutants such as pesticides and radionuclides. Also, NOM can react with free chlorine disinfectants in conventional treatment to form trihalomethanes (THMs) and haloacetic acids (HAAs) which are regulated by U.S. Environmental Protection Agency (EPA) [63]. The EPA has set MCLs in drinking water for THMs

and HAAs at a combined concentration of 80 μg L^{-1} for 4 regulated THMs and 60 μg L^{-1} for 5 regulated HAAs [36].

Phenolic compounds play a central role in the structure of NOM with a broad spectrum of molecular weights, size distributions, functional groups, and substructures. Electrochemical advanced oxidation processes (EAOPs) have recently been investigated as novel modular technologies for water treatment and removal of algae, taste, odor and color. The mechanism of EAOPs involves the production of hydroxyl radicals ($OH^{\bullet}$) on stable anode materials. However, EAOPs may also occur indirectly through the formation of oxidants such as chlorine, hypochlorous acid, hypo- chlorite or hydrogen peroxide/ozone at the electrodes and have documented health risks. For example, boron-doped diamond (BDD) electrodes are currently considered to be the stable anode material for EAOPs, because they generate high yields of $OH^{\bullet}$ and are anodically stable, corrosion resistant, and commercially available [39, 40]. Even so, the application of BDD electrodes for the treatment of chloride-containing waters have resulted in the formation of both inorganic and organic chlorinated byproducts [38, 64–70], which have documented bladder cancer and birth defects [71, 72]. Due to the health concerns, careful monitoring of unintended byproducts that form during EAOPs are necessary so that appropriate treatment methods can be developed for a given water treatment application.

2.4 Algae Harvesting, Biolipid Extraction and Photosynthetic Electrons Evaluation

Algae are a large and diverse group of aquatic organisms harvested for their biomass as the feedstocks for biodiesel or biofuel production. Most species can convert solar energy into chemical energy in the form of polysaccharides (sugars) and triacylglycerides (fats) through photosynthesis. These molecules are the raw materials for producing bioethanol and biodiesel fuels. In our previous study [23], reactive electrochemical membranes (REM) are one of the filter systems for

simultaneous algae harvesting and pretreatment for lipid extraction. Reduced photosynthetic activity and oxygen production rates were the results of REM-treated algae. In addition, charge transfer from photosystems to the transport chain, especially charge extraction to an electron, support the need for potential applications in algae viability determination.

Quinones play a key role in fundamental biological processes as electron carriers in aerobic respiration (menaquinone or ubiquinone) or photosynthesis (plastoquinone). Recent studies have successfully shown the feasibility of harvesting the high energy photosynthetic electrons with electron mediator such as quinones, flavin mononucleotide (FMN) and phenazine methosulfate (PMS) [73]. Hydroquinone (HQ) is neutral and soluble in the cell membrane which allows it to shuttle electrons along the respiratory and photosynthetic chains. These properties allow quinones to be used as exogenous redox mediators in microbial applications to extract electrons from photosynthetic organisms [74], such as in protoplasts [69], isolated thylakoid membranes [75], isolated photosystem II complexes [76], or microbial metabolism [77]. P-benzoquinine (BQ) has been used to extract photosynthetic electrons from a single living protoplast by extracellular microelectrode measurement for quantitative investigation. Yasukawa et al. [78] reported that the carbon disk and gold (Au) disk microelecroedes can be used to monitor the localized concentrations of BQ and hydroquinone (HQ) on the cell under light irradiation. The results support that the BQ accepted two electrons from the photosynthetic respiratory electron transport chains (PSI and PSII) to form HQ. The electron transport can be monitored by reduction or oxidation current on the UME. Yue et al. [73] used different wavelengths of light as irradiation source and found that the thylakoids have the weakest response at wavelengths in the range 500-700 nm, which corresponds to green light. This finding indicates that the photocurrent indeed comes from the thylakoid membrane since the green color of most plants suggests the absence of

absorption of green light by the chloroplast complexes. Longatte [79] tested seven different quinones including 2,6-dichlorobenoquinone (2,6-DCBQ), p-phenylbenoquinone (PPBQ) to estimate the efficiency of the exogenous quinones from algae in the PBS. 2,6-DCBQ was recommended for electrochemical applications as electron carriers in photosynthetic activities.

2.5 Application of Scanning Electrochemical Microscopy (SECM) in Microbiology

Scanning electrochemical microscopy (SECM) is a powerful analytical method for biochemical kinetic studies, which provides a real-time, label free and noninvasive investigation in biological systems [80–82]. SECM utilizes an ultramicroelectrode (UME) for substrate characterization by measuring electrochemical current of an aqueous redox molecule as it interacts with a substrate. For example, the reaction at the UME can be the diffusion-limited reduction reaction of an oxidized redox species O to R ($O + ne \rightarrow R$), where the steady state limiting current on the UME ($i_{T,\infty}$) is given by equation (2-1) **(Figure 2-1a)**.

$$i_{T,\infty} = 4nFDC_Oa \quad (2\text{-}1)$$

In this equation, F is the Faraday constant, D is the diffusion coefficient, C_O is the bulk concentration of species O, and a is the disk radius.

The feedback modes of SECM are based on negative and positive feedback effects, which are driven by either insulating or conductive substrates, respectively, as shown in **Figure 2-1**. When the UME approaches an insulating substrate, the current on the UME decreases proportionally as the distance between the UME and substrate decrease (**Figure 2-1b**). On the other hand, when the UME approaches a conductive substrate, the active redox mediator cycling between the UME and the substrate significantly increases as the distance decreases between UME and substrate. Therefore, the current on the UME increases when the UME approaches the

conductive substrate. It is important to note that the mediator regeneration reaction on the conductive substrate can be kinetically limited, hence, the reaction rate constant can be determined by this method. The feedback modes of SECM have been applied for measuring cell redox activity [83].

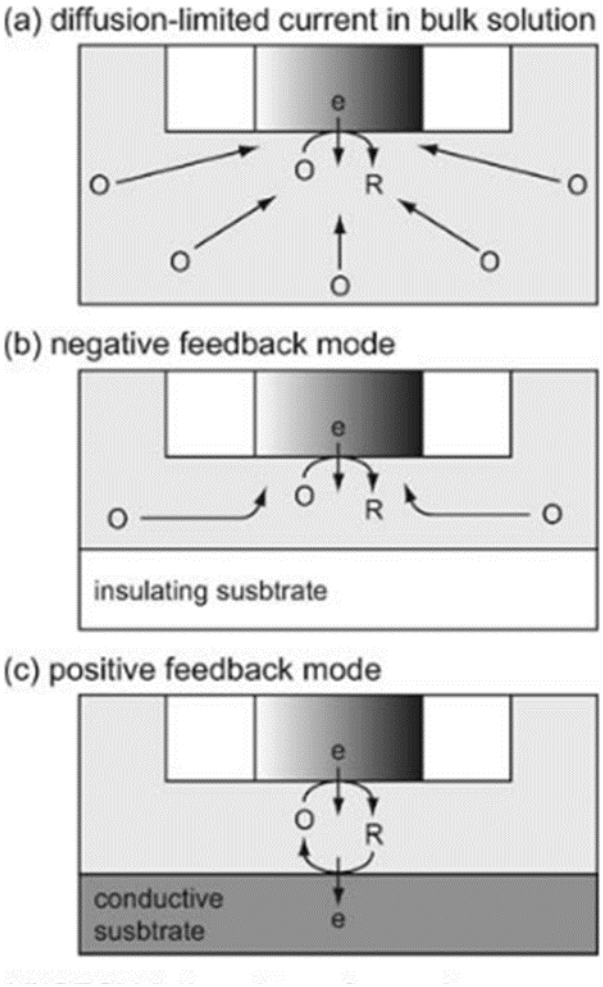

Figure 2- 1. Principles of SECM, showing (a) hemispherical diffusion to the disk-shaped tip positioned far from the substrate, (b) the negative feedback mode based on hindered diffusion by insulating substrate, (c) the positive feedback mode at conductive substrate Modified from reference [83].

SECM has also been utilized for rapid chemical species mapping. As expected, the image obtained with SECM is dependent on the selectivity of the probe. This selectivity includes pH measurements using antimony electrodes [43, 44]. The measurement of fast pH changes and chemical activities in microenvironments has been performed using SECM with different UMEs [85]. In particular, various metal and metal oxide SECM tips have been used for local pH measurement [86]. Specific types of electrodes include Sb_2O_3, IrO_2, TiO_2, MnO_2, Bi_2O_3, PtO_2, SnO_2, OsO_2, Ta_2O_5, PdO, RuO_2, RhO_2, ZrO_2, Hg_2O, HgO, Co_3O_4, and PbO_2 [74, 75, 85–87]. Iridium oxide (IrO_x) pH electrodes have the following advantages relative to other metal/metal oxides probes: (1) wide linear pH response range (pH 2-10) and (2) fast and stable response in aqueous systems [75, 87].

Moreover, SECM can also be applied for cell morphology [82, 83], physiology phenomenon [83] and species transfer [77] studies in biological systems [88]. Shiku et.al [89] investigated O_2 consumption of single bovine embryos by SECM monitoring. They concluded the embryo size was strongly correlated to the oxygen consumption. Host animals utilize O_2 with a squid- activated-membrane oxidase complex to produce H_2O_2 to protect themselves against the pathogenic microorganisms. Hence, to counteract this oxidative stress, the catalase on bacteria rapidly reduces the concentration of H_2O_2 through decomposition to water and O_2 near the bacteria cell surface. Abucayon et al. [90] studied the H_2O_2 decomposition for catalase activity on the biofilms by operating SECM with the Pt UME. Yasukawa et al. [78] explored the application of the SECM for studying algae's photosynthetic activity. During photosynthesis, the respiratory electron transfer in the protoplast was monitored using amperometric measurements. In addition, SECM can also be used to monitor cell respiration and cellular redox activity. Moreover, DNA can also be captured by SECM imaging. Turcu et al. [91] developed an DNA probe by electrostatic

approach to visual the status. Ferricyanide ($[Fe(CN)_6]^{3-}$) was used as a mediator for DNA detection. Results indicated that when the tip was scanned across a gold electrode functionalized with DNA, the tip current decreased due to the repulsive forces between the mediator and DNA.

3. Role of Near-Electrode Solution Chemistry on Bacteria Attachment and Poration at Low Applied Potentials

REPRINTED WITH PERMISSION FROM M.-H. LIN, S. MEHRAEEN, G. CHENG, C. RUSINEK and B.P. CHAPLIN, ROLE OF NEAR-ELECTRODE SOLUTION CHEMISTRY ON BACTERIA ATTACHMENT AND PORATION AT LOW APPLIED POTENTIALS ENVIRON. SCI. TECHNOL. 2020, 54, 446−455 COPYRIGHT 2019 AMERICAN CHEMICAL SOCIETY

3.1 Abstract

This research investigated mechanisms for biofouling control at boron-doped diamond (BDD) electrode surfaces polarized at low applied potentials (e.g., -0.2 to 1 V versus Ag/AgCl), using *Pseudomonas aeruginosa* as a model organism. Results indicated that electrostatic interactions between bacteria and ionic electrode functional groups facilitated bacteria attachment at the open circuit potential (OCP). However, under polarization the applied potential governed these electrostatic interactions and electrochemical reactions resulted in surface bubble formation and near-surface pH modulation that decreased surface attachment under anodic conditions. The poration of the attached bacteria occurred at OCP conditions and increased with the applied potential. Scanning electrochemical microscopy (SECM) provided near-surface pH and oxidant formation measurements under anodic and cathodic polarizations. The near-surface pH was 3.1 at 1.0 V vs. Ag/AgCl and 8.0 at -0.2 V vs. Ag/AgCl and was likely a contributor to bacteria poration. Interpretation of SECM data using a reactive transport model allowed for a better understanding of the near-electrode chemistry. Under cathodic conditions, the primary oxidant formed was H_2O_2 and under anodic conditions a combination of H_2O_2, $Cl^{\bullet}$, and Cl_2 formation likely contributed to bacteria poration at potentials as low as 0.5 V vs. Ag/AgCl.

3.2 Introduction

Biofilm growth is of critical concern in many industries including drinking water systems [30, 46]. Biofouling can greatly affect the performance of water treatment membranes [20, 26], capacitive deionization electrodes [27], and other treatment technologies. Biofilm growth in water distribution systems is also a significant health concern [92]. Currently, the prevailing biofilm control strategies used in water treatment include chemical sterilization (e.g., chlorine),[28], [29] surface modification[20, 30], and nanoparticle deposition (e.g., Ag) [7, 31]. Although effective, each method has unique challenges. Chemical sterilization requires shipment and storage of hazardous chemicals, and both surface modification and nanoparticle deposition techniques have a finite service life [51, 93], due to slow fouling of the modified surface and nanoparticle depletion, respectively.

Electrochemical techniques are effective biofouling control strategies [3, 11, 12, 32] and offer technical advantages over traditional methods. Disinfectants, including reactive oxygen species (ROS) and Cl-based oxidants, can be generated *in situ* by reactions at the electrode surfaces, thus mitigating the concerns over shipping and storage of hazardous chemicals. In addition, system performance of electrochemical technologies is easily automated and controlled remotely.

Although electrochemical methods have been studied to prevent bacteria attachment or promote poration,[32–34, 94] the mechanisms for bacteria poration at low applied potentials is not thoroughly understood. Several electrochemical-mediated poration mechanisms have been proposed in the literature, including: 1) electroporation [3, 12], 2) disruption of the intracellular redox potential by the applied electric field [33], 3) direct electron transfer reactions [95], 4) acidic/basic pH at the electrode surface [53], and 5) *in situ* ROS ($OH^{\bullet}$, $O_2^{\bullet-}$, H_2O_2, O_3) and Cl_2 generation [14, 96].

The objectives of this study were to investigate bacteria poration at electrified interfaces at low applied potentials and provide insights into the attachment and poration mechanisms. A model biofilm forming bacteria (i.e., *Pseudomonas aeruginosa* (PAO1)) was studied at boron-doped diamond (BDD)

electrode surfaces at potentials between -0.2 V and 1 V (vs Ag/AgCl). Scanning electrochemical microscopy (SECM) was utilized to monitor the near-surface pH and formation of ROS resulting from electrochemical reactions. The SECM results were interpreted using a reaction-diffusion model and finite element method. Insights gained from the experiments and modeling were used to propose possible poration mechanisms for bacteria at low applied potentials.

3.3 Experimental

3.3.1 Reagents

Sodium perchlorate ($NaClO_4$), phosphate buffer silane (PBS), sodium chloride (NaCl), oxalic acid dehydrate, 30% hydrogen peroxide (H_2O_2), potassium hexacyanoferrate (III) ($K_3[Fe(CN)_6]$), potassium hexacyanoferrate (II) ($K_4[Fe(CN)_6]$), hexaammineruthenium (II) chloride ($Ru(NH_3)_6Cl_2$), hexaammineruthenium (III) chloride ($Ru(NH_3)_6Cl_3$) and Nafion® were purchased from Sigma-Aldrich (St. Louis, MO USA). The (3-Aminopropyl)triethoxysilane, 98% (APTES), iridium tetrachloride ($IrCl_4$), and 1-ethyl-3-(3-dimethylaminopropyl)carbodiimide (EDC) were purchased from Alfa Aesar (MA, USA). Tryptone was purchased from IBI Scientific (Iowa, USA). Granulated yeast extract and Drisolv® toluene anhydrous were purchased from EMD Millipore (USA). MasterMet^{TM} non-crystallizing colloidal silica (0.02 µm) polishing suspension was purchased from Buehler (IL, USA). The viability/cytotoxicity assay kit was purchased from Biotium (Fremont, CA USA). Solutions were made from Elga purelab flex ultrapure deionized (DI) water (18.2 MΩ cm at 21 °C). The PAO1 bacteria was isolated from a patient from University of Washington [97]. All chemicals were used as received.*Electrode Preparation and Characterization*

Optically transparent electrodes (OTEs) and microelectrode arrays (MEAs) were fabricated at Fraunhofer USA Center for Coatings and Diamond Technologies (East Lansing, MI). The OTEs consisted of a BDD microcrystalline film deposited on a 2 mm thick quartz glass substrate using hot filament chemical

vapor deposition (CVD). The OTEs were cut into 1 cm^2 diameter disks using a laser cutting system. The MEAs were described in detail previously [98] and consisted of 20 μm diameter BDD microelectrodes spaced 300 μm apart (see **Appendix A**, **Figure A-1**). A single microelectrode made up ~ 0.35 % of the total BDD surface area. An anodic pretreatment process in 1 M $NaClO_4$ (20 mA cm^{-2} for 20 min) was used to clean the BDD/OTE electrode and terminate it with -OH groups [99]. An APTES-functionalized BDD/OTE (APTES-BDD/OTE) electrode was prepared from a pretreated BDD/OTE after rinsing with methanol, ethanol, and water. The cleaned BDD/OTE was immersed in 5 mM APTES in anhydrous toluene and allowed to react in an Ar-filled glove box for 3 hours. The APTES-BDD/OTE was then rinsed three times with toluene and methanol and annealed at 120 °C for 30 min to promote cross-linking of the silanes [100, 101].

The surface functional groups on the OTEs were characterized by XPS (Kratos Axis-165). Cycle voltammetry (CV) scans (100 mV s^{-1}) were performed with ionic redox couples (5 mM $Fe(CN)_6^{3-/4-}$ and 5 mM $Ru(NH_3)_6^{3+/2+}$) in the PBS electrolyte to evaluate charge transfer. Contact angle measurements were made using the sessile drop method and Image J software with DropSnake plugin [102].

3.3.2 Bacteria Growth Media and Culture Conditions

The PAO1 cells were transferred from a stock solution and cultured in lysogeny broth (LB), which contained 10 g tryptone, 5 g yeast extract, and 10 g NaCl in 1 L of DI water. The culture was incubated at 37°C on a rotary shaker at 160 rotations per minute (rpm) for 16 hours to late-log phase [103]. After incubation, bacteria cells were washed three times in PBS by centrifugation at 7000×g for 5 min at room temperature. The concentration of the bacteria was quantified by optical density (OD) measurements at 600 nm (OD_{600}). Direct plate counts were performed and a standard

curve of OD versus plate count numbers was constructed (**Figure A-2**). The bacterial cell concentration was ~10^9 cells mL^{-1} at an OD_{600} = 1.0.

3.3.3 Dual Staining Procedure

The viability/cytotoxicity assay kit for bacteria live and dead cell counts (Biotium, USA), was used according to the manufacturer's protocol [104, 105]. DMAO is a green nucleic acid dye that stains both live and dead bacteria (excitation 503 nm/emission 530 nm), while EthD-III is a red dye (excitation 530 nm/emission 620 nm) that only stains cells with a damaged outer membrane. More details are provided in the **Appendix A**.

3.3.4 Bacteria Attachment/ Poration Studies

The PAO1 was washed and resuspended in a centrifuge tube with PBS to ~ 10^9 cells mL^{-1} and transferred to a 2 mL Teflon® cell for attachment and poration studies (**Figure 3-1**). The OTEs were the working electrodes and were sealed at the bottom of the cell with an o-ring and a titanium foil was used as a current collector. A Pt wire was used as counter electrode and a Ag/AgCl electrode was used as a reference (**Figure 3-1a**). Potentials and currents were controlled and monitored with a bipotentiostat (CHI920D model, CH Instrument, Inc). Each experiment was conducted for 105 minutes at a constant potential from -0.2 V to 1.0 V vs. Ag/AgCl. Bacteria attachment numbers and live/dead ratio were determined after each experiment. Details are provided in the **Appendix A**.

3.3.5 Ultramicroelectrode pH Probe Fabrication and Measurements

To monitor the pH near the OTE surface, a pH probe was fabricated by anodic electrodeposition of an iridium oxide film on a commercial Pt ultramicroelectrode (UME) [106], [107]. Details of the fabrication method are provided in the **Appendix A**. The pH measurements

were made 2 µm above the OTEs using SECM. The IrO_2 UME was calibrated with pH buffer solutions (pH 2-10) under ambient conditions, and Nernstian slopes in the range of 50-65 mV pH^{-1} were obtained and considered acceptable for pH measurements [106]. The pH was monitored over time and as a function of the applied potential on the OTE surface (-0.2 to 1.0 V vs Ag/AgCl). The setup for pH monitoring experiments is shown in **Figure 3-1b** and 3-**1c**. A standard three-electrode setup was used to control the potential on the OTEs, as described for the attachment/poration studies. The pH was measured by monitoring the potential between the IrO_2 UME and a second Ag/AgCl reference electrode using a digital multimeter (Neotech^{TM}, Hong Kong).

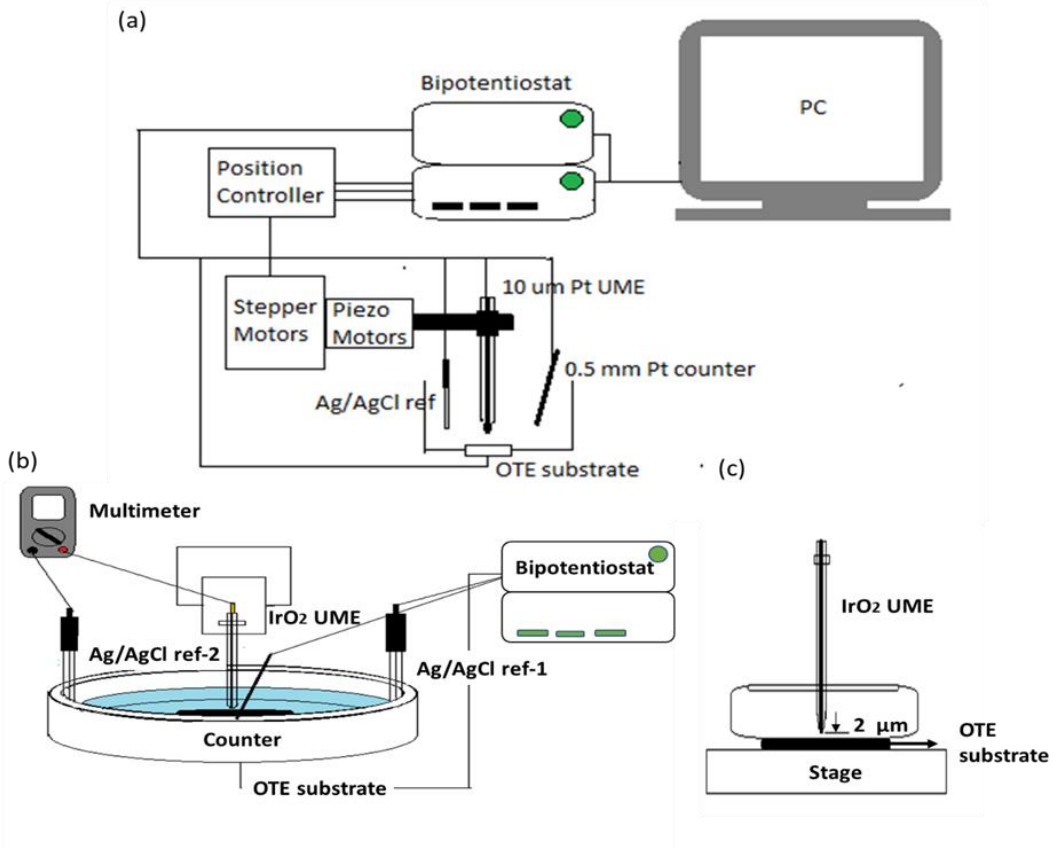

Figure 3- 1. Scanning electrochemical microscopy (SECM) setup (a) with 10 µm Pt UME, counter, reference electrode and OTE substrate, (b) for pH monitoring with multimeter and additional reference electrode.

3.3.6 ROS Formation Measurements

The Pt UME was used to detect ROS formation from a single microelectrode of the BDD MEA. These measurements were conducted over a potential range of -0.5 to 1.0 V vs Ag/AgCl. The Pt UME was located 2 µm above the MEA insulating surface and was held constant at 0.9 V vs Ag/AgCl. A standard three-electrode setup was used to control the potential on the MEA.

3.3.7 Reaction-Diffusion Model

To interpret the SECM data, a reaction-diffusion model was developed. The model simulated the reaction of two species (H_2O_2 and $Cl^{\bullet}$) and their diffusion between the BDD and UME tip surface at steady-state in two dimensions with radial symmetry. Finite element method was used to numerically solve the coupled reaction-diffusion equations with appropriate boundary conditions in Matlab. More details about the model, boundary conditions, and solution method are provided in the **Appendix A** (**Figure A-3)**.

3.4 Results and Discussion

3.4.1 Electrode Characterization

Surface hydrophobicity and electrostatic interactions are two critical factors that affect cell adhesion to solid surfaces [4, 5, 46]. To understand the surface-bacteria interaction, two different electroactive surfaces were used, BDD/OTE and APTES-BDD/OTE. The CV scans were used to determine the effect of surface charge on charge transfer reactions with ionic redox couples (**Figure 3-2)**. The CV scans illustrated that the BDD/OTE and APTES-BDD/OTE have a similar potential window for solvent stability from 0.6 to -0.6 V vs. Ag/AgCl in the PBS electrolyte. The similar charging current for the two electrodes indicated that the surface area did not change significantly due to the APTES surface modification (**Figure 3-2a**). The positive surface charge

of the APTES-BDD/OTE resulted in a significantly higher peak current for the 5.0 mM $Fe(CN)_6^{3-/4-}$ inner sphere redox couple relative to the BDD/OTE (**Figure 3-2b**), which was attributed to electrostatic interactions between the anionic redox couple and the positively charged amino groups ($-NH_3^+$) on the APTES-BDD/OTE surface. By contrast, the peak current was only slightly reduced on the APTES-BDD/OTE relative to the BDD/OTE with the 5 mM $Ru(NH_3)_6^{2+/3+}$ outer sphere redox couple (**Figure 3-2c**). These results indicated that charge transfer reactions involving the outer sphere redox couple were not as sensitive to the surface charge of the OTE as the inner sphere redox couple. The peak separation of both redox couples was similar for both electrodes, indicating that the charge transfer kinetics were not significantly affected by the APTES functionalization process. The BDD/OTE had a hydrophilic surface [107], with a measured contact angle of 45 degrees (**Figure 3-2d**). The APTES-BDD/OTE electrode had a hydrophobic surface, with a measured contact angle of 97 degrees (**Figure 3-2d**) and a positively charged surface at neutral pH (pKa = 7.6).

Analysis of the OTEs by XPS was used to determine the surface chemistry (**Figure 3-2e** and **Table 3-1**). Analysis of the XPS data determined six separate C 1s peaks (**Table 3-1**). Assignments for the C 1s spectrum were based on literature values [99]. Past studies have shown that the various oxygenated functional groups form on the BDD surface as a result of anodic polarization [64]. The BDD/OTE contained primarily C-H (C1 = 42%), C-C (C2 = 21%) and C-OH (C4 = 19%) groups. A significant proportion of the C-NH (C3 = 18%) and $–(CH_2CH_2NH)_n$- (C6 = 16%) groups were detected on the APTES-BDD/OTE as a result of the functionalization (**Figure 3-2f** and **Table 3-1a**). The peak area ratios for C/O, C/N, and C/Si are shown in **Table 3-1b.** The C/O ratio was similar for both OTEs, but the C/N and C/Si ratios decreased due to APTES

functionalization. Comparing the C/N and C/Si ratios before and after functionalization provided an estimate of 70% APTES surface coverage (see **Appendix A**).

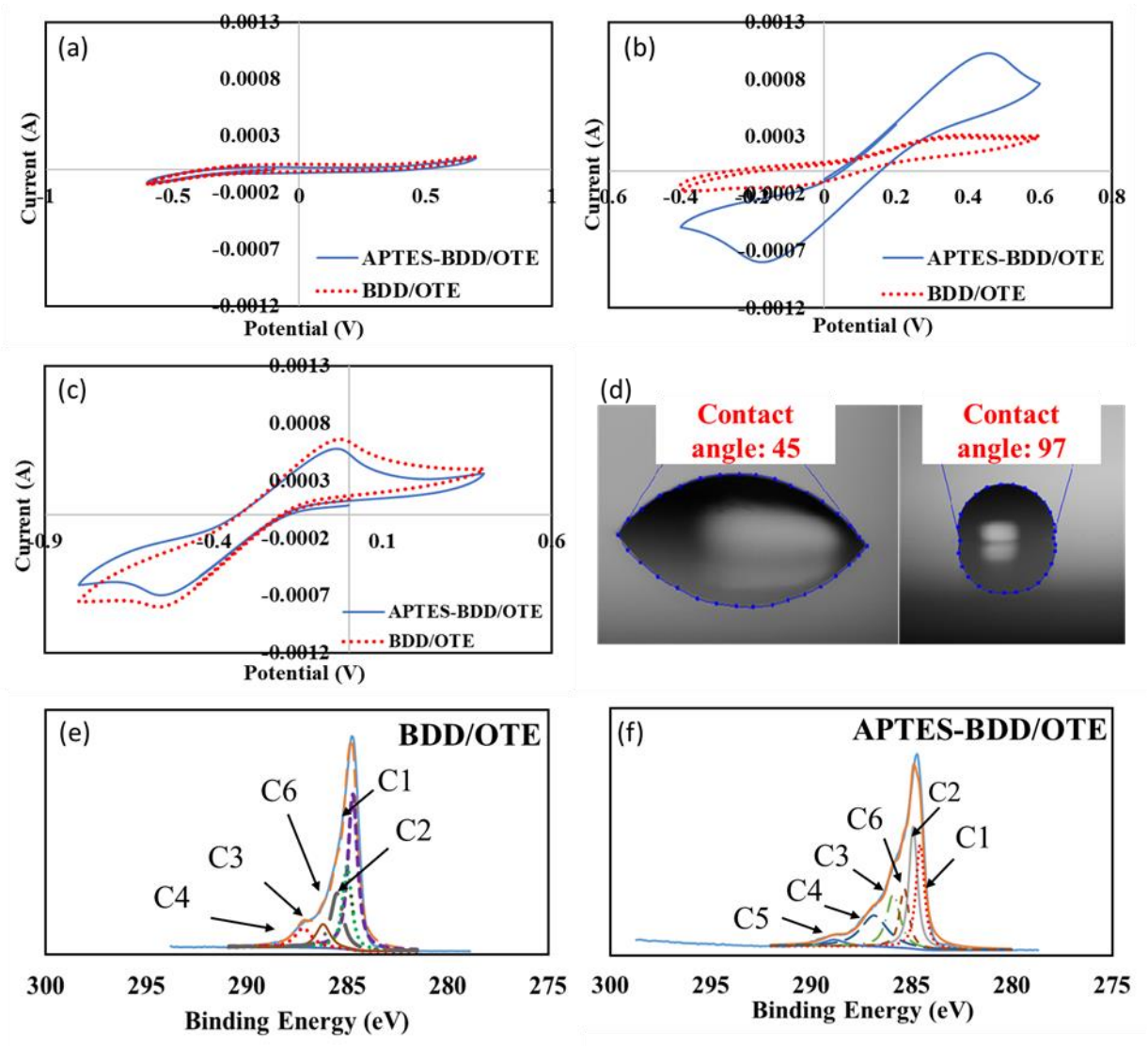

Figure 3- 2. Cyclic volatammogram (CV) curves of bare BDD/OTE and APTES-BDD/OTE in the (a) phosphate buffer solution (PBS) (b) PBS containing 5 mM $K_3Fe(CN)_6$ / $K_4Fe(CN)_6$ and (c) PBS containing 5mM $Ru(NH_3)_6Cl_3$/$Ru(NH_3)_6Cl_2$. (V v.s Ag/AgCl) (d) Contact angles of BDD/OTE and APTES-BDD/OTE. XPS spectra analysis of (e) BDD/OTE and (f) APTES-BDD/OTE. XPS peak identification provided in Table 3-1.

Table 3- 1. (a) Summary of XPS peaks and (b) elements ratio on both OTEs

Peak Label	Binding energy (eV)	Possible functional groups	Surface Coverage BDD/OTE (%)	Surface Coverage APTES-BDD/OTE (%)	Reference
C1	284.6 ± 0.15	C-H	41.9	17.7	[99]
C2	285.1 ± 0.3	C-C	20.8	25.8	[99]
C3	286 ± 0.3	C-O/C=O/ $-(CH_2CH_2NH)_n-$	9.1	17.6	[108]
C4	286.4 ± 0.3	C-OH	18.8	19	[99]
C5	288.7±0.15	-COOH	0	4	[99]
C6	285.5	C-NH	9.3	15.6	[109]

(b) Elements ratio on both OTEs.	BDD/OTE	APTES-BDD/OTE
C/O	5.9	3.4
C/N	59.5	18.5
C/Si	64.5	20.5

3.4.2 Bacteria Attachment/ Poration Studies

Initially, bacteria cells suspended in the bulk solution experience hydrodynamics and physicochemical forces (i.e., van der Waals, electrostatic interactions) as they approach the surface of a substrate. These intermolecular forces are primarily between the $-COO^-$, $-NH_3^+$and $-PO_4^{2-}$ functional groups of the bacteria surface and the functional groups of the substrate [110]. Results for the bacteria attachment studies are shown in **Figure 3-3a** and indicate a relationship between the number of attached cells and the applied potential on the OTEs. In general, bacteria attachment was significantly enhanced on the hydrophobic, positively charged APTES-BDD/OTE compared to the hydrophilic BDD/OTE at the open circuit potential (OCP) and under applied anodic potentials. The total bacteria attachment numbers were similar on both OTEs under cathodic

potentials with the exception of the most cathodic potential (-0.2 V vs Ag/AgCl), where attachment was observed for the APTES-BDD/OTE but not for the BDD/OTE (**Figure 3-3a**). These results were attributed to electrostatic interactions between the APTES-modified surface and bacteria. The zeta potential measurements for PAO1 as a function of pH indicated that they were negatively charged over the pH range of 5 to 12 (**Appendix A**, **Figure A-4**). Therefore, under anodic potentials the positively charged electrode attracted the bacteria and they were electrostatically adsorbed at the positively charged $-NH_3^+$ functional groups of APTES. Higher anodic potentials showed a decrease in the attachment numbers, which was attributed to the generation of small bubbles from water oxidation, which likely blocked the electrode surface [111]. At the same time, the surface pH on the electrode was < 5.0 when the applied potentials were higher than 0.5 V vs Ag/AgCl, due to water oxidation (see **Figure 3-4** and associated discussion). The bacteria surface becomes positively charged in this pH range (**Appendix A, Figure A-4**). Therefore, the decrease in the attachment numbers at higher anodic potentials may also be due to electrostatic repulsive forces between the positive surface charges of bacteria and the anode. These phenomena are most evident at the highest anodic potential (1.0 V vs Ag/AgCl). The cell attachment on both OTEs decreased upon the application of cathodic potentials due to the repulsive forces between the OTEs and bacteria cells, indicating that the polarization charge of the electrode was more significant than the ionic charge of the $-NH_3^+$ functional groups of APTES and the functional groups were also deprotonated at the alkaline surface pH.

After each experiment the attached cells were analyzed for their membrane integrity using fluorescent microscopy. **Figure 3-3b** shows the percentage of dead cells as a function of the applied potential on the OTEs, which was determined by averaging the mean direct count values from triplicate experiments. The error bars represent the standard deviation about mean values.

The mean value from an individual experiment was obtained by averaging the direct count of 10 random locations (128 by 128 μm area) on each sample. In general, damage to the bacterial membrane was observed at applied potentials that were > 0.8 or < -0.1 V vs. Ag/AgCl (**Figure 4b**). Representative fluorescent images showing the live/dead cells at each potential on the OTEs are provided in the **Appendix A** (**Figure A-5**). It should be noted that planktonic control experiments under similar solution conditions showed low cell deaths (< 3%), indicating that electrode mediated processes were responsible for bacteria membrane damage even at the OCP.

(a)

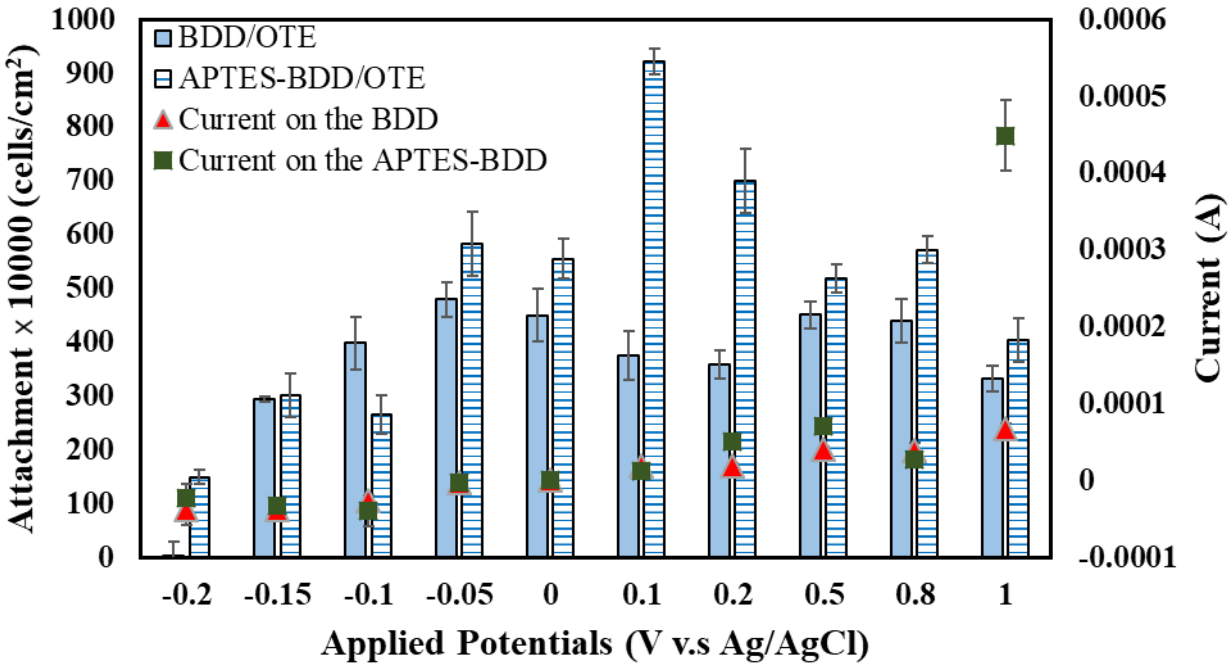

(b)

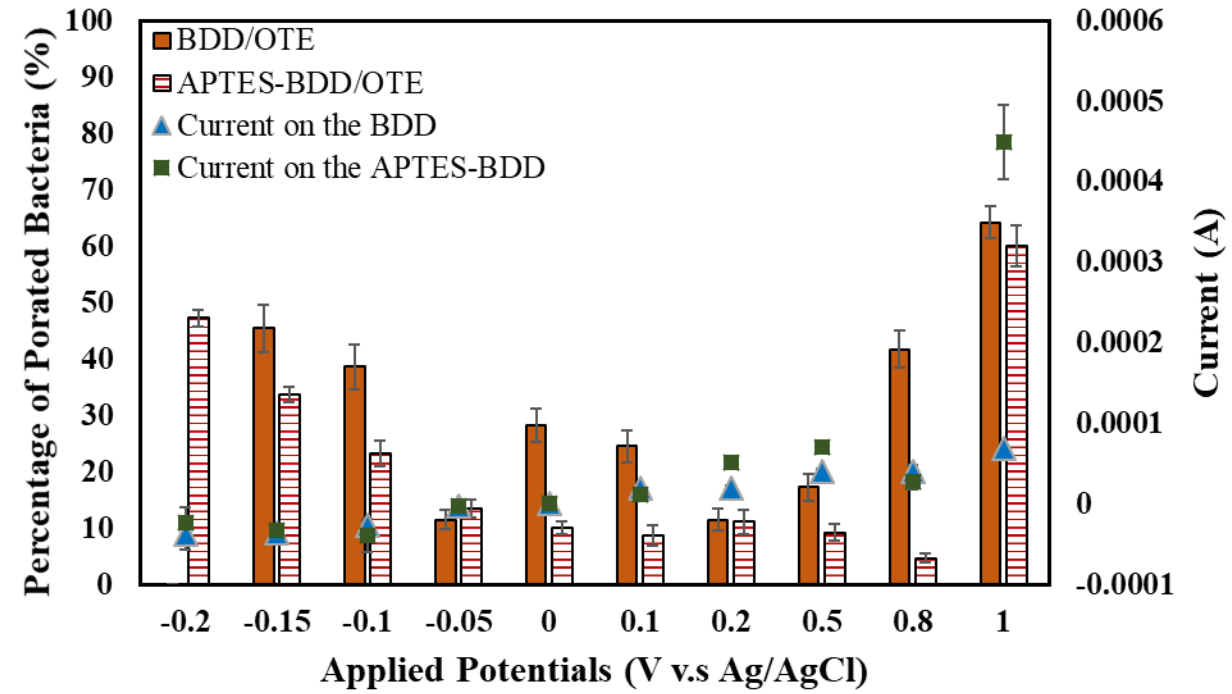

Figure 3- 3. (a) Comparison of the Pseudomonas aeruginosa (PAO1) attachment on the different substrates with applying different potentials (bars). Bacteria were not detected on the BDD surface when applied -0.2 V. (b) Comparison of the dead bacteria ratio (bars) on the two different substrates as a function of the applied potential. The data points represent the measured current.

3.4.3 SECM Characterization

There are several proposed mechanisms for bacteria poration at polarized electrode surfaces at low potentials (< |±1.0| V/SHE). These mechanisms include: 1) electroporation [32], 2) disruption of the intracellular redox potential by the applied electric field [50], 3) direct electron transfer reactions [95], 4) acidic/basic pH at the electrode surface [53], and 5) ROS ($OH^{\bullet}$, $O_2^{\bullet-}$, H_2O_2, O_3) and Cl_2 generation at the electrode surface [96]. Electroporation was not considered a significant contributor to cell poration because the electric field strength was rather small (e.g., 500 V m^{-1}, **Appendix A, Table A-1**). Generally electric fields of > 20,000 V m^{-1} are needed to cause electroporation [112]. The electric field effect on the intracellular redox state was not investigated, but the mechanism responsible for this effect was not clearly described in prior work [14], and it is also difficult to imagine how a relatively weak electric field of approximately 500 V m^{-1} would affect intracellular processes. Direct electron transfer reactions were also not considered as a primary contributor to cell poration, as measured currents did not increase upon the progressive addition of cells to solution (data not shown). The remaining probable mechanisms (i.e., pH change and ROS and Cl_2 production) were further explored using SECM experiments.

Under anodic and cathodic polarization conditions the oxygen evolution reaction (reaction 3-1) and the hydrogen evolution reactions (reactions 3-2 and 3-3), respectively, can significantly alter the near-surface pH.

$$2H_2O \rightarrow O_2 + 4H^+ + 4e^- \quad (3\text{-}1)$$

$$2H^+ + 2e^- \rightarrow H_2 \quad (3\text{-}2)$$

$$2H_2O + 2e^- \rightarrow H_2 + 2OH^- \quad (3\text{-}3)$$

In our previous study we estimated the surficial pH (pH_s) using mass transport calculations was pH_S = 4.4 at an anodic surface potential of 0.8 V vs. Ag/AgCl and pH_S = 10.5 at a cathodic surface potential of -0.5 V vs. Ag/AgCl. It was concluded that the acidic/alkaline pH was the primary contributor to bacteria poration [53]. To provide further support for this mechanism, an IrO_2 UME was utilized to monitor the pH ~2 µm above the OTE surface at the various potentials used in the poration experiments (**Figure 3-4**). Results indicated that the final measured pH ranged from 3.1 at an anodic potential of 1.0 V vs Ag/AgCl to approximately 8.0 at a cathodic potential of -0.2 V vs Ag/AgCl, where the bulk pH remained constant at 7.4 by the buffering capacity of the PBS electrolyte. The acidic/basic surface conditions measured by SECM correlate with the poration trends shown in **Figure 3-3b**, which suggests that they may have contributed to bacteria poration. The adaptive acid and alkaline tolerance range for neutrophilic bacteria is between pH values of 5.5 to 8.5 [113, 114]. SECM results clearly demonstrated that conditions near the electrode surface, where bacteria were adsorbed, were significantly different from the neutral pH in the bulk solution.

The pH measurements also indicated that the pH change as a function of potential was more moderate for the APTES-BDD/OTE compared to the BDD/OTE (**Figure 3-4**). For example, the pH decreased sharply when a 1.0 V vs. Ag/AgCl anodic potential was applied to the BDD/OTE after 30 minutes and remained around pH 3.5. By contrast, the surface pH decreased slowly on the APTES-BDD/OTE over the duration of the 90-minute experiment. These results were attributed to the buffer capacity of the $-NH_2/-NH_3^+$ groups of APTES. This surficial buffer capacity may explain the generally lower ratio of dead bacteria observed on the APTES-BDD/OTE relative to the BDD/OTE (**Figure 3-3b**).

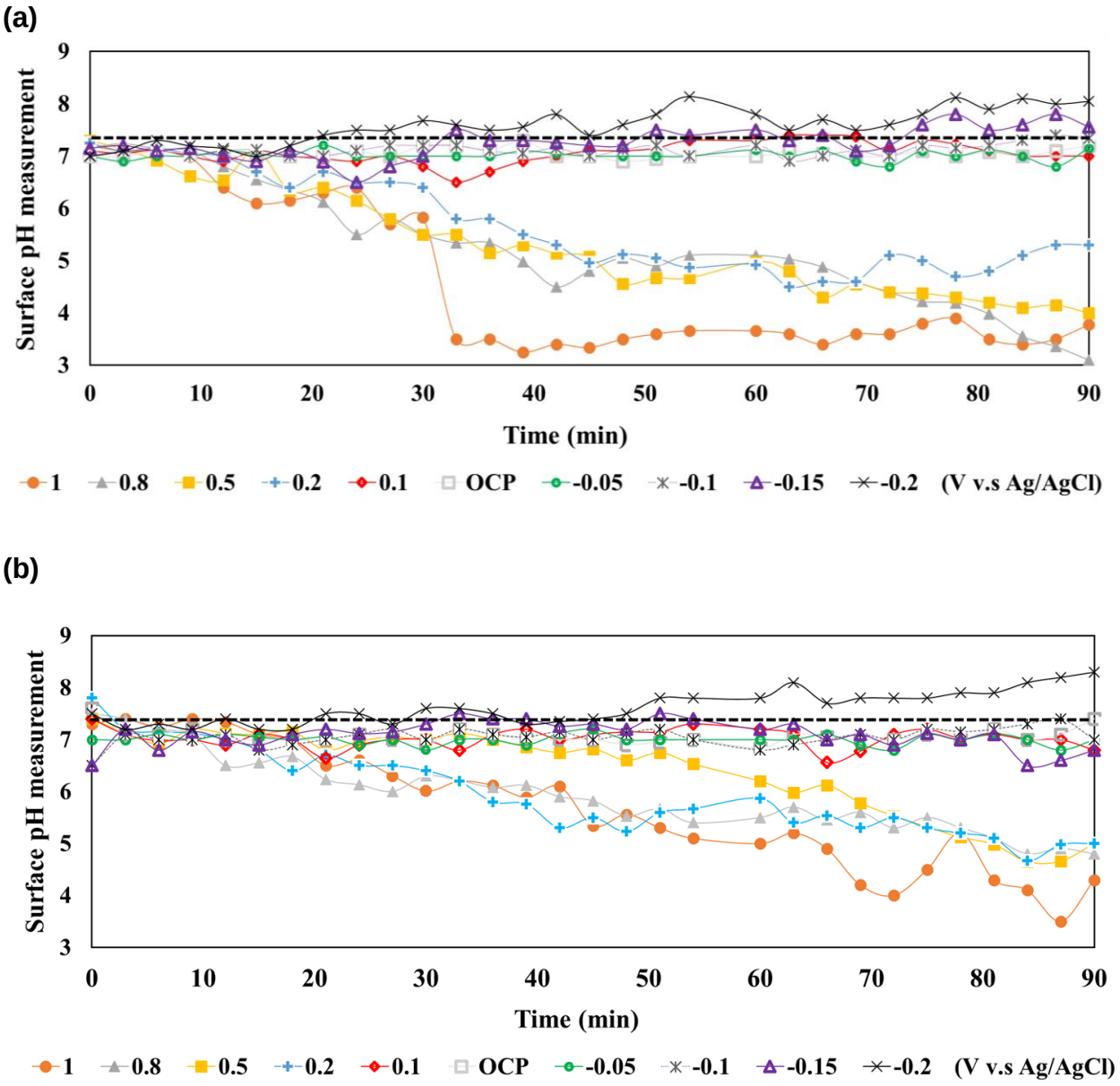

Figure 3- 4. Measurement of pH ~ 2 μm from the electrode surface: (a) BDD/OTE and (b) APTES-BDD/OTE. Dashed line represents the bulk solution pH. The results were averaged from duplicate experiments.

As a complementary experiment, planktonic bacteria experiments were conducted to determine the effect of the bulk pH on bacteria poration. The bacteria size and poration ratio were observed to change as a function of bulk pH and time (**Figure 3-5**). As shown, the bacteria size

increased from 1 μm to 5 μm over the duration of the 90-minute experiment under both acidic and alkaline conditions with a more pronounced increase in cell size at pH > 8.0 (**Figure 3-5a**). The ratio of dead bacteria in these experiments was counted after 90 minutes (**Figure 3-5b**). Results indicated that the bacteria membranes were compromised at pH values greater than 8.4 and less than 5.5, which are in the range of the surficial pH measurements shown in **Figure 3-4**. The increase of the dead bacteria ratio in the different pH solutions may be due to the loss of a binding enzyme on the bacteria's outer membrane inducing membrane instability, bacteria swelling, and ultimately cell death.

(a)

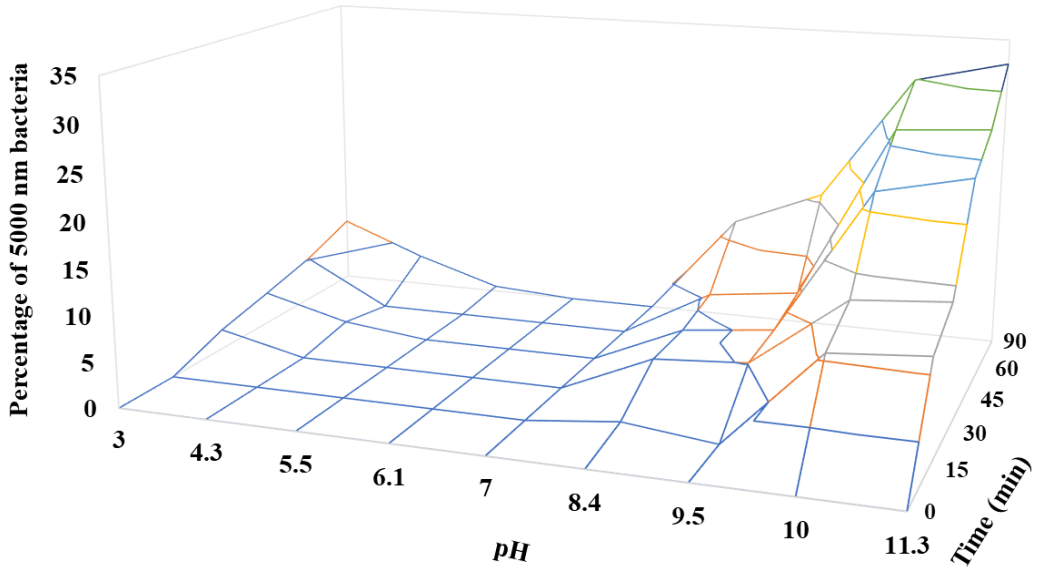

(b)

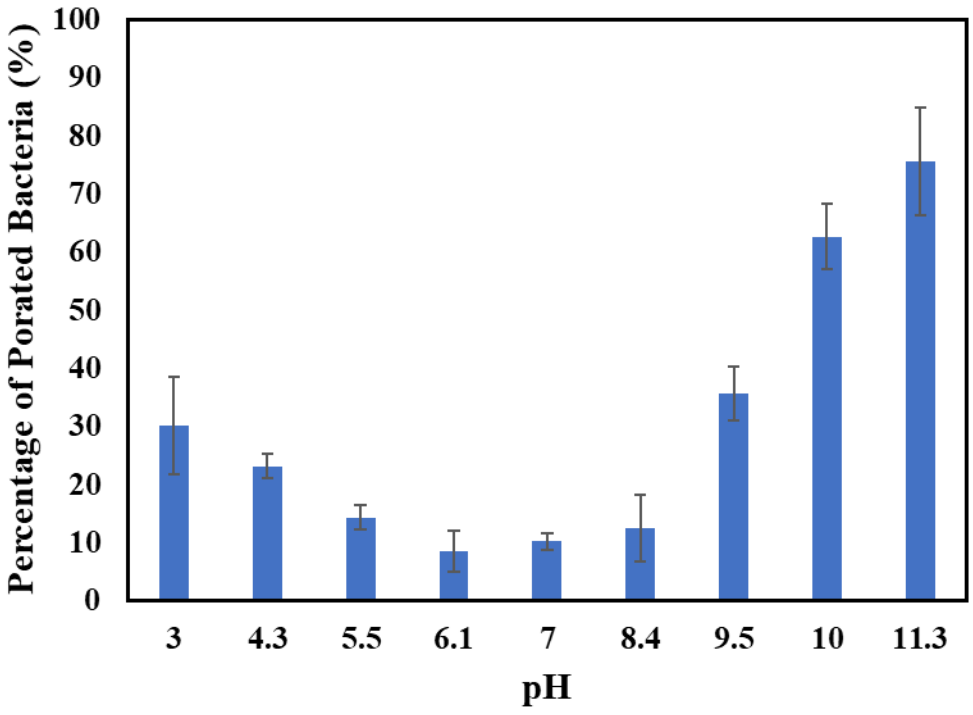

Figure 3- 5. **(**a) The percentage of ~ 5 µm bacteria as a function of solution pH and experimental time. (b) The ratio of dead bacteria at each pH after 90 minutes.

Bacteria poration at low potentials has previously been attributed to ROS and Cl_2 production [10, 33]. Under cathodic polarization conditions the formation of H_2O_2 and $O_2^{\bullet-}$ is possible according to reactions (3-4) and (3-5), respectively.

$$O_2 + e^- \rightarrow O_2^{\bullet-} \quad (3\text{-}4)$$

$$O_2^{\bullet-} + 2H^+ + e^- \rightarrow H_2O_2 \quad (3\text{-}5)$$

In addition, ROS can form under anodic conditions (i.e., $OH^{\bullet}$, H_2O_2, and O_3) according to the following overall redox reactions [96,115–118]:

$$H_2O \rightarrow OH^{\bullet} + H^+ + e^- \qquad E^o = 2.39 \text{ V vs. Ag/AgCl} \quad (3\text{-}6)$$

$$2H_2O \rightarrow H_2O_2 + 2e^- + 2H^+ \qquad E^o = 1.58 \text{ V vs. Ag/AgCl} \quad (3\text{-}7)$$

$$H_2O_2 \rightarrow O_2 + 2H^+ + 2e^- \qquad E^o = 0.49 \text{ V vs. Ag/AgCl} \quad (3\text{-}8)$$

$$O_2 + H_2O \rightarrow O_3 + 2H^+ + 2e^- \qquad E^o = 1.87 \text{ V vs. Ag/AgCl} \quad (3\text{-}9)$$

SECM experiments were conducted to determine the production of ROS under the anodic and cathodic potentials of the poration experiments using a 100 mM $NaClO_4$ electrolyte to prevent the formation of Cl-based oxidants. In order to determine the anodic formation rate of ROS on the BDD MEA, the SECM experiment was conducted in a substrate generation tip collection (SG-TC) mode directly above a single 20 μm diameter microelectrode. A schematic of the positioning of the UME above the MEA is shown in the **Appendix A**, **(Figure A-1d)**. The BDD MEA was held at different anodic potentials. The Pt UME was positioned ~2.0 μm above the MEA insulating layer (i.e., 3.0 microns above the BDD) and was held at a constant potential of 0.9 V vs. Ag/AgCl to oxidize the ROS that was formed at the BDD at a diffusion-limited rate. The ROS formation rate was calculated assuming that H_2O_2 was the major oxidizable compound formed, as O_2, $OH^{\bullet}$,

and O_3 are not oxidized at the potential of the UME. A standard curve was developed for H_2O_2, and the H_2O_2 oxidation current at 0.9 V vs. Ag/AgCl was linear for bulk H_2O_2 concentrations between 10 and 455 μM (R^2 = 0.99; **Appendix A**, **Appendix A-6**). The electrochemical half reactions are shown below, with equilibrium potentials (E_{eq}) calculated based on solution conditions (e.g., pO_2 = 0.21 and pH = 7.5).

BDD (Generation): $2H_2O \rightarrow H_2O_2 + 2e^- + 2H^+$ E_{eq} = 1.17 V vs. Ag/AgCl (3-10)

UME (Collection): $H_2O_2 \rightarrow O_2 + 2e^- + 2H^+$ E_{eq} = 0.06 V vs. Ag/AgCl (3-11)

The results in **Figure 7a** show a significant increase in the background-corrected UME current at substrate potentials ≥ 0.5 V vs. Ag/AgCl, indicating the onset of anodic H_2O_2 formation. A reactive transport model was fit to the total measured current at the UME by changing the value for the H_2O_2 production rate ($v_{H_2O_2}$) at the BDD surface. The values for $v_{H_2O_2}$ are shown in **Table 2** and range from 8.4 x 10^{-6} mol m^{-2} s^{-1} at 0.5 V vs. Ag/AgCl to 1.43 x 10^{-4} mol m^{-2} s^{-1} at 1.0 V vs. Ag/AgCl. Simulations were able to reproduce BDD substrate currents within a factor of 3.7 (**Table 2**). These results suggest that H_2O_2 production was occurring under the anodic potentials used in the poration experiments.

SECM experiments were also conducted in the PBS electrolyte to determine the effect of Cl^- on ROS formation (PBS electrolyte contains 140 mM Cl^-). The UME current during anodic polarization of the BDD was approximately an order of magnitude lower for the PBS solution compared to the $NaOCl_4$ electrolyte (see **Figure 3-6a and 3-6b**). Since the BDD substrate currents were similar for the two electrolyte solutions (see **Table 2**), these results indicated that Cl^- reacted on the BDD surface under anodic conditions to form Cl-based oxidants, which in turn reacted with H_2O_2. In order to interpret the experimental data, the generation of both H_2O_2 and Cl-based

oxidants at the BDD substrate was simulated using the reaction-diffusion model, which also included homogeneous reaction between solution phase oxidants. Model fits to the UME tip current utilized the same values for $v_{H_2O_2}$ as were determined for the $NaClO_4$ electrolyte, as it was assumed that the change in electrolyte did not significantly affect H_2O_2 production (see **Appendix A, Figure A-7**). Simulations indicated that the experimental UME tip currents could be obtained under conditions where the homogeneous kinetics were under diffusion-control (i.e., k > 1 x 10^8 M^{-1} s^{-1}). Based on a review of published second-order reaction rate constants between H_2O_2 and Cl-based oxidants [119], it was determined that $Cl^{\bullet}$ was the probable primary Cl-based oxidant present in the experiments ($k_{Cl^{\bullet},H_2O_2}$ = 2.0 x 10^9 M^{-1} s^{-1}). The formation of Cl_2 according to reaction 13 was also included in the transport model [120, 121].

$$2\ Cl^{\bullet} \rightarrow Cl_2 \qquad k_{Cl^{\bullet},Cl^{\bullet}} = 8.8 \times 10^7\ M^{-1}\ s^{-1} \qquad (3\text{-}12)$$

Any Cl_2 that formed would have negligible effects on the H_2O_2 concentration, due to slow reaction kinetics [122].

$$Cl_2 + H_2O_2 \rightarrow O_2 + 2HCl \qquad k_{Cl_2,H_2O_2} = 1.3 \times 10^4\ M^{-1}\ s^{-1} \qquad (3\text{-}13)$$

In addition, the formation of HOCl/OCl^- and their subsequent reactions with H_2O_2 were also assumed to be negligible based on the relatively slow reaction rate constants, as shown in the reactions below [123, 124] .

$$Cl_2 + H_2O \rightarrow HOCl + Cl^- + H^+ \qquad k_{Cl_2,H_2O} = 15\ M^{-1}\ s^{-1} \qquad (3\text{-}14)$$

$$HOCl + H_2O_2 \rightarrow HCl + H_2O + O_2 \qquad k_{HOCl,H_2O_2} = 1.1 \times 10^4\ M^{-1}\ s^{-1} \qquad (3\text{-}15)$$

$$OCl^- + H_2O_2 \rightarrow Cl^- + H_2O + O_2 \qquad k_{OCl^-,H_2O_2} = 1.7 \times 10^5\ M^{-1}\ s^{-1} \qquad (3\text{-}16)$$

The low UME current also suggested that Cl-based oxidants did not react on the UME under anodic polarization (i.e., 0.9 V vs. Ag/AgCl). The simulated $Cl^{\bullet}$ production rates ranged from 3.36 x 10^{-5} mol m^{-2} s^{-1} at 0.5 V vs. Ag/AgCl to 2.92 x 10^{-4} mol m^{-2} s^{-1} at 1.0 V vs. Ag/AgCl (**Table 3-2**). Simulations were able to reproduce BDD substrate currents within a factor of ~2.2.

Additional SECM experiments were conducted under cathodic polarized conditions to determine the rate constant for the 2e$^-$ oxygen reduction reaction (ORR) to H_2O_2 on BDD ($k_{H_2O_2}$). The BDD substrate was polarized cathodically to facilitate the ORR and the experiments were conducted in the SG-TC mode (**Figure 3-6c**). The half reactions for this experiment are as follows:

BDD (Generation): $O_2 + 2e^- + 2H^+ \rightarrow H_2O_2$ E_{eq} = 0.05 V vs. Ag/AgCl (3-17)

UME (Collection): $H_2O_2 \rightarrow O_2 + 2e^- + 2H^+$ E_{eq} = 0.05 V vs. Ag/AgCl (3-18)

Results indicated that H_2O_2 began to form at -0.5 V vs. Ag/AgCl (**Figure 3-6c**). The reaction-diffusion model was fit to the experimental UME current by varying the value for $k_{H_2O_2}$ at the BDD surface. For the SG-TC mode simulation a value of $k_{H_2O_2}$ = 0.13 s^{-1} was determined. The results for cathodic H_2O_2 formation in the PBS electrolyte were nearly identical to the $NaClO_4$ results ($k_{H_2O_2}$ = 0.17 s^{-1}, **Figure 3-6d**). These results suggested that H_2O_2 was the primary oxidant formed under cathodic conditions.

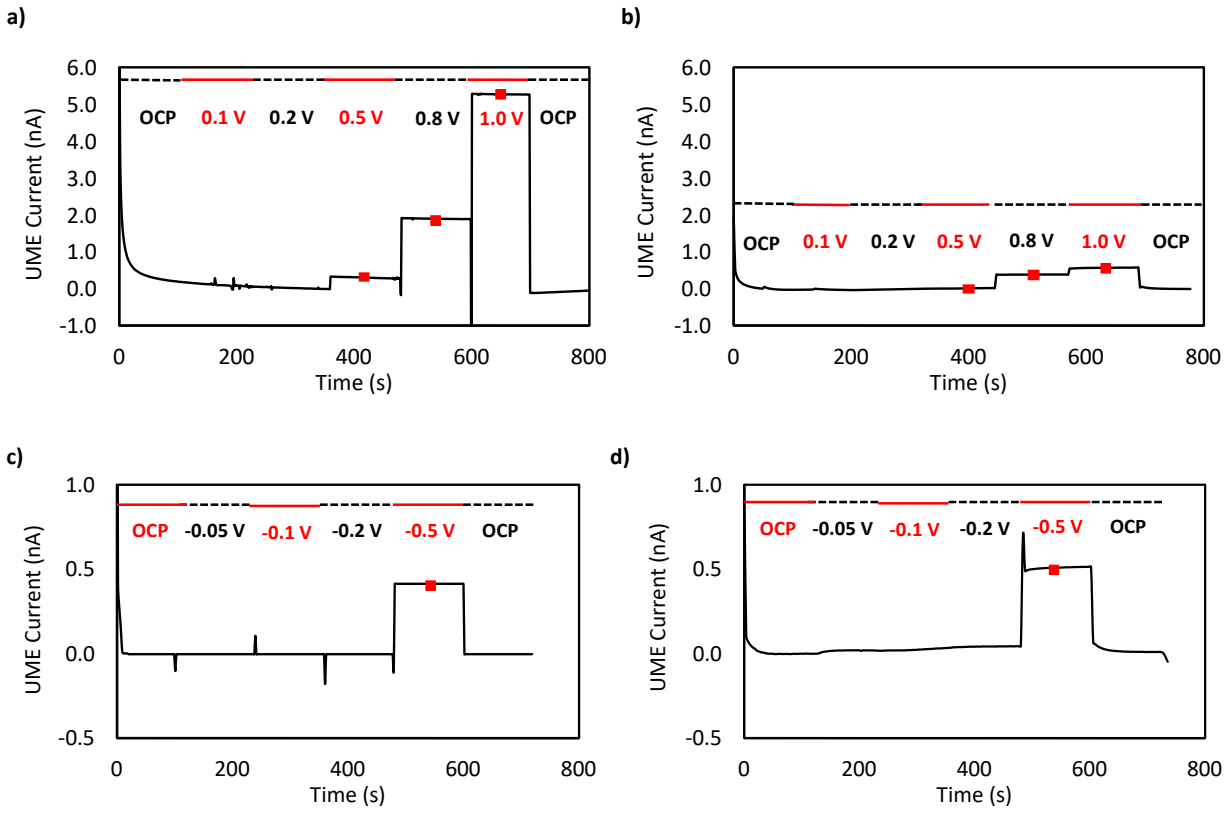

Figure 3- 6. SECM experiments for H_2O_2 detection in substrate generation-tip collection mode. The Pt UME was held constant at 0.9 V vs Ag/AgCl. The solid line represents the background-corrected UME current and the red squares are model fits. The MEA substrate potentials are listed in each figure. (a) substrate polarized anodically in 0.1 M $NaClO_4$, (b) substrate polarized anodically in PBS, (c) substrate polarized cathodically in 0.1 M $NaClO_4$, (d) substrate polarized cathodically in PBS.

Table 3- 2. Summary of experimental SECM and reaction-diffusion simulation results: (a) 0.1 M $NaClO_4$ electrolyte and (b) PBS electrolyte.

a)

Potential V vs. Ag/AgCl	Measured UME Current (nA)	Simulated UME Current (nA)	Measured BDD Current (nA)	Simulated BDD Current (nA)	H_2O_2 production rate (mol m^{-2} s^{-1})
0.5	0.30	0.30	1.9	0.51	8.40E-06
0.8	1.9	1.9	2.7	3.1	5.16E-05
1.0	5.3	5.3	23	8.7	1.43E-04

b)

Potential V vs. Ag/AgCl	Measured UME Current (nA)	Simulated UME Current (nA)	Measured BDD Current (nA)	Simulated BDD Current (nA)	H_2O_2 production rate (mol m^{-2} s^{-1})	$Cl^{\bullet}$ production rate (mol m^{-2} s^{-1})
0.5	0.01	0.01	1.4	3.1	8.40E-06	3.36E-05
0.8	0.39	0.39	3.0	6.4	5.16E-05	1.08E-04
1.0	0.57	0.57	18	18	1.43E-04	2.92E-04

3.5 Conclusion

Results from the SECM experiments suggested that a combination of pH change and oxidant formation at the BDD OTE surface were the primary contributors to bacteria poration. Under cathodic conditions oxidant production had a limited role in bacteria poration, since -0.2 V vs Ag/AgCl was the most cathodic potential tested and H_2O_2 formation was not detected until a cathodic potential of -0.5 V vs Ag/AgCl. Under anodic conditions both H_2O_2 and Cl-based oxidants were formed in the PBS solution at anodic potentials of $\geq$ 0.5 V vs Ag/AgCl. The Cl-based oxidants (e.g., $Cl^{\bullet}$) were likely a primary contributor to bacteria poration. While prior studies have shown that H_2O_2 is a weak disinfectant [33], the reactions between H_2O_2 and Cl-based oxidants could produce various other oxidants that contributed to bacterial poration.

3.6 Acknowledge

Funding for this work was provided by two National Science Foundation awards to B.P. Chaplin (CBET-1453081; CBET-1604776).

4. Bacteria Poration on Modified Boron-Doped Diamond Electrode Surfaces Induced by Divalent Cation Chelation

4.1 Abstract

This research investigated mechanisms for biofouling control at modified boron-doped diamond (BDD) electrode surfaces polarized at low applied potentials (e.g., -0.2 to 1 V versus Ag/AgCl), using *Pseudomonas aeruginosa* (PAO1) as a model pathogenic organism. Results indicated that electrostatic interactions and electrochemical reactions under polarized conditions can affect cell attachment and poration, respectively. However, results suggested that divalent ions from the outer membrane of PAO1 can be chelated by N-propyl-2-hydroxyacetamide functional groups that were immobilized on a BDD optically transparent electrode (termed OH-BDD/OTE). It was observed that two- to three-fold higher percentage of porated bacteria were observed on the OH-BDD/OTE compared with BDD/OTE under applied anodic potentials between 0.1 to 0.5 V vs Ag/AgCl. Density functional theory calculations indicated that the chelation mechanism was thermodynamically favorable. Zeta potential measurements of the PAO1 bacteria as a function of chelator and Mg^{2+} concentrations were performed and interpreted using a mathematical model based on the nonlinear Poisson-Boltzmann equation. Results supported the chelation mechanism for bacteria poration, which indicates that electrode modification may be a viable method to prevent biofouling of electrode surfaces that are operated at low applied potentials.

4.2 Introduction

The interaction between microorganisms and surfaces has become a focal point of scientific investigations in both natural and engineered settings. Bacteria can often have negative impacts in several industries, such as water treatment and distribution [46], food [125, 126], and medical device implants [48, 127]. These industries spend significant time and resources to combat the growth of biofilms on pipes, heat exchangers, membranes, medical tools and implants, and other surfaces [1–3]. As a result, it is important to understand methods and mechanisms that control bacteria attachment and cause inactivation.

Electrochemical techniques have emerged as potentially effective biofouling control strategies [10, 14, 33, 128–130]. However, high cell potentials (e.g., > 5.0 V) are often needed to generate sufficient disinfectant concentrations [45]. Therefore, electrochemical techniques are not always cost effective due to high power consumption, and other electrochemical water treatment methods, such as capacitive deionization [27, 131], experience biofouling due to their low operating cell potentials (e.g., ~ 1.0 V). Recent work has shown that reactive oxygen species (ROS) and Cl-based oxidants can be generated at electrode surfaces at low-applied potentials ($\leq |1.0|$V vs. Ag/AgCl), and can cause poration of bacterial cell membranes [132]. However, there is still a need to develop strategies that increase antimicrobial activity of electrode surfaces at low cell potentials for effective biofouling control.

Several studies have shown that chelators such as citrate, phosphate, ethylene-bis(oxyethylenenitrilo)tetraacetic acid (EGTA), ethylenediaminetetraacetic acid (EDTA), and hexametaphosphate possess antibacterial activity [54, 57, 133]. These chelators extract Mg^{2+}, Ca^{2+} and other divalent ions from the lipopolysaccharides (LPS) of the cell membrane, which causes membrane destabilization [134, 135]. Studies have shown that chelators can be immobilized on

surfaces to impart antimicrobial activity. For example, EDTA was used to inactivate *P. aeruginosa* amd *Salmonella enterica serovar* bacteria by chelating Mg^{2+}, Ca^{2+}, and Fe^{2+} from their cell membranes [55, 133]. In addition, polyphosphate has also been shown to chelate divalent cations from the cell membrane of *Bacillus cereus,* which caused growth inhibition and cell lysis [136]. Chelator coatings on electrodes have been studied and applied for biosensing purposes [137–139] and as electrocatalysts [140]. However, to our knowledge this strategy has not been tested on electrode surfaces for antimicrobial control during water treatment.

In this study we investigated the attachment and antimicrobial properties of functionalized electrode surfaces under low applied potentials between -0.2 and 1.0 V vs Ag/AgCl. BDD electrodes were used as model stable electrode surfaces and modified with N-propyl-2-hydroxyacetamide groups to produce distinct chelation sites. These modified electrodes were tested for their antibacterial activity using *Pseudomonas aeruginosa* (POA1) as a model biofilm forming bacteria, which is a known opportunistic pathogen that causes severe acute and chronic infections within the urinary and respiratory tracts of humans [141]. The electrode surfaces were characterized by cyclic voltammetry (CV) and X- ray photoelectron spectroscopy (XPS), and POA1 attachment and poration studies were conducted as a function of the applied potential and Mg^{2+} concentration. Experimental results suggested that the N-propyl-2-hydroxyacetamide groups acted as divalent chelation sites that caused bacteria poration, which were supported by density functional theory (DFT) calculations. Zeta potential measurements of the PAO1 bacteria as a function of chelator and Mg^{2+} concentrations were performed and interpreted using a mathematical model based on the nonlinear Poisson-Boltzmann equation. These results supported the chelation mechanism for bacteria poration.

4.3 Materials and Methods

4.3.1 Reagents

Sodium perchlorate ($NaClO_4$), phosphate buffer saline (PBS, with compositions of with composition of 137 mM NaCl, 2.7 mM KCl, 10 mM Na_2HPO_4 and 1.8 mM KH_2PO_4),glycolic acid (GA), magnesium chloride hexahydrate ($MgCl_2 \cdot 6H_2O$), potassium hexacyanoferrate (III) ($K_3[Fe(CN)_6]$), potassium hexacyanoferrate (II) ($K_4[Fe(CN)_6]$), hexaammineruthenium (II) chloride ($Ru(NH_3)_6Cl_2$), hexaammineruthenium (III) chloride ($Ru(NH_3)_6Cl_3$), glycolic acid (GA), and 4-morpholinoethanesulfonic acid (MES) were purchased from Sigma-Aldrich (St. Louis, MO USA). Ethylenediaminetetraacetic acid and disodium salt dihydrate (EDTA) were purchased from Fisher Chemistry (MA, USA). N-hydroxysuccinimide (NHS) was purchased from Chem-Impex International (IL, USA). (3-Aminopropyl) triethoxysilane, 98% (APTES), and 1-(3-Dimethylaminopropyl)-3-ethylcarbodiimide (EDC) were purchased from Alfa Aesar (MA, USA). Tryptone was purchased from IBI Scientific (IA, USA). Granulated yeast extract and Drisolv® toluene anhydrous were purchased from EMD Millipore (USA). The viability/cytotoxicity assay kit was purchased from Biotium (Fremont, CA USA). Solutions were made from Elga purelab flex ultrapure deionized (DI) water (18.2 MΩ cm at 21°C). The POA1 bacteria was isolated from a patient at the University of Washington [97]. All chemicals were used as received.

4.3.2 Electrode Preparation

Optically transparent electrodes (OTEs) were fabricated at Fraunhofer USA Center for Coatings and Diamond Technologies (East Lansing, MI, USA). A boron-doped diamond (BDD) microcrystalline film was deposited on a 2 mm thick quartz glass substrate by hot filament chemical vapor deposition (CVD) and was cut into 1 cm^2 disks using a laser cutting system. The

BDD/OTE electrode was pretreated anodically in 1 M $NaClO_4$ (20 mA cm^{-2} for 20 min) to terminate it with -OH groups [142]. The pretreated BDD/OTE was rinsed sequentially with ethanol, methanol, and water. Next, the cleaned BDD/OTE was placed in an Ar-filled glove box and immersed in 5 mM APTES in anhydrous toluene for 3 hours. The APTES functionalized BDD/OTE (APTES-BDD/OTE) was then rinsed three times with toluene and methanol and annealed at 120°C for 30 min to promote cross-linking of the silanes [100], [101]. The N-propyl-2-hydroxyacetamide modified BDD electrode (OH-BDD/OTE) was prepared from an APTES-BDD/OTE using GA and the EDC/NHS method. The chemical structure of the OH-BDD/OTE functional group is shown in **Figure 4-1**. Details of the electrode functionalization methods are provided in the Appendices (**Appendix B**, **Figure B-1**).

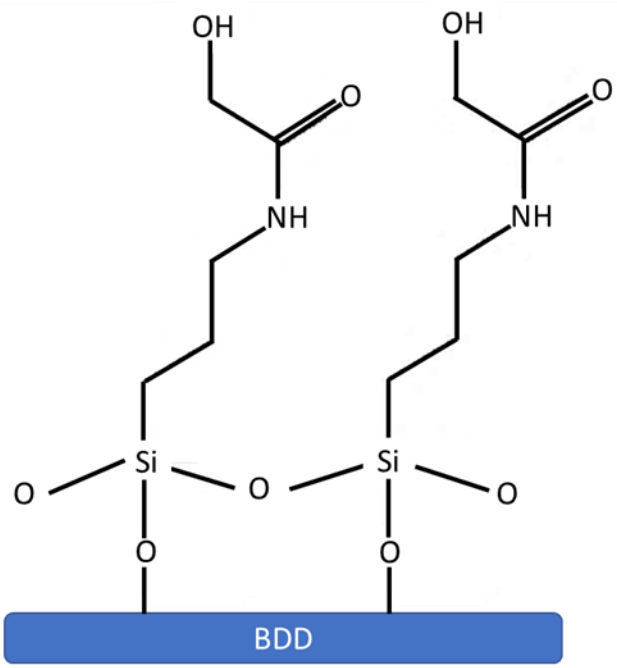

Figure 4- 1. The structure of N-propyl-2-hydroxyacetamide modified BDD (OH-BDD/OTE).

4.3.3 *Electrode Characterization*

The OTEs were characterized by CV, XPS (Kratos Axis-165), and contact angle measurements. The CV scans were performed with two different ionic redox couples (5 mM $K_3Fe(CN)_6/K_4Fe(CN)_6$ and 5 mM $Ru(NH_3)_6Cl_3/Ru(NH_3)_6Cl_2$ at 1:1 molar ratios) in the PBS background electrolyte (pH = 7.4) to evaluate the charge transfer between the redox couples and the OTE surfaces. The potential was swept at a scan rate of 100 mV s^{-1}. Contact angle measurements were obtained by Image J software with DropSnake plugin [102].

4.3.4 *Bacteria Growth Media and Culture Conditions*

The POA1 bacteria cells were transferred from a stock solution and cultured in lysogeny broth (LB), which contained 10 g tryptone, 5 g yeast extract, and 10 g NaCl in 1 L of DI water. The culture was incubated at 37° C on a rotary shaker at 160 rotations per minute (rpm) for 16 hours, which corresponded to late-log phase of bacteria growth [103]. After incubation, bacteria cells were washed three times in PBS by centrifugation at 7000×g for 5 min at room temperature. The concentration of the bacteria in the solution was quantified by optical density (OD) at 600 nm (OD_{600}). Direct plate counts were performed, and a standard curve was constructed of OD versus plate count numbers (**Appendix B**, **Figure B-2**). The bacteria cell concentration was determined to be approximately 1×10^9 cells mL^{-1} at an OD_{600} value of 1.0.

4.3.5 *Dual Staining Procedure*

The bacteria counts were made with a viability/cytotoxicity assay kit according to the manufacture's protocol (Biotium, USA). Prior to staining, bacteria were washed three times with a 0.85% NaCl solution. The viability/cytotoxicity assay was prepared by mixing 10 µL of DMAO, 20 µL of Ethidium Homodimer-III (EthD-III), and 80 µL of 0.85% NaCl. DMAO is a green dye

capable of staining nucleic acids in both intact and porated bacteria cells (excitation 503 nm/ emission 530 nm). The EthD-III red dye (excitation 530 nm/ emission 620 nm) selectively stains cells with a porated outer membrane. Mixed reagent solutions were prepared freshly before each experiment. A 1 μL volume of reagent solution was added to each 100 μL of PBS washed bacteria suspension. The bacteria were incubated in the reagent solution at room temperature without light irradiation for 15 minutes. A cover slide was placed over the OTE after staining and the cells were imaged at 10 individual random spots (128 by 128 μm area) using an inverted fluorescent microscope (Olympus IX73, Japan) with band-pass filter sets, which have blue wide pass with excitation 460-495 nm; emission 510-550 nm (FITC filter), and green wide long pass with excitation 530-550 nm; emission 575 nm (TRITC filter).

4.3.6 Bacteria Attachment/Poration Studies

The POA1 cells were washed and resuspended in a centrifuge tube with PBS to ~ 10^9 cells mL^{-1} and transferred to a 2 mL Teflon® cell for attachment/poration studies (**Figure 4-2**). The OTEs were used as working electrodes and sealed at the bottom of the SECM holder with an o-ring and a titanium foil was used as a current collector. A Pt wire was used as a counter electrode and a Ag/AgCl electrode was used as a reference. Potentials and currents were controlled and monitored with a bipotentiostat (CHI920D model, CH Instrument, Inc). Each experiment was conducted for 105 minutes at a constant potential (-0.2 V to 1.0 V vs. Ag/AgCl). For studying the effect of divalent cations on bacteria inactivation, different concentrations of Mg^{2+} (5, 10, 15, 20 mM) were added into the PBS solution and cathodic/anodic potentials were applied on the OTEs. Every experiment was repeated three times and all reported errors and error bars represent the standard deviation about mean values.

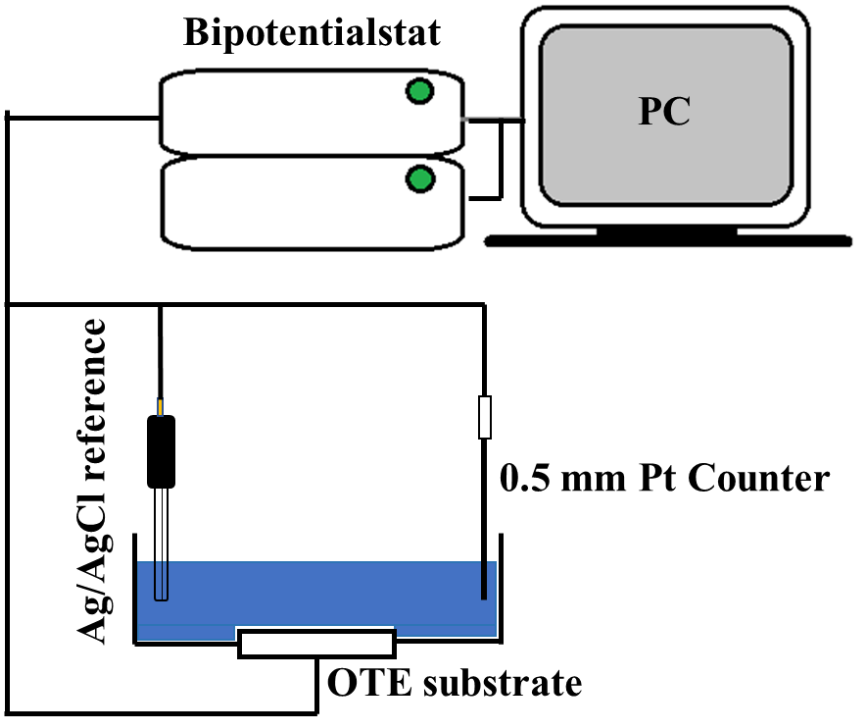

Figure 4- 2. Experiment setup including OTE substrate, reference electrode and platinum counter electrode with bipotentiostat.

4.3.7 Bacteria Surface Charge Measurements

The PAO1 zeta potentials were measured as a function of solution conditions using electrophoretic light scattering (Nano-ZS, Malvern). The POA1 cells (~ 10^9 cells mL^{-1}) were washed and resuspended in a 20 mL beaker with PBS. Small amounts of EDTA or GA as chelators were added into the glass vial continuously by auto titration (MPT-2, Malvern), and solution pH was monitored and recorded simultaneously. Solution phase experiments were conducted with planktonic bacteria to determine the effect of GA and EDTA as chelators in the presence of Mg^{2+} (0 - 30 mM).

4.3.8 Bacteria Titration Experiments

The titration experiments were conducted to determine the charge regulation on the bacteria cell surface [143, 144]. The bacteria were grown in the LB to stationary phase. A concentration of ~1×1010 cells mL-1 was suspended in a beaker with 5 mL of 0.1 M NaCl, which was adjusted to pH 11 by 0.1 N NaOH addition. The concentration of bacteria was determined by OD_{600} as shown in **Appendix B, Figure B-3**. A 0.1 N HCl solution was titrated into the beaker and solution pH was monitored and recorded. Bacteria were transported continuously into disposable capillary cells for surface potential measurements using a zetasizer (Nano-ZS, Malvern). The titration results were used to estimate the dissociation constants (K_{a_i}) and their corresponding site numbers (N_{a_i}) of acidic and basic functional groups on the bacteria cell surface. Details are shown in the **Appendix B**.

4.3.9 Quantum Mechanical Calculations

Density functional theory (DFT) calculations were performed to determine the Gibbs free energy for adsorption of Mg^{2+} at the 2-hydroxyacetamide functional group. Simulations were performed using Gaussian 16 software [145]. Unrestricted spin, all-electron calculations were performed using the 6-31G+(d) basis set for geometry optimization, frequency, and energy calculations. A scale factor of 0.9806 was used to correct for known systematic errors [136]. The gradient corrected Becke, three- parameter, Lee−Yang−Parr (B3LYP) functional was used for exchange and correlation. Implicit water solvation was incorporated using the SMD model [146].

4.3.10 Mathematical Model

To interpret bacteria poration, chelation of metallic ions on the cell surface, and surface charge measurements, we developed a mathematical model based on the nonlinear Poisson-

Boltzmann Equation, which estimates the distribution of counter ions near the charged cell surface [147]. Using the Henderson-Hasselbalch equation for PBS, GA, and EDTA under different pH conditions, the model accounts for protonation/deprotonation of acidic groups, and chelation of divalent cations at fixed sites on the cell surface. We assumed that these cations are subject to both an attractive non-electrostatic and electrostatic interaction potential from the cell membrane [148]. We also hypothesized that bacterial surface charges arise from carboxylic, hydroxyl, and phosphoric groups, which yield the pH dependence [144].

Ignoring the radius of curvature of the cell surface and considering the cell surface as a flat ion-penetrable layer with finite thickness (r_d), where there are not any basic groups, we described the electric potential distribution with respect to distance from the cell surface by [148] :

$$\frac{d^2y}{dx^2} = \begin{cases} -\rho - c_0 \sum_i z_i n_i e^{(-z_i y)}, & x < x_d \\ -c_0 \sum_i z_i n_i e^{(-z_i y)}, & x \geq x_d \end{cases} \quad (4\text{-}1)$$

where $y = e\,\psi/kT$ and ψ are the dimensionless and dimensional electric potentials, respectively; e is the charge of an electron; kT is the thermal energy; $x = r/\kappa$ is the dimensionless distance from the ion-impenetrable core of the cell surface; $x_d = r_d/\kappa$; $\kappa = \sqrt{(\epsilon_w \varepsilon_0 kT)/(e^2 N_A \sum_i z_i^2 n_i)}$ is the Debye-Huckel length; n_i is the molar concentration of ions of type *i*; N_A is the Avogadro's number; z_i is the valence of ions of type *i*; ϵ_w is the dielectric constant of the bulk; ε_0 is the permittivity of the vacuum; and $c_0 = (\kappa^2 e^2 N_A)/(\epsilon_w \varepsilon_0 kT)$.

In equation (4-1), ρ is the density of static charges in the ion-penetrable layer of the cell surface, which can be defined by protonation and deprotonation of ionizable acidic groups according to the following equilibrium reactions [144, 149, 150] :

$$\mathrm{R}_{a_i}\mathrm{H} \leftrightharpoons \mathrm{R}_{a_i}^- + \mathrm{H}^+ \quad (4\text{-}2)$$

and the adsorption of divalent cations is given by [144] :

$$\mathrm{R}_{a_i}\mathrm{M}^{+} \leftrightharpoons \mathrm{R}_{a_i}^{-} + \mathrm{M}^{2+} \tag{4-3}$$

where $\mathrm{R}_{a_i}^{-}$ indicates ionizable acidic groups of type *i*, namely, phosphoric, carboxylic, and hydroxyl groups, and M^{2+} represents the divalent cations. The static charge density in the ion-penetrable layer is given by:

$$\rho = \frac{\kappa^2 e^2}{kT\epsilon_0\epsilon_w}\left\{-\sum_i \frac{N_{a_i}K_{a_i}}{k_{a_i}+[\mathrm{H}^+]e^{-y}+\frac{K_{a_i}}{K_M}[\mathrm{M}^{2+}]e^{-2y}} + \frac{\frac{K_{a_i}}{K_M}[\mathrm{M}^{2+}]e^{-2y}}{k_{a_i}+[\mathrm{H}^+]e^{-y}+\frac{K_{a_i}}{K_M}[\mathrm{M}^{2+}]e^{-2y}} - 2\frac{[\mathrm{H_2Y}^{2-}]N_d e^{2y-\Delta g}}{1+[\mathrm{H_2Y}^{2-}]e^{2y-\Delta g}}\right\} \tag{4-4}$$

where the last term represents adsorption of $\mathrm{H_2Y}^{2-}$ on to the ion-penetrable layer, and chelation of a metallic ion by the displacement of the weakly acidic protons using a modified Langmuir isotherm [149, 151, 152], as shown in **Figure 4-3**. The adsorption is occurring according to the following reaction:

$$\mathrm{M}^{2+} + \mathrm{H_2Y}^{2-} \leftrightharpoons \mathrm{MY}^{2-} + 2\mathrm{H}^{+}. \tag{4-5}$$

In equation (4-4), $[\mathrm{H}^+]$, $[\mathrm{M}^{2+}]$, and $[\mathrm{H_2Y}^{2-}]$ are the concentrations of the hydrogen ions, divalent cations, and dissociated divalent chelator anions, respectively; N_{a_i} and N_d are the number of acidic sites of type *i*, and adsorption sites for chelation per unit volume, respectively; K_{a_i} and K_M are dissociation constants of acidic group of type *i* and binding constants of adsorbed divalent cations, respectively; and Δg is the Gibbs energy of specific interaction nondimensionalized by kT. Equation (4-1) is subjected to the following boundary conditions

$$\left.\frac{dy}{dx}\right|_{x=0} = 0, \quad y|_{x=\infty} = \left.\frac{dy}{dx}\right|_{x=\infty} = 0, \quad \lim_{x\to x_d^+} y = \lim_{x\to x_d^-} y, \tag{4-6}$$

where $x = 0$ indicates the ion-impenetrable core of the cell surface, and $x = \infty$ represents the bulk solution. Using the finite difference scheme with the direct discretization of the derivative terms, we solved equation (4-1) numerically to find dimensionless zeta potential, y, where we applied the boundary conditions in equation (4-6) via a shooting method, and assumed the thickness of ion-penetrable layer to be $r_d = 5$ nm. We used a fully nonlinear optimization to find the model parameters (N_{a_1} to N_{a_4}, N_d, K_{a_1} to K_{a_4}, K_M, and Δg) by fitting the zeta potentials from the model to those from the experimental measurements.

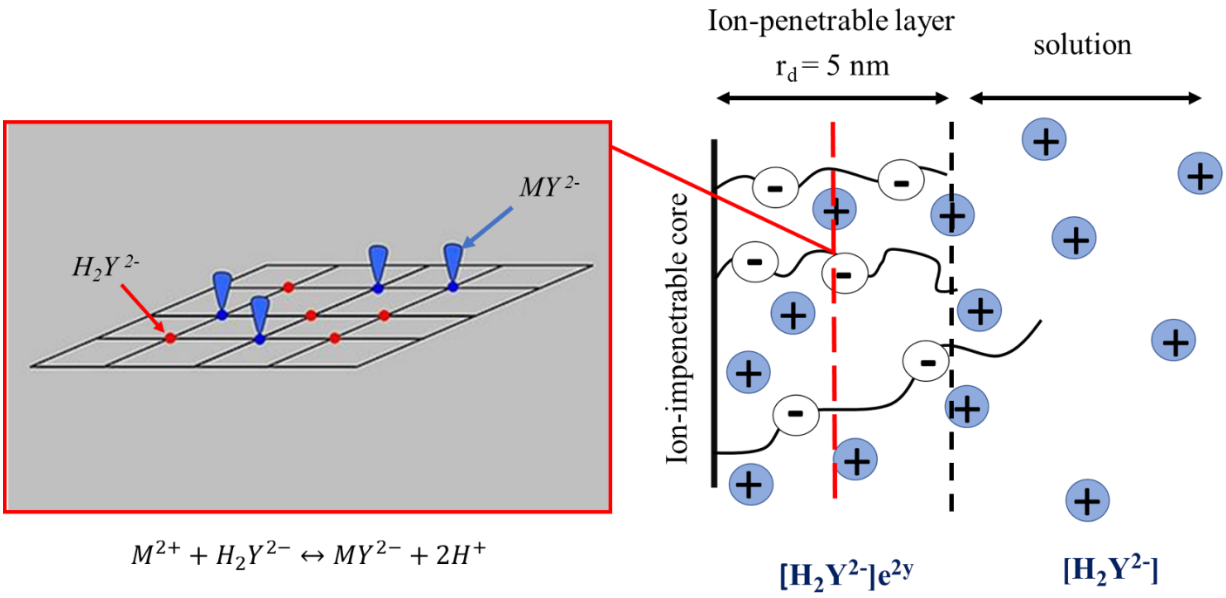

Figure 4- 3. Schematic presentation of a charge profile of bacteria surface and divalent ions binding sites in the ion-penetrable layer. Left panel: red circles represent binding sites occupied by protons and blue symbols represent binding sites where a M^{2+} cation is present.

4.4 Results and Discussion

4.4.1 Electrode Characterization

Two different electrode surfaces (i.e., BDD/OTE and OH-BDD/OTE) were characterized using CV scans to determine the effect of surface functional groups on the charge transfer reactions

with aqueous ionic redox couples (**Figure 4-4**). The CV scans in the PBS electrolyte illustrated that the average charging currents on BDD/OTE and OH-BDD/OTE were 29 μA and 16 μA, respectively, at a potential of 0 V vs. Ag/AgCl (**Figure 4-4a**). These results indicated that the reactive surface area decreased by ~ 45% after electrode modification, likely due to a blockage of active sites by the functionalization process. Therefore, more work is needed to develop these coatings so that reactive surface area is not compromised, but the bacteriostat properties of the coatings are anticipated to prevent biofilm growth, which if not addressed can result in the complete blockage of the electrode surface. CV scans containing 5.0 mM of the $Fe(CN)_6^{3-/4-}$ inner sphere redox couple showed a lower current for the OH-BDD/OTE relative to the BDD/OTE and a positive shift in the formal electrode potential (**Figure 4-4b**). These results were attributed to repulsive electrostatic interactions between the anionic redox couple and the negative dipoles of the oxygen atoms in the 2-hydroxyacetamide functional groups. Thereby, increasing the surface concentration of the oxidized redox species relative to the reduced one. The charge transfer of the $Fe(CN)_6^{3-/4-}$ inner sphere redox couple is very sensitive to surface termination of the electrodes [64, 153, 154]. By contrast, the peak current was only slightly reduced at the OH-BDD/OTE relative to the BDD/OTE with the 5 mM $Ru(NH_3)_6^{2+/3+}$ redox couple (**Figure 4-4c**). The results indicated that the $Ru(NH_3)_6^{2+/3+}$ outer sphere redox couple was less sensitive to electrostatic interactions than the inner sphere redox couple [154]. Also, the peak separation of both redox couples were approximately the same for both electrodes, indicating that only access of the redox couples to the electrode surface were affected and that the charge transfer kinetics were not greatly affected by the functionalization process. The BDD/OTE had a hydrophilic surface [64], with a measured contact angle of 45 degrees (**Figure 4-4d**). The OH-BDD/OTE electrode had a more hydrophobic surface with a measured contact angle of 65 degrees (**Figure 4-4d**).

To determine the stability of the electrode modification under the potential range of the experiments (-0.2 to 1.0 V vs. Ag/AgCl), CV scans were performed for the OH-BDD/OTE after a total anodic charge of 256 C and cathodic charge of -129 C were applied to the electrode. The CV scans showed similar results for the $Fe(CN)_6^{3-/4-}$ and $Ru(NH_3)_6^{2+/3+}$ redox couples before and after this "ageing" process (**Appendix B, Figure B-4**), indicating that the surface modification was stable in the potential range of -0.2 to 1.0 V vs. Ag/AgCl.

The surface chemistry of the OTEs were analyzed by XPS and results are shown in **Figure 4-5** and **Table 4-1.** The C1s spectrum assignments were based on previous literature data [99]. The BDD/OTE contained primarily C-H (C1 = 42%), C-C (C2 = 21%), and C-OH (C4= 19%) functionalities. By contrast, a significant proportion of the C-C (C2 = 93.2%), C-O/C=O/-$(CH_2CH_2NH)_n$- (C3 = 4.2%), and -COOH (C5 = 2.6%) groups were detected on the OH-BDD/OTE. The peak area ratios for C/O, C/N, and C/Si are shown in **Table 4-1b**. The C/O ratios were similar for both OTEs (5.9 for BDD/OTE and 4.1 for OH-BDD/OTE), but the C/N ratios (59.5 for BDD/OTE and 17.2 for OH-BDD/OTE) and C/Si ratios (64.5 for BDD/OTE and 17.4 for OH-BDD/OTE) decreased due to 2-hydroxyacetamide functionalization. Comparing the C/N and C/Si ratios before and after functionalization provided an estimate of ~ 77% surface coverage of the 2-hydroxyacetamide functional groups on the BDD surface (see **Appendix B** for details).

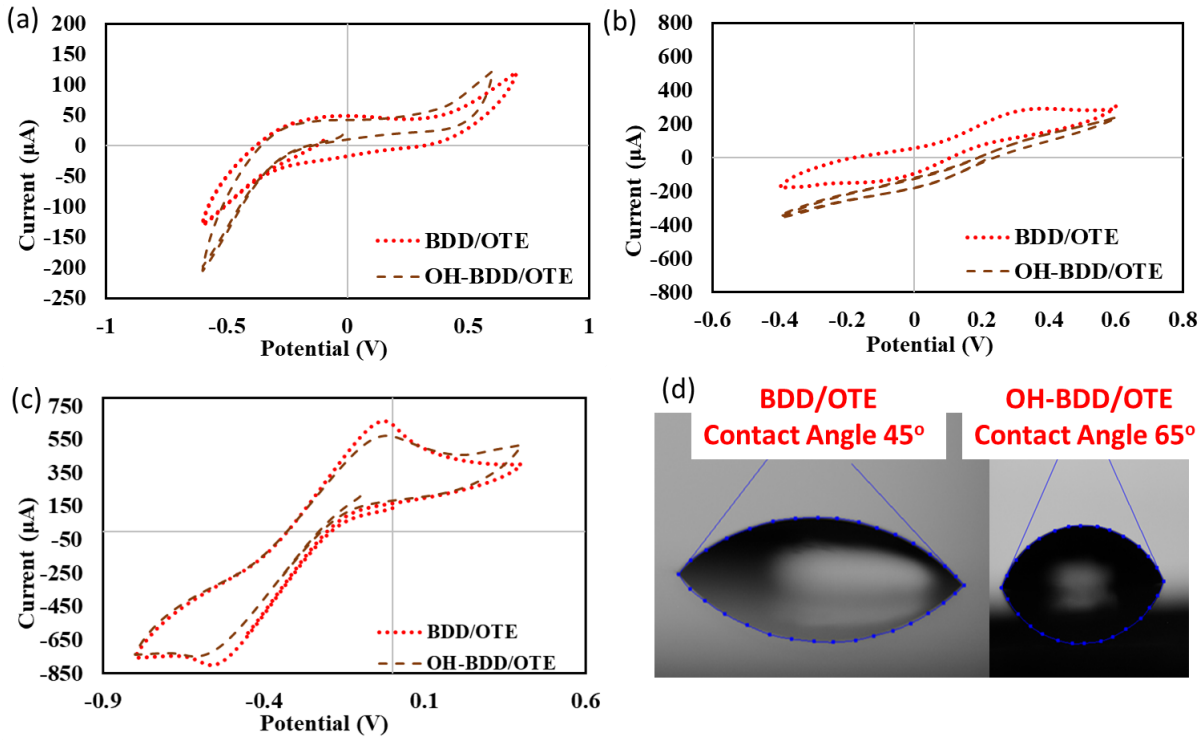

Figure 4- 4. Cyclic voltammogram (CV) curves of bare BDD/OTE and OH-BDD/OTE in the (a) phosphate buffer saline (1x PBS), pH = 7.4 (b) PBS containing 5 mM $K_3Fe(CN)_6/K_4Fe(CN)_6$ and (c) PBS containing 5mM $Ru(NH_3)_6Cl_3/Ru(NH_3)_6Cl_2$. (V v.s Ag/AgCl) (d) contact angles of BDD/OTE and OH-BDD/OTE.

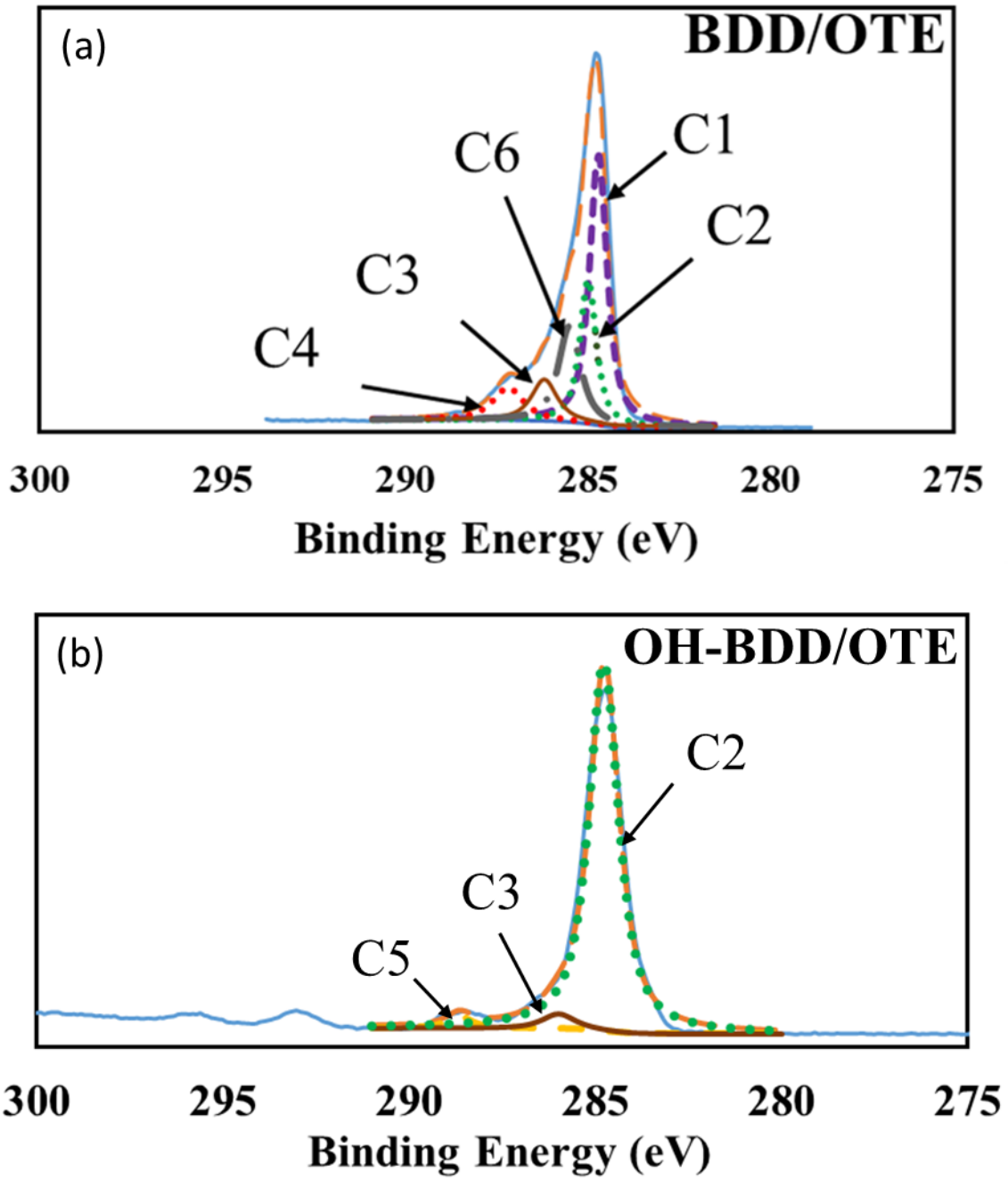

Figure 4- 5. XPS spectra analysis of (a) BDD/OTE and (b) OH-BDD/OTE. C1 purple, C2 green, C3 brown, C4 red, C5 yellow, C6 grey and orange line for total peak area.

Table 4- 1. (a) Summary of XPS peaks and (b) elements ratio on both OTEs determined by XPS.

(a)

Peak Label	Binding energy (eV)	Possible functional groups	Surface Coverage BDD/OTE (%)	Surface Coverage OH-BDD/OTE (%)	Reference
C1	284.6 ± 0.15	C-H	41.9	0	[99]
C2	285.1 ± 0.3	C-C	20.8	93.2	[99]
C3	286 ± 0.3	C-O/C=O/ -$(CH_2CH_2NH)_n$-	9.1	4.2	[108]
C4	286.4 ± 0.3	C-OH	18.8	0	[99]
C5	288.7±0.15	-COOH	0	2.6	[99]
C6	285.5	C-NH	9.3	0	[109]

(b)

Elements ratio on both OTEs.	BDD/OTE	OH-BDD/OTE
C/O	5.9	4.1
C/N	59.5	17.2
C/Si	64.5	17.4

4.4.2 Bacteria Attachment/ Poration Studies

Results for bacteria attachment numbers and the percentages of porated cells as a function of the applied potential on the OTEs are shown in **Figure 4-6a** and **Figure 4-6b**, respectively. These values were determined by averaging the direct count of 10 random locations on each sample. Initially, approximately 10^9 cells mL^{-1} were suspended in the bulk solution with a total solution volume of 2 mL. The currents on both OTEs were similar, but the attached cell numbers were higher on the OH-BDD/OTE, except for applied potentials of 0.8 and 1.0 V vs Ag/AgCl **(Figure 4-6a)**. These results suggested that the functionalization of the OH-BDD/OTE provided

additional adsorption sites for bacteria, possibly due to a higher hydrophobicity. However, at the higher anodic potentials, the formation of oxygen bubbles likely offsets this difference.

The attached cells were analyzed for their membrane integrity using fluorescent microscopy (**Figure 4-6b)**. In general, the percentage of bacteria with membrane damage increased upon increases in anodic and cathodic potentials on the BDD/OTE (**Figure 4-6b**). These results were attributed to basic and acidic local pH environments due to water electrolysis under cathodic and anodic potentials, respectively, and the formation of ROS and reactive chlorine species [132]. However, two- to three-fold higher percentage of porated bacteria were observed on the OH-BDD/OTE compared with BDD/OTE under applied anodic potentials between 0.1 to 0.5 V vs Ag/AgCl **(Figure 4-6b)**, suggesting that other mechanisms may be responsible for bacteria inactivation under these conditions.

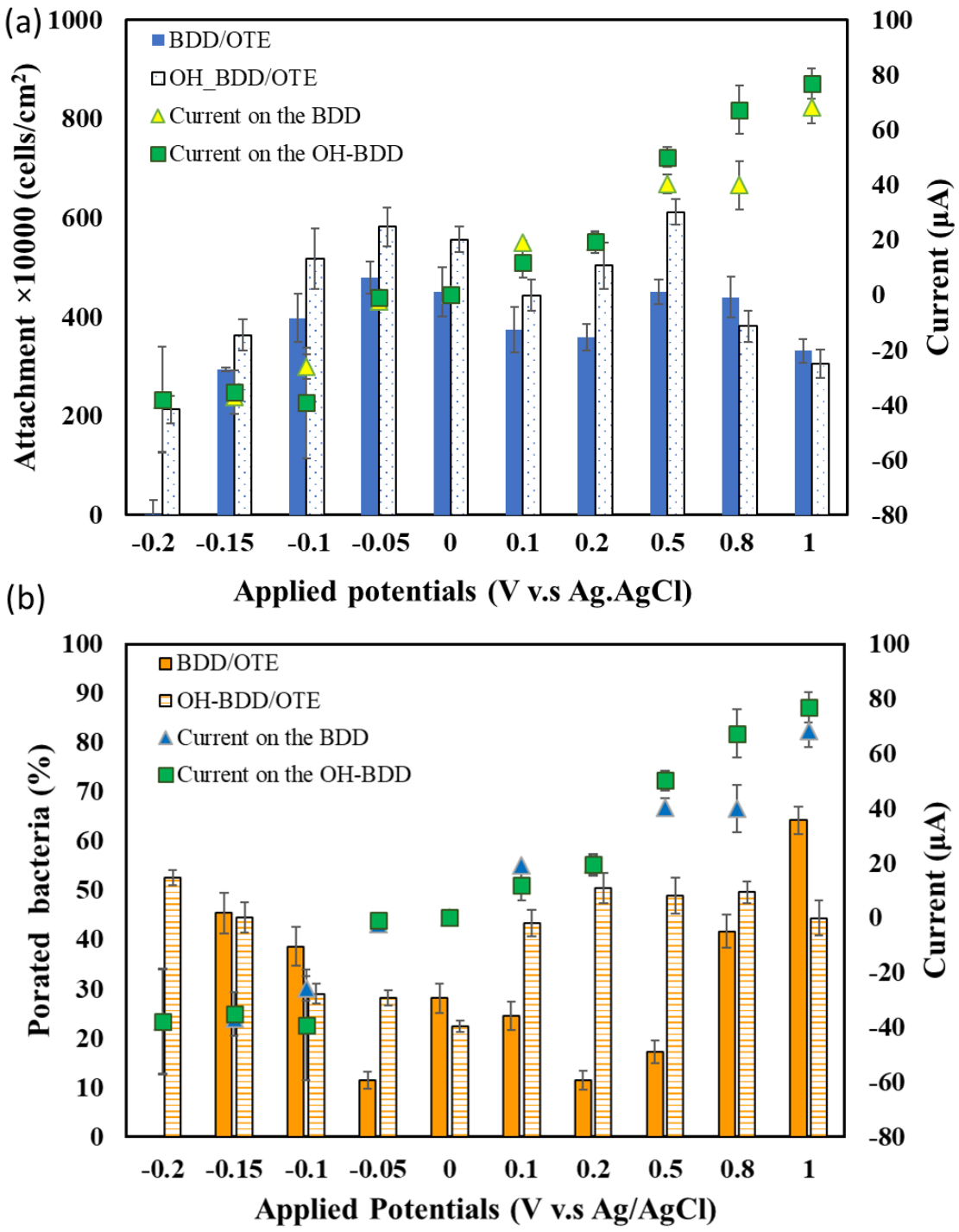

Figure 4- 6. Comparison of the (a) bacteria total attachment number and (b) percentage of porated bacteria (bars) on the two different substrates as a function of the applied potential. Measured currents given as data points.

One possible mechanism for destabilization of the bacteria membrane is chelation of the divalent cations from charge balancing sites. The cell membrane consists of $-COO^-$, $-HPO_4^-$, and $-PO_4^{2-}$ functional groups on the polyanionic LPS [155], which are neutralized and mechanically stabilized by divalent cations such as Ca^{2+} and Mg^{2+} [156]. The structure of the 2-hydroxyacetamide functional group on the OH-BDD/OTE provides a possible site that can chelate divalent cations from the LPS and cause bacterial membrane damage. DFT simulations were performed to provide evidence for the existence of this chelation site. The Gibbs free energy for adsorption of Mg^{2+} at the 2-hydroxyacetamide functional group was calculated as ΔG = -180 kJ mol^{-1} (**Figure 4-7**). These results support the hypothesis that divalent cation chelation by the OH-BDD/OTE was thermodynamically favorable.

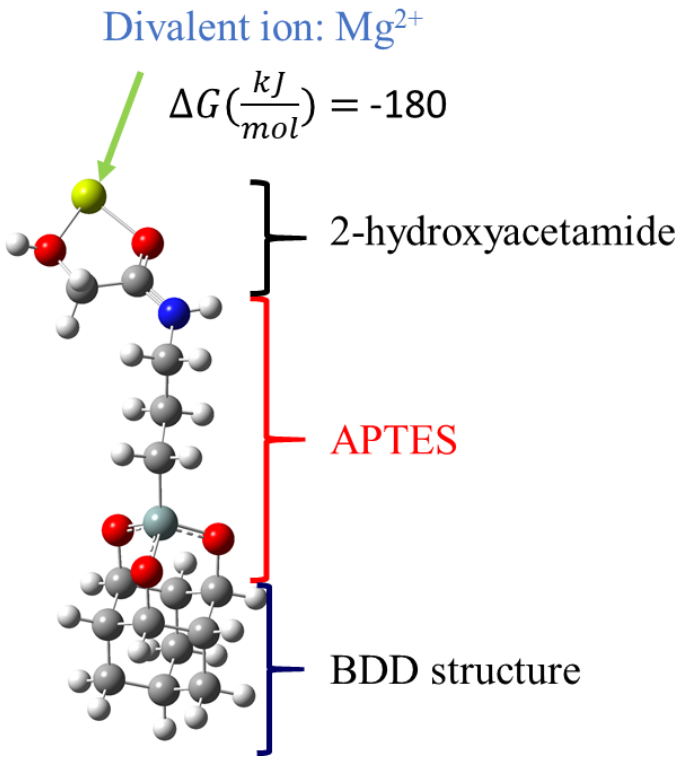

Figure 4- 7. Optimized geometry of adsorption of Mg^{2+} at the 2-hydroxyacetamide functional group of the OH-BDD/OTE determined by DFT simulations. Atom key: Oxygen = red; Carbon = gray; Nitrogen = blue; Silicon = dark-grey; Magnesium = yellow; Hydrogen = white.

However, the DFT results do not provide evidence that this chelation effect is strong enough to remove divalent cations from the LPS. To support this possibility, various Mg^{2+} concentrations were added into the 2 mL Teflon® cell under applied potentials of 0.2 V and -0.15 V vs. Ag/AgCl for both the BDD/OTE and OH-BDD/OTE (**Figure 4-8**). The results in **Figure 4-8a** show that under an applied anodic potential of 0.2 V vs. Ag/AgCl and in the absence of Mg^{2+}, the percentage of viable bacteria, which is defined as bacteria with uncompromised cell membranes, was 82 ± 2.0% on the BDD/OTE and 53.3 ± 1.7% on the OH-BDD/OTE. Upon the addition of Mg^{2+} to solution (5 to 15 mM) the percentage of viable bacteria significantly increased for both OTEs (**Figure 4-8a**). The percentage of viable bacteria increased from 53.3 ± 1.7% to 92.4 ± 2.7% on the OH-BDD/OTE and increased from 82 ± 2.0% to 89 ± 3.3% on the BDD/OTE. This result may be due to the ability of the additional Mg^{2+} ions to stabilize the cell membrane. By contrast, upon the addition of Mg^{2+} to solution with a polarization of -0.15 V vs. Ag/AgCl, the percentage of viable bacteria significantly increased from 55 ± 4.1% % to 75 ± 4.5% on BDD/OTE, but was approximately constant on the OH-BDD/OTE with and without the presence of Mg^{2+} (**Figure 4-8b**). For example, the percentage of viable bacteria was 55 ± 5.02% on the OH-BDD/OTE without the addition of Mg^{2+} and were 62.4 ± 4.8%, 60.0 ± 4.5%, and 57.9 ± 4.2% with Mg^{2+} concentrations of 5, 10, and 15 mM, respectively (**Figure 4-8b**). These results suggest that both the applied potential and the Mg^{2+} concentration both play roles in the bacteria poration process. It is hypothesized that when the OTE is polarized as a cathode, the electric double layers of the adsorbed POA1 cells and the OTEs begin to overlap [157]. Therefore, there is a three-way competition for Mg^{2+} ions between the 2-hydroxyacetamide chelation sites, PAO1 bacteria, and the OTE double layer. Apparently under cathodic conditions the Mg^{2+} ions are more thermodynamically favorable (or kinetically trapped) at the chelation sites and OTE double layer

over the PAO1 surface. It was beyond the scope of work to investigate this mechanism in further detail in this study. However, more experimental and theoretical work is needed to test the proposed hypothesis.

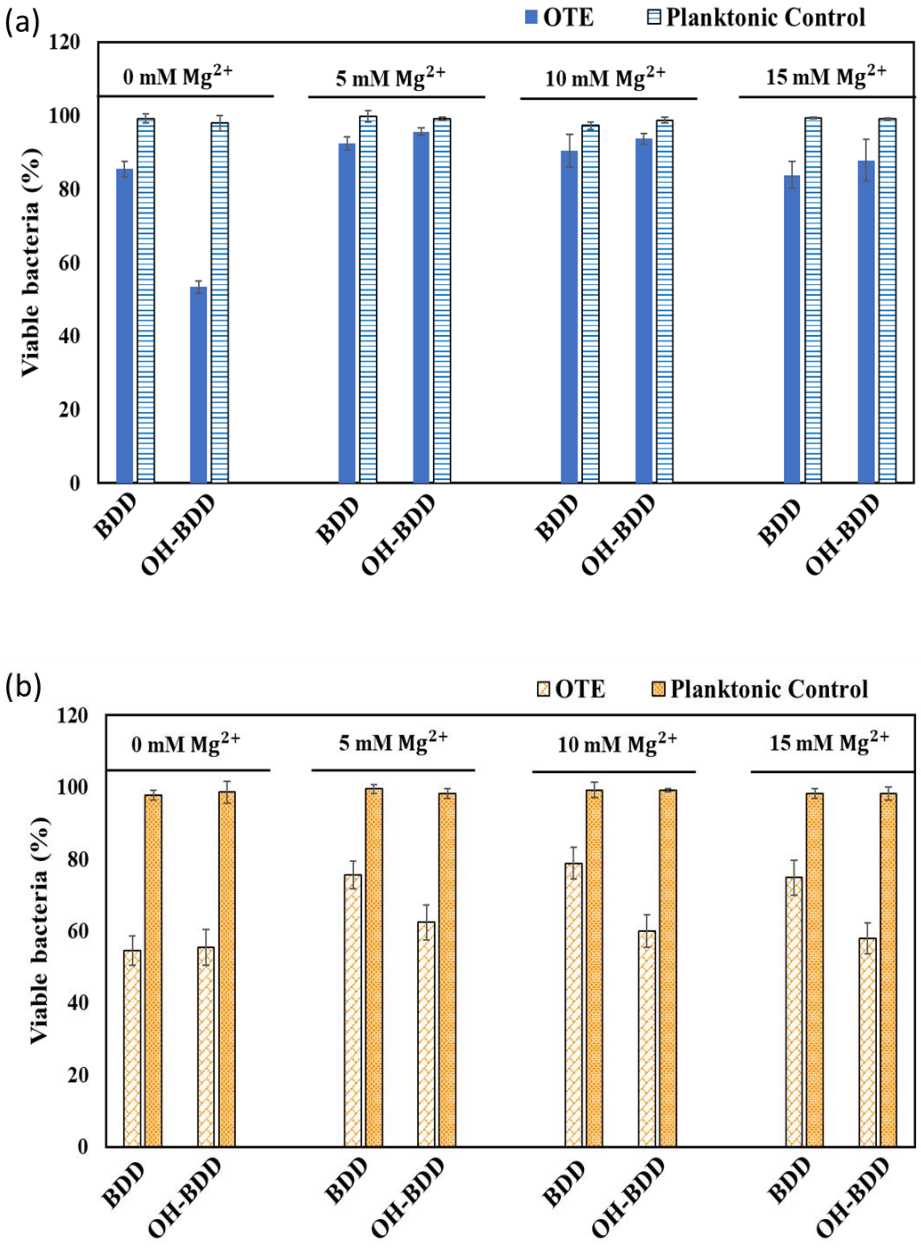

Figure 4- 8. Comparison of POA1 viable ratio on the different substrates with different concentration of $MgCl_2$ when the applied potential was (a) 0.2V and (b) -0.15V (n = 3).

To support the chelation hypothesis by the 2-hydroxyacetamide functional group of the OH-BDD/OTE, solution-phase experiments were conducted by adding different concentrations of either GA or EDTA to solutions containing bacteria. GA was used as a solution phase surrogate for the 2-hydroxyacetamide functional groups and EDTA was used for comparison purposes, as it is a well-known chelator [108, 135].

Bacteria numbers were controlled by OD_{600} readings before each experiment. As shown in **Figure 4-9**, in general, the percentage of viable bacteria decreased with increases in the concentration of chelator from 0 to 20 mM. The percentage of viable bacteria decreased from 77 ± 1.5% to 45 ± 2.0% when the concentration of GA was increased from 0 to 20 mM (**Figure 4-9a**), and the percentage of viable bacteria decreased from 75 ± 1.5% to 35 ± 2.3% over the same concentration range for EDTA (**Figure 4-9b**). The results indicated that GA behaved similarly to the well-known EDTA chelator and supports the hypothesis that the 2-hydroxyacetamide functional groups can act as a chelator of divalent cations.

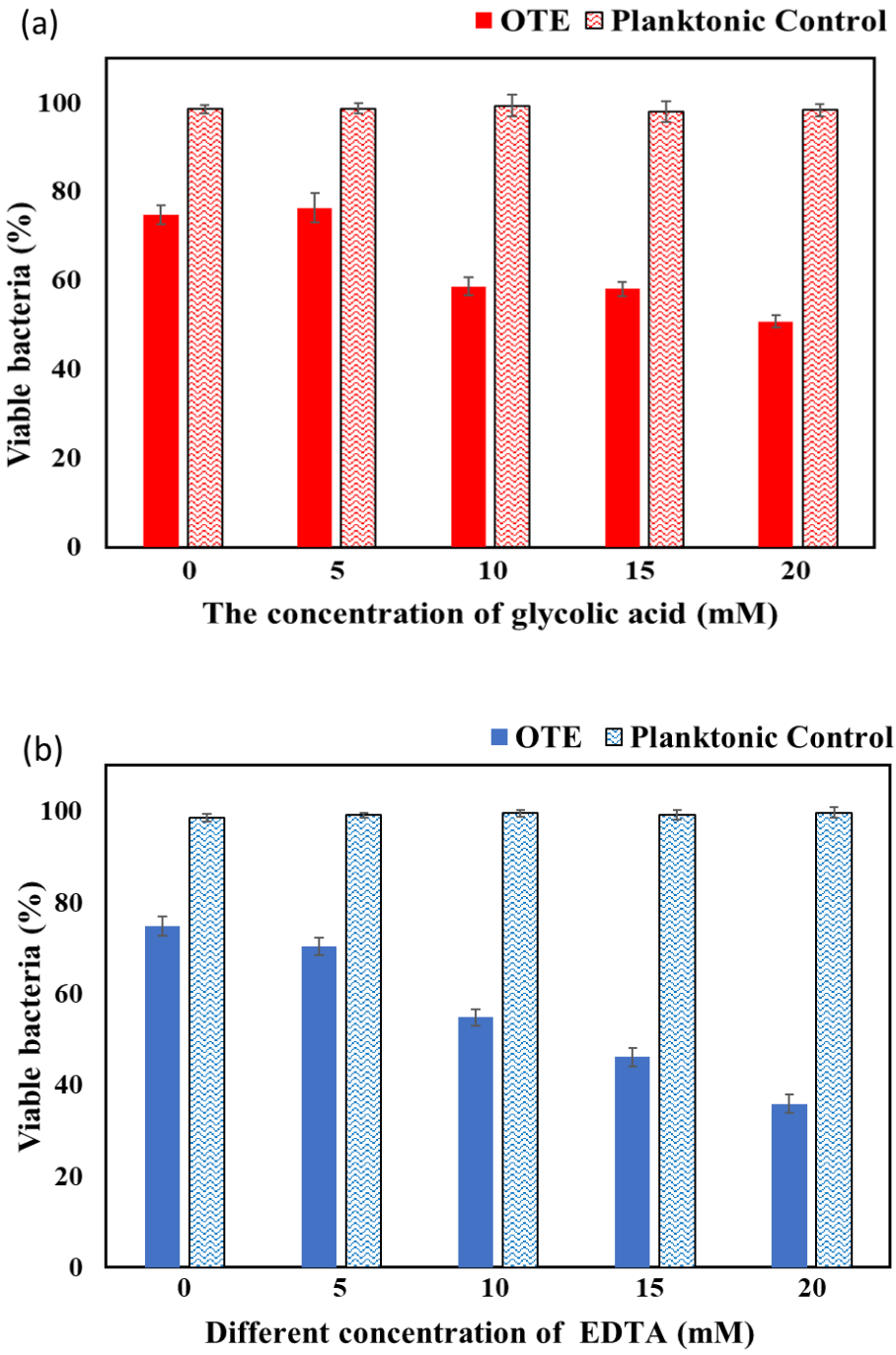

Figure 4- 9. *Comparison of the percentage of viable bacteria under different concentrations of (a) glycolic acid (GA) and (b) EDTA without applied potential (n = 3). All experiments used planktonic bacteria. Bacteria cells were exposed to different concentrations of EDTA and GA solutions for 90 minutes.*

For a deeper understanding of the effects that the solution phase chelators and divalent cations have on the bacteria surface charge, zeta potential measurements were made during the addition of EDTA or GA into solution in the presence of different Mg^{2+} concentrations (i.e., 0-30 mM). The POA1 bacteria surface charge was around -13 mV in the PBS electrolyte (pH = 7.5) in the absence of either chelators or added divalent cations (**Figure 4-10a**). However, the bacteria surface charge became more negative upon the addition of EDTA in the absence of Mg^{2+} and reached a value of -18 mV at a concentration of 30 mM EDTA (**Figure 4-10a**). The addition of Mg^{2+} (10, 20 and 30 mM) resulted in similar zeta potential versus EDTA concentration profiles, but they were shifted to higher surface charge values at a given EDTA concentration (**Figure 4-10b-d)**. The solution pH dropped from 7.5 to 5.5 while 30 mM EDTA was titrated into the system (data not shown). The zeta potential dropped to -22 mV once cell lysis occurred and a white precipitate was observed (data not shown).

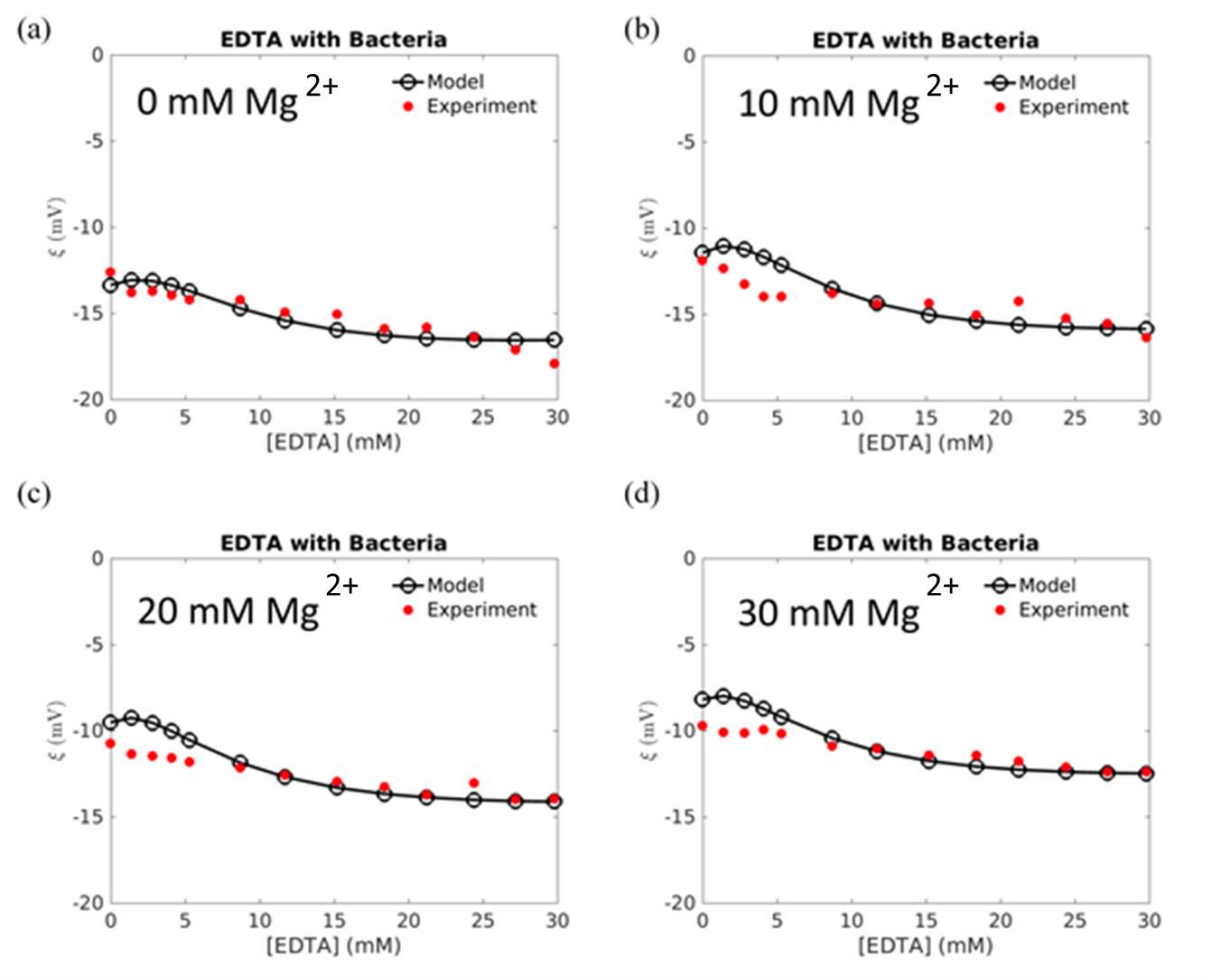

Figure 4- 10. Comparison of the percentage of viable bacteria under different concentrations of (a) glycolic acid (GA) and (b) EDTA without applied potential (n = 3). All experiments used planktonic bacteria. Bacteria cells were exposed to different concentrations of EDTA and GA solutions for 90 minutes.

The same experiments were conducted using GA as a chelator and similar experimental trends were observed (**Figure 4-11**). The POA1 bacteria zeta potential was around -12 mV in the PBS electrolyte (**Figure 4-11a**). The zeta potential decreased to -16 mV upon the progressive addition of GA in the absence of Mg^{2+}. Additional Mg^{2+} (10, 20 and 30 mM) increased the cell surface zeta potential as shown in **Figures 4-11b-d**. Similar to the EDTA experiments, the cell surface potentials decreased when GA was titrated into solution. Consequently, the solution pH

dropped from 7.5 to 3.5 while 30 mM GA was titrated into the system (data not shown). These results indicated that the bacteria surface charge increased with an increase in the concentration of divalent cations and that high enough concentrations of either EDTA or GA could chelate these ions, leading to decreases in surface charge and eventually cell lysis.

A mathematical model was used to interpret the experimental zeta potential measurements as a function of solution conditions. The dissociation constant (K_{a_i}), and the corresponding site number (N_{a_i}) of acidic functional groups for bacteria were determined from experimental titration data (**Appendix B, Figure B-5**). Previous titration studies demonstrated that bacteria have four primary acid/base functional groups including carboxylic, phosphate, amine, and hydroxyl groups [35, 139]. In our titration study (as shown in **Appendix B, Figure B-6**) the results demonstrated that POA1 has four pK_{a_i} values of 3.9, 7.4, 8.6 and 10.6 with their corresponding site numbers of 6.5, 5.4, 8.3 and 16.1 number/nm^2, as shown in the first row of **Table 4-2**. The mathematical model was also used to optimize N_{a_i} and pK_{a_i} values by fitting simulated zeta potentials to those from experimental measurements. Table 2 compares optimized POA1 N_{a_i} and pK_{a_i} values obtained from the model with those from the experimental measurements, where three of the four pK_{a_i} values were closely matched. The model also predicts Gibbs free energy of chelation and the corresponding N_{a_i} for EDTA and GA under various divalent cation concentrations. Overall, parameters predicted by the model are in the same order of magnitude and reasonable agreement with the experimental measurements (sum of squared residuals for dimensionless zeta potential, y, were 9.3x 10^{-3}, 2.7 x 10^{-2}, 2.3 x 10^{-2}, and 2.1 x 10^{-2}, for EDTA with 0, 10, 20, and 30 mM Mg^{2+}, respectively, and 1.1 x 10^{-2}, 1.7 x 10^{-2}, 1.5 x 10^{-2}, and 1.2 x 10^{-2} for GA with 0, 10, 20, and 30 mM Mg^{2+}, respectively). **Figure 4-10** and **4-11** compare zeta potentials obtained from experimental measurements and simulations for EDTA and GA, respectively. The reasonable agreement

between experimental data and the mathematical model supports the chelation mechanism as a viable explanation for PAO1 poration in our studies.

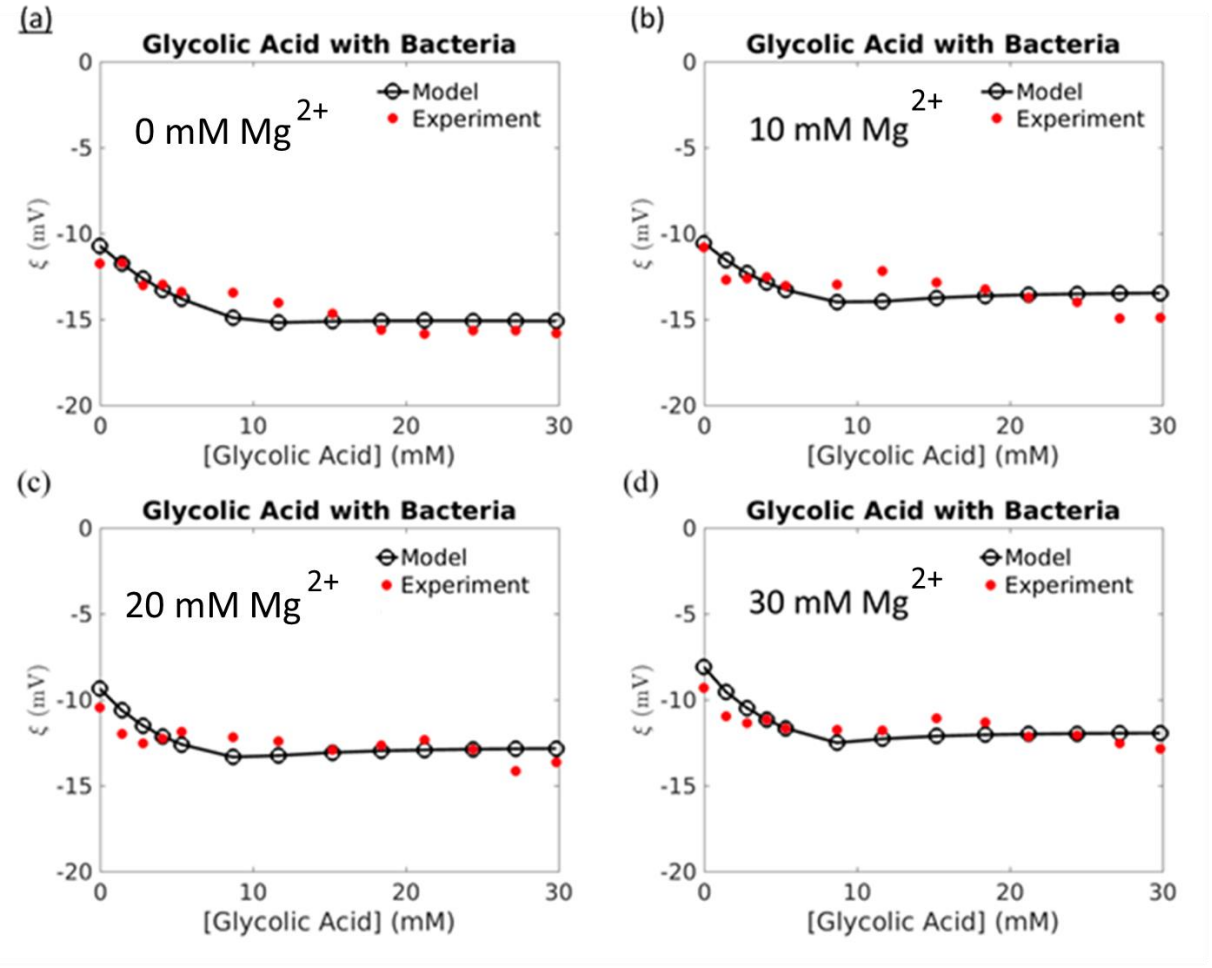

Figure 4- 11. Zeta potential of POA1 as function of different GA concentrations and (a) 0 mM, (b) 10 mM, (c) 20 mM and (d) 30 mM Mg^{2+} in the solution.

Table 4- 2. Deprotonation rate constants, their corresponding site numbers, and number of adsorption sites for chelation for EDTA and GA.[§]

	Deprotonation Rate Constant					**Site number (number/nm^2) ¶**					
Solution	pK_{a1}	pK_{a2}	pK_{a3}	pK_{a4}	K_M	N_{a1}	N_{a2}	N_{a3}	N_{a4}	N_d	ΔG^*
Experimental Solution Condition	3.9 (0.05)	7.4 (0.31)	8.6 (0.67)	10.6 (0.24)	-	6.5 (2.7)	5.4 (1.5)	8.3 (5.4)	16.1 (3.7)	-	-
EDTA, 0 mM Mg^{2+}	3.3	7.5	5.6	10.3	5.0	11.0	3.3	10.4	15.7	41.7	0.4
EDTA, 10 mM Mg^{2+}	3.3	7.5	5.2	10.3	5.0	11.0	16.3	10.4	15.9	62.0	0.4
EDTA, 20 mM Mg^{2+}	3.3	7.5	5.2	10.3	5.0	11.0	16.3	10.4	15.9	62.9	0.4
EDTA, 30 mM Mg^{2+}	3.3	7.5	5.2	10.3	5.0	11.0	16.3	10.4	15.9	57.8	0.4
GA, 0 mM Mg^{2+}	3.3	7.5	6.4	10.3	5.0	2.8	16.3	10.4	16.0	44.3	5.0
GA, 10 mM Mg^{2+}	3.3	7.5	6.2	10.3	5.0	8.9	16.3	10.4	16.0	50.8	5.0
GA, 20 mM Mg^{2+}	3.3	7.5	5.9	10.3	5.0	11.0	16.3	10.4	16.0	66.1	5.0
GA, 30 mM Mg^{2+}	3.3	7.5	5.2	10.3	5.0	11.0	16.3	10.4	16.0	76.4	5.0

[§]Standard deviation for experimental values is given in parentheses. [*]ΔG is the free energy in kJ/mol. [¶]Site volume number density was converted to surface number density assuming a uniform site distribution along a 50 nm fibril length [148].

4.5 Conclusion

The BDD electrode surface was successfully modified with 2-hydroxyacetamide functional groups. CV scans of $Fe(CN)_6^{3-/4-}$ and $Ru(NH_3)_6^{2+/3+}$ redox couples confirmed that the reactive surface area decreased by ~ 45% after electrode modification, likely due to a blockage of active sites by the functionalization process. XPS measurements confirmed the functional groups on the OTEs. The bacteria poration ratio on the OH-BDD/OTE surface was generally higher than on the BDD/OTE surface, which was attributed to chelation of divalent cations from the POA1 cell membrane leading to poration. Solution phase experiments with POA1, Mg^{2+}, and GA as a model chelator supported this chelation mechanism, which was corroborated with DFT simulations and a mathematical model based on the nonlinear Poisson-Boltzmann equation. Further work is needed to minimize the decrease of reactive surface area upon electrode modification and determine the interaction of bacteria cells on polarized electrode surfaces under

complex solution conditions and in the presence of various surface functional groups. BDD was used as a model electrode, due to its inert surface, chemical stability, and ability to fabricate as an OTE to facilitate the experimental work. However, in practice the BDD electrode may be replaced with other electrode materials, since the modification occurs through a self-assembly process via reaction with -OH groups on the electrode surface. Therefore, the modification is appropriate for carbon and metal oxide electrodes, and thus should have applicability on a range of electrode materials.

4.6 Acknowledgements

Funding for this work was provided by two National Science Foundation awards to B.P. Chaplin (CBET-1453081; CBET-1604776).

5. Chlorinated Byproduct Formation during the Electrochemical Advanced Oxidation Process at Magnéli Phase Ti_4O_7 Electrodes

5.1 Abstract

This research investigated chlorinated byproduct formation at Ti_4O_7 anodes. Resorcinol was used as a model organic compound representative of reactive phenolic groups in natural organic matter and industrial phenolic contaminants and was oxidized in the presence of NaCl (0—5 mM). Resorcinol mineralization was >79% in the presence and absence of NaCl at 3.1 V/SHE (residence time = 13 s). Results indicated that ~4.3% of the initial chloride was converted to inorganic byproducts (free Cl_2, ClO_2^-, ClO_3^-) in the absence of resorcinol and this value decreased to < 0.8% in the presence of resorcinol. Perchlorate formation rates from chlorate oxidation were 115—371 μmol m^{-2} h^{-1}, approximately two orders of magnitude lower than reported values for boron-doped diamond anodes. Liquid chromatography-mass spectroscopy detected two chlorinated organic products. A multi-chlorinated alcohol compound (C_3HCl_4OH) at 2.5 V/SHE and a mono-chlorinated phenolic compound ($C_8H_7O_4Cl$) at 3.1 V/SHE were proposed as possible structures. Density functional theory calculations estimated that the C_3HCl_4OH product was resistant to direct oxidation at 2.5 V/SHE and the $C_8H_7O_4Cl$ compound was likely a transient intermediate. Chlorinated byproducts should be carefully monitored during EAOPs and multi-barrier treatment approaches are likely necessary to prevent halogenated byproducts in the treated water.

5.2 Introduction

Electrochemical advanced oxidation processes (EAOPs) have recently been intensely researched as possible new modular technologies for drinking water treatment [158], industrial

wastewater treatment [159–161], and groundwater remediation [162, 163]. EAOPs rely on stable anode materials that primarily degrade contaminants through direct oxidation reactions at the anode surface and indirect oxidation through reactions with hydroxyl radicals ($OH^{\bullet}$) that form from the oxidation of water [38, 64]. Boron-doped diamond (BDD) electrodes are currently considered to be the state-of-the-art anode for EAOPs, because they generate high yields of $OH^{\bullet}$ and are anodically stable, corrosion resistant, and commercially available [39], [40]. However, the application of BDD electrodes for treatment of chloride-containing waters results in the formation of inorganic and organic chlorinated byproducts [38, 64–69, 164–166] which have documented health risks, such as bladder cancer and birth defects [71, 72].

The generation of inorganic chlorinated byproducts during EAOPs is initiated by the oxidation of chloride (Cl^-) at the anode surface. The general oxidation pathway is shown below:

$$Cl^- \rightarrow Cl^{\bullet} \rightarrow HOCl/OCl^- \rightarrow ClO_2^- \rightarrow ClO_2 \rightarrow ClO_3^- \rightarrow ClO_4^- \quad (5\text{-}1)$$

where chlorine is oxidized from an initial oxidation state of -1 in Cl^- to +7 in perchlorate (ClO_4^-). The electrochemical formation of chlorite (ClO_2^-), chlorate (ClO_3^-), and ClO_4^- has been reported in studies using BDD electrodes [64, 68–70]. The U.S. Environmental Protection Agency (EPA) has set a maximum contaminant level (MCL) for ClO_2^- in drinking water at 1.0 mg L^{-1} and proposed a non-enforceable MCL goal (MCLG) for ClO_4^- at 56 μg L^{-1} [167]. In addition, Massachusetts and California have set more stringent, enforceable drinking water standards for ClO_4^- of 2 μg L^{-1} and 6 μg L^{-1}, respectively [168, 169]. Currently, ClO_3^- is not regulated, but the EPA has set a health reference level (HRL) at 210 μg L^{-1} [63].

Organic chlorinated byproducts may also form during EAOPs through reactions between organic compounds and chlorine species shown in reaction (5-1), such as chlorine radical ($Cl^{\bullet}$),

hypochlorous acid/hypochlorite ($HOCl/OCl^-$), and chlorine dioxide (ClO_2). For example, the electrochemical treatment of saline waters using BDD anodes formed trihalomethanes (THMs), haloacetic acids (HAAs), haloacetonitriles, haloketones, 1,2-dichloroethane, and unidentified adsorbable organic chlorine compounds [65–67, 164, 165]. The EPA has set MCLs in drinking water for THMs and HAAs at a combined concentration of 80 $\mu g\ L^{-1}$ for four regulated THMs and 60 $\mu g\ L^{-1}$ for five regulated HAAs [36]. Several other halogenated industrial organic chemicals have also been regulated by the EPA at the $\mu g\ L^{-1}$ range. Due to the health concerns associated with both regulated and unregulated halogenated organic compounds, close scrutiny of unintended byproducts that form during EAOPs is necessary so that appropriate treatment trains can be developed for a given water treatment application.

Recent work has shown that porous Magnéli phase Ti_4O_7 electrodes are high surface area, stable anode materials [41, 42] that are capable of direct oxidation of contaminants [43] and formation of $OH^\bullet$ [42]. When operated in flow-through mode, Ti_4O_7 anodes achieve over an order of magnitude higher mass transport rates compared to traditional parallel plate electrochemical cells (e.g., BDD) [170]. The combination of enhanced mass transport and high specific surface area results in significant removal of various organic contaminants with high rate constants and low energy consumption, even when operated in a single-pass mode with low hydraulic residence times (~ 10 s) [43, 44, 170–174]. However, work has not yet been done to determine the potential for halogenated byproduct formation during their use in EAOPs.

Therefore, the aim of this study was to investigate both inorganic and organic chlorinated byproduct formation during EAOPs using a Magnéli phase Ti_4O_7 reactive electrochemical membrane (REM). Since phenolic compounds play a central role in the structure of natural organic matter (NOM) and many industrial contaminants present in natural waters [175–177] resorcinol

was used as a model organic compound, and it was oxidized in the presence of NaCl (1 and 5 mM) and as a function of electrode potential. Inorganic and organic byproduct formation was characterized using ion chromatography and liquid chromatography–mass spectrometry (LC-MS), respectively. The stability and probable fate of resorcinol and chlorinated byproducts were investigated using density functional theory (DFT) methods. This work is the critical first step in understanding halogenated byproduct formation on Ti_4O_7 electrodes.

5.3 Materials and Methods

5.3.1 Reagents

Sodium chloride (NaCl), sodium chlorite ($NaClO_2$), sodium chlorate ($NaClO_3$), potassium phosphate monobasic (KH_2PO_4) and HPLC grade methanol were purchased from Alfa Aesar (MA, USA). Sodium perchlorate ($NaClO_4$), sodium hypochlorite solution (NaOCl) with 10-15 wt/vol% available chlorine, and titanium dioxide (TiO_2) were purchased from Sigma-Aldrich (MO, USA). Resorcinol was purchased from MP Biomedical (OH, USA). Paraffin oil was purchased form EMD Millipore (USA). Sodium sulfite (Na_2SO_3) was purchased from Thermo Fisher (MA, USA). Chemical Oxygen Demand (COD) reagents were purchase from Hach (CO, USA). Solutions were made with deionized (DI) water (18.2 MΩ cm at 21°C). All chemicals were used as received.

5.3.2 REM Synthesis and Characterization

REMs were synthesized using a previously published method [178]. Briefly, 5g TiO_2 powder (particle diameter = 32 nm) was reduced to Ti_4O_7 in a tube furnace at 1050°C for 6 hours in the presence of 1 atm H_2 gas (flow rate = 252 cm^3 min^{-1}). The Ti_4O_7 powder (0.65 g) was mixed with 1.25 wt.% paraffin oil as a binder. The mixture was compressed in a 1.12 cm diameter die with a uniaxial pressure of 2.7 MPa. The thickness of the pellet was approximately 2 mm. Pellets

were placed in a tube furnace at 1050°C for 6 hours in the presence of 1 atm H_2 for sintering. The Magnéli phases present in the pellet were determined by XRD (Siemens D-5000) with Cu-Ka radiation (λ = 1.5418 Å) and diffraction peaks were identified according to the standard database [178].

5.3.*3* *Experimental Flow-Through Reactor Setup*

A schematic of the reactor setup is shown in **Appendix C** (**Figure C-1**). Experiments were performed in a flow-through reactor in single-pass mode with a standard three-electrode setup (**Appendix C**, **Figure C-1a**). The Ti_4O_7 REM was used as the working electrode (anode) with an exposed projected surface area of 0.5 cm^2. The current collector was Ti, and a 0.35 cm^2 BDD film on Nb (BDD/Nb) ring electrode was placed between the Ti and REM to prevent Ti corrosion in the presence of reactive chlorine species (**Appendix C, Figure C-1b**). The BDD/Nb electrode did not participate significantly in the reaction, as control experiments showed similar resorcinol oxidation when it was removed (data not shown). The counter electrode (cathode) was Ti and a 1 mm diameter leak-free Ag/AgCl was used as the reference electrode (Warner Instruments, LF-100, CT, USA) (**Appendix C, Figure C-1b)**. Permeate flux (J = 240 L m^{-2} hr^{-1} (LMH)) was controlled and adjusted using a digital gear micropump (Cole-Parmer, IL, USA). Applied potentials and currents were controlled and measured by a Gamry Reference 600 potentiostat/galvanostat (PA, USA). All potentials were corrected for potential drop in the solution (iR_s) and reported versus the standard hydrogen electrode (/SHE).

5.3.4 *Electrochemical Oxidation Experiments*

All oxidation experiments were conducted in the flow-through reactor at 22±1 °C, pH = 6.7, and a solution conductivity of 283 μS cm^{-1} using a KH_2PO_4 background electrolyte. The

solution conductivity value was chosen to mimic that of typical natural waters [179] and was measured using a conductivity probe (PC2700, Oakton, Cole-Parmer, IL, USA). Control oxidation experiments were performed with either 1 mM resorcinol or NaCl (1 and 5 mM), to determine a baseline for resorcinol oxidation and inorganic chlorinated byproduct formation. The following potentials were applied during electrochemical oxidation experiments: open circuit potential (OCP = 0.11 V/SHE), 0.99 ± 0.09, 1.56 ± 0.03, 2.07 ± 0.04, 2.5 ± 0.04 and 3.1 ± 0.03 V/SHE. Two solution conditions were used to study chlorinated byproduct formation: (1) 1 mM NaCl and 1 mM resorcinol; (2) 5 mM NaCl and 1 mM resorcinol. All experiments were performed in duplicate, and errors reported represent 95% confidence intervals on average values. The 1 mM concentration of resorcinol was chosen to ensure transformation product detection and the 1—5 mM NaCl concentrations were chosen to bracket the Cl^- concentrations found in typical natural waters [180].

Separate experiments were conducted to measure the kinetics of ClO_4^- formation from a 1 mM $NaClO_3$ and 10 mM KH_2PO_4 solution under OCP and 3.0 V/SHE with flow rates of 240 to 1200 LMH. In order to compare with the electrochemical system, batch control experiments were also conducted in a beaker containing 1 mM NaOCl, 1 mM resorcinol, and the background KH_2PO_4 electrolyte under constant mixing.

5.3.5 Analytical Methods

The permeate samples were split during collection. One part was immediately quenched by Na_2SO_3 addition and used for further analyses; the other part was used for free chlorine measurements. Concentrations of Cl^-, ClO_2^-, ClO_3^-, and ClO_4^- were determined by ion chromatography (Dionex ICS-2100; Dionex Ion Pac AS16 column; KOH eluent; 0.75 mL min^{-1} flow rate) with method detection limits of 10 nM for ClO_2^-, ClO_3^-, and ClO_4^- and 5 nM for Cl^-. Free chlorine (as Cl_2) concentrations were determined by Hach method 8021 (USEPA N,N-

diethyl-p-phenylenedi-amine (DPD) method) [142] according to the manufacturer's protocol. The Cl^- concentration was calculated by subtracting the measured free chlorine concentration from the IC measured Cl^- concentration, where the later was quenched with Na_2SO_3. The total moles of Cl were calculated using equation (5-2).

$$\text{Total mole of Cl} = 2\times\text{Free Chlorine } (Cl_2) + Cl^- + ClO_2^- + ClO_3^- + ClO_4^- \quad (5\text{-}2)$$

Resorcinol concentrations were determined using a Shimadzu UFLC XR HPLC with a Phenomenex Kinetex 5 µm C18 column (5µm, 100 Å, 250 × 4.6 mm) and a photodiode array detector (PDA) (Nexera X2, Shimadzu). The mobile phase was 75:25 (%, v/v) mixture of methanol and DI water with a flow rate of 1.0 mL min^{-1}. The PDA detector was set to 254 nm for resorcinol analysis [142, 181, 182]. Chemical oxygen demand (COD) measurements were used to estimate resorcinol mineralization. according to the manufacturer's protocol [183].

Select samples were analyzed by negative mode electrospray ionization liquid chromatography mass spectrometry (LC-MS; Agilent 1260 HPLC coupled to an Agilent 6460 triple-quad MS). Elutions were achieved using an Agilent Poroshell 120 EC-C18 column with 0.1% formic acid (10% acetonitrile, v/v) and acetonitrile as the aqueous and mobile phases, respectively, at a flow rate of 0.25 mL/min. The mass-to-charge ratios (*m/z*) of chlorinated compounds were identified from a full MS2 scan from 25 – 500 *m/z* based on the isotopic signature of chlorine. All *m/z* values measured by LC-MS were converted to Daltons (Da) by adding the mass of one proton after verifying that the ions were singly charged. The differences in the masses of proposed structures and the measured masses may be due to slight differences in the Cl^{35}:Cl^{37} isotope ratios but are within the error of the LC-MS. For all proposed Cl-containing compounds it was assumed that Cl had a standard molar mass of 35.45 Da.

5.3.6 Quantum Mechanical Simulations

DFT simulations were performed using Gaussian 16 software [145]. Unrestricted spin, all-electron calculations were performed using the 6-31G++(d) basis set for frequency and geometry optimization, and the 6-311G++(3df,2p) basis set for energy calculations. The M06-2X hybrid meta exchange-correlation functionals was used [184], and implicit water solvation was simulated using the SMD model [185]. Individual explicit water molecules were incorporated into simulations where appropriate, in order to simulate important hydrogen bonding interactions.

Direct electron transfer reactions were modeled using Marcus theory, according to methods described previously [173, 186]. The E^0 values for a given direct electron transfer reaction were calculated by the following equation:

$$E^0 = -\frac{\Delta_r G^0}{nF} - E^0_{abs}(SHE) \tag{5-3}$$

where $\Delta_r G^0$ is the standard free energy for the reduction reaction, F is the Faraday constant, n is the number of electrons transferred, and $E^0_{abs}(SHE)$ is the absolute standard reduction potential of the SHE ($E^0_{abs}(SHE)$ = 4.28 eV) [187, 188]. The potential dependent Gibbs free energy of activation ($\Delta G^{\ddagger}$) for direct electron transfer oxidation reactions were calculated using Marcus theory according to the following equation [189]:

$$\Delta G^{\ddagger} = \frac{\lambda_f}{4}\left[1 - \frac{96.5(E-E^0}{\lambda_f}\right]^2 \tag{5-4}$$

where E is the applied electrode potential and λ_f is the total reorganization energy of the forward oxidation reaction. The effect of the solvent on λ_f was not considered as previous research showed negligible solvent effects in polar solvents [190].

5.4 Results and Discussion

5.4.1 Resorcinol Oxidation Experiments

The Ti_4O_7 Magnéli phase reactive electrochemical membranes (REMs) used in this study were thoroughly characterized in prior work [178]. The conductivity of the REM was 765 S m^{-1}, and the XRD pattern contained the characteristic peak at 20.8° and other peaks the matched the Ti_4O_7 standard data (**Figure 5-1a**). A schematic showing the possible electrochemical reaction pathways for resorcinol and chloride oxidation are shown in **Appendix C**, **Figure C-2**. Control oxidation experiments were conducted containing only 1 mM resorcinol (flux = 240 LMH; KH_2PO_4 electrolyte; solution conductivity = 283 μS cm^{-1}; pH = 6.7). As shown in **Figure 5-1b,** under OCP conditions (0.11 V/SHE), resorcinol removal was not observed, which indicated that it did not significantly adsorb on the REM. Measurable resorcinol oxidation began at potentials > 1.0 V/SHE, and average normalized permeate resorcinol concentrations (C_p/C_f) for duplicate experiments were 0.80 ± 0.01, 0.52 ± 0.001, 0.29 ± 0.01, and 0.12 ± 0.01 at anodic potentials of 1.6, 2.1, 2.5, and 3.1 V/SHE, respectively. The OCP, 2.5, and 3.1 V/SHE were used for subsequent resorcinol electrochemical oxidation experiments, which is a realistic potential range for which electrochemical oxidation would be used in a treatment scenario.

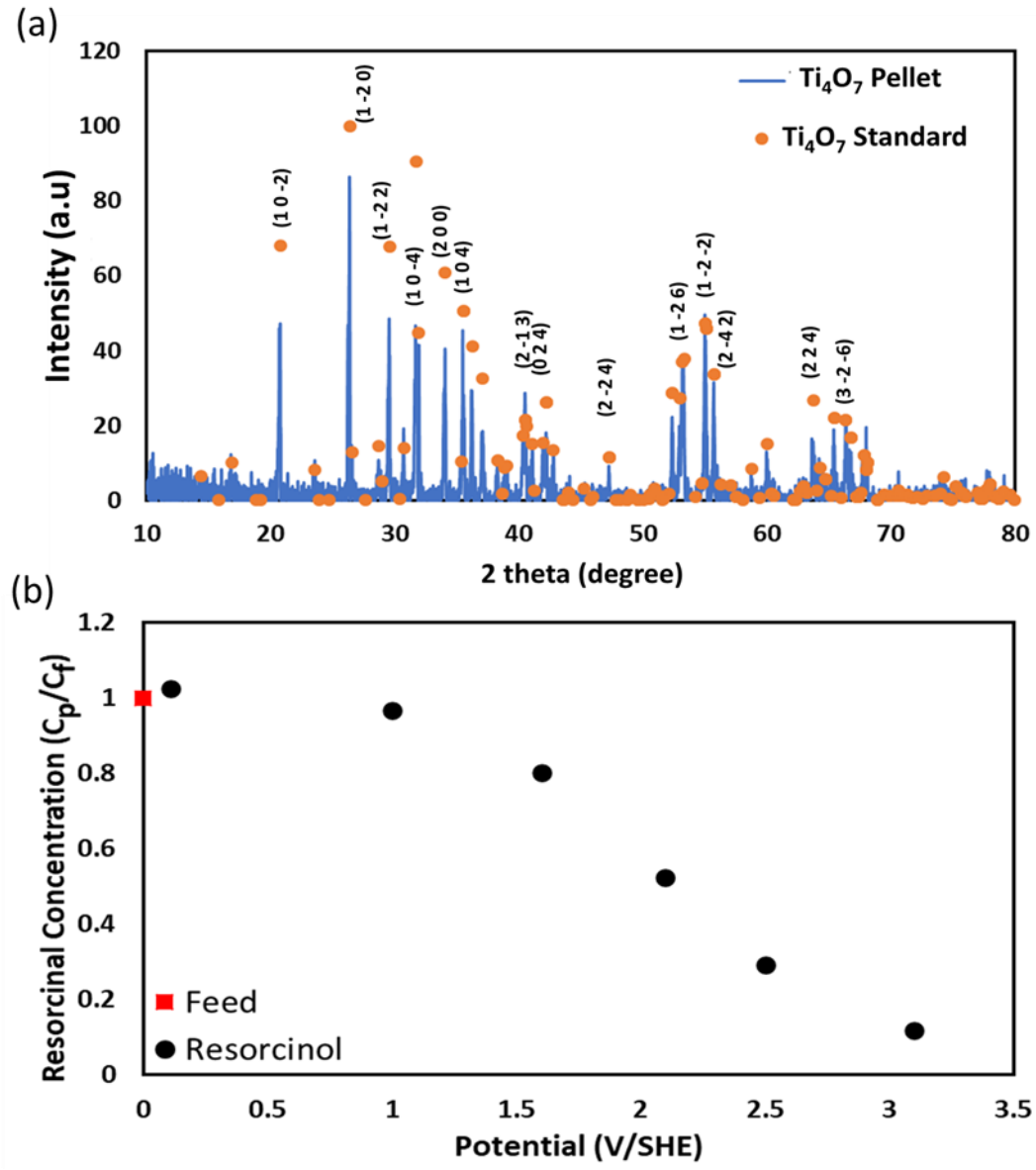

Figure 5- 1. **(a)** XRD analysis of Ti_4O_7 pellet (blue line) and the standard diffraction data of Ti_4O_7 (JCPDS. No. 50-0787) (orange dot). Separate control experiments of (b) Normalized resorcinol concentration profiles (C_p/C_f) in the feed (red square) and permeate solution (black dots) after oxidation process with a flux 240 LMH and retention time 13s. Error bars are contained within the data points.

To investigate chlorinated byproduct formation, NaCl concentrations of 1 and 5 mM were added to 1 mM resorcinol. Resorcinol permeate concentration profiles indicated that the addition of NaCl to solution does not have a pronounced effect on resorcinol removal (**Appendix C, Figure**

C-3). For example, the average resorcinol C_p/C_f values for duplicate 1 mM resorcinol experiments without NaCl were 0.29 ± 0.01 and 0.12 ± 0.01 at 2.5 and 3.1 V/SHE, respectively. These values increased to 0.38 ± 0.02 and 0.20 ± 0.01 for the 1 mM resorcinol/1 mM NaCl solutions and were 0.35 ± 0.03 and 0.14 ± 0.02 for the 1 mM resorcinol/5 mM NaCl solutions at applied potentials of 2.5 and 3.1 V/SHE, respectively. In addition, the C_p/C_f values for COD were used to estimate the extent of resorcinol mineralization (**Appendix C**, **Figure C-3**). Estimates of mineralization at 2.5 V/SHE were 82 ± 11%, 110 ± 13%, and 89 ± 18%, and estimates at 3.1 V/SHE were 84 ± 7%, 86 ± 9%, and 79 ± 6% at 0, 1, and 5 mM NaCl concentrations, respectively. Results do not show clear trends for resorcinol mineralization with respect to either potential or NaCl concentration. However, resorcinol mineralization was >79% in a single pass through the REM in all experiments, and the overall oxidation half-reaction is shown in reaction 5-5.

$$C_6H_6O_2 + 10H_2O \rightarrow 6CO_2 + 26H^+ + 26e^- \quad (5\text{-}5)$$

5.4.2 Electrochemical Byproduct Formation

The formation of inorganic chlorinated byproducts was investigated in two sets of experiments: 1) NaCl-only controls with 1 and 5 mM NaCl, and 2) 1 mM resorcinol containing either 1 or 5 mM NaCl. Results from oxidation of a 1 mM NaCl solution are shown in **Figure 5-2a** and are reported as a percentage of the feed Cl^- concentration at log-scale. Only 6.0 ± 4.0% to 7.0 ± 2.0% of Cl^- was oxidized at anodic potentials between 1.0 to 3.1 V/SHE, indicating slow reaction kinetics for Cl^- at the Ti_4O_7 surface compared to resorcinol oxidation. Inorganic chlorinated compounds were limited to free Cl_2 (i.e., HOCl + OCl^-) at concentrations between 5.1 to 21 μM (1.0 to 4.3% of feed Cl^-), and approximately 0.7 μM of ClO_2^- (0.070% of feed Cl^-) was detected at an anodic potential of 3.1 V/SHE (**Figure 5-2a**). Neither ClO_3^- nor ClO_4^- were detected

(< 10 nM) during the oxidation of the 1 mM NaCl solution. The oxidation products from a 5 mM NaCl solution are shown in **Figure 5-2c**. Chloride oxidation was between 3.0 ± 4.0% at 1.0 V/SHE and increased to 6.0 ± 2.0% at 3.1 V/SHE. Oxidized inorganic chlorinated species included free Cl_2 (6.5 to 110 μM; 0.26 to 4.4% of feed Cl^-), ClO_2^- (0.1 to 2.5 μM; 0.0020 to 0.050% of feed Cl^-), ClO_3^- (6.0 to 8.0 μM; 0.12 to 0.16% of feed Cl^-), and low concentrations of ClO_4^- of 0.3 μM (1.5 μg L^{-1}; 0.0060% of feed Cl^-) at 1.6 V/SHE and 3.1 V/SHE (**Figure 5-2c**). The ClO_4^- concentrations were lower than the EPA's proposed MCLG for perchlorate (56 μg L^{-1}) and ClO_3^- concentrations were close to the EPA's HRL. The highest measured conversion of Cl^- to inorganic byproducts in the 1 mM NaCl solution was 4.3% at 2.5 V/SHE and in the 5 mM NaCl solution was 4.5% at 2.5 V/SHE. The total measured inorganic chlorinated byproducts were not significantly different from the total Cl^- conversion.

The inorganic chlorinated byproducts that formed during the oxidation of resorcinol in NaCl solutions were similar to the NaCl-only control experiments, and Cl^- oxidation was 10 ± 1% at both anodic potentials of 2.5 and 3.1 V/SHE. Permeate solutions contained low concentrations of free Cl_2 (1.1 and 4.0 μM; 0.22 and 0.80% of feed Cl^-) in the 1 mM NaCl/resorcinol solution (**Figure 5-2b**) and free Cl_2 (5.0 and 7.0 μM; 0.20 and 0.28% of feed Cl^-), ClO_2^- (2.0 μM; 0.040% of feed Cl^-), and ClO_3^- (3.5 and 3.0 μM; 0.070 and 0.060% of feed Cl^-) in the 5 mM NaCl/1 mM resorcinol solution (**Figure 5-2d**). Perchlorate was detected at a low concentration (1.5 μM; 0.030% of feed Cl^-) in the 5 mM NaCl control but was not detected in the 5 mM NaCl/1 mM resorcinol experiments, similar to prior work that concluded that ClO_4^- formation is lower in chloride-containing solutions that contain organic compounds [191]. In fact, all inorganic chlorinated products were lower in the presence of resorcinol (comparing **Figures 5-2a** to **5-2b** and **Figure 5-2c** to **5-2d**) due to the competition for reactive sites and available oxidants and reactions between

organics and chlorinated inorganic oxidants. The highest measured conversion of Cl^- to inorganic byproducts in the 1 mM NaCl/1 mM resorcinol solution was 0.8% at 3.1 V/SHE and in the 5 mM NaCl/1 mM resorcinol solution was 0.3% at 2.5 V/SHE. The total measured inorganic chlorinated byproducts were much lower than the total Cl^- conversion, indicating that chlorinated organic byproducts likely formed.

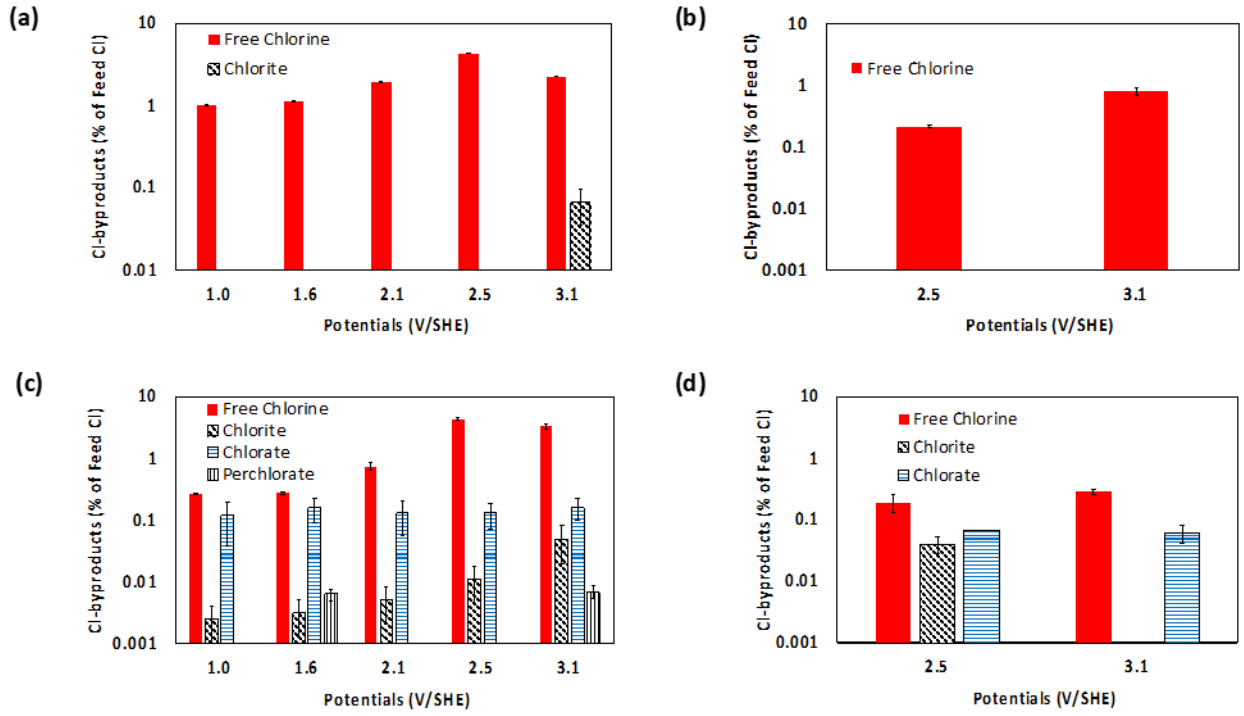

Figure 5- 2. Inorganic chlorinated byproducts detected during oxidation experiments: (a) 1 mM NaCl; (b) 1 mM NaCl and 1 mM resorcinol; (c) 5 mM NaCl; and (d) 5 mM NaCl and 1 mM resorcinol. For all experiments were operated with KH_2PO_4 background electrolyte, solution conductivity 283 µS/cm, solution pH 6.7 and J = 240 LMH.

Since ClO_4^- is a terminal oxidation product of Cl^-, it has potential to accumulate in solution under conditions of extended electrolysis (e.g., batch mode oxidation). Therefore, separate experiments were conducted to investigate ClO_4^- formation with a 1 mM $NaClO_3$ feed solution at an anodic potential of 3.0 V/SHE and as a function of flow rate (**Appendix C, Figure C-4)**. Results from these experiments yielded a first order rate constant of 0.04 s^{-1} for ClO_4^- formation and

permeate ClO_4^- concentrations ranged between 31 to 48 μg L^{-1}, for hydraulic residence times between 2.6 to 13 s, respectively (**Appendix C, Figure C-4a**). These concentrations yield projected surface area normalized rates between 115 and 371 μmol m^{-2} h^{-1} (**Appendix C, Figure C-4b**), which are approximately three orders of magnitude lower if normalized by the total REM surface area [178]. These experiments represent the worst-case scenario for ClO_4^- formation, as they were conducted with high ClO_3^- concentration (1 mM) and in the absence of organic compounds. Under similar reaction conditions (i.e, 1 mM $NaClO_3$, anode potential of 2.6 to 2.7 V/SHE) the formation of ClO_4^- from ClO_3^- on BDD electrodes was measured at rates between 28,000 to 45,000 μmol m^{-2} h^{-1} [69], which are over two orders of magnitude higher than our reported rates. Furthermore, the ClO_4^- concentrations in our experiments were always lower than the EPA's MCLG of 56 μg L^{-1} [167]. These results show the low production rate of ClO_4^- on the Ti_4O_7 REM anodes compared to BDD.

During the oxidation of resorcinol to CO_2, it was assumed that various radicals formed and reacted with each other to form a diverse set of products. To characterize the primary stable products during this process, permeate solutions from resorcinol oxidation were analyzed by LC-MS (**Figure 5-3**). The raw LC-MS data is provided in the SI and isotopic patterns were used to identify chlorinated products (**Appendix C, Figures C-5 and C-6**). Resorcinol oxidation in NaCl-free solutions at potentials of 2.5 and 3.1 V/SHE resulted in non-chlorinated products with observed masses of 110.1, 116, 154.1, 187.2, and 218 Da (**Figure 5-3**). The 110.1 Da product had the same mass as resorcinol but a different retention time, indicating it was an oxidation product. Under OCP conditions, products were not observed in agreement with the lack of resorcinol transformation (**Figure 5-1b**). Products were not detected with a mass less than resorcinol (110.1 Da), indicating that higher molecular weight compounds formed from the coupling of radical

species and addition of $OH^{\bullet}$ during the reaction. Resorcinol oxidation in the presence of 1.0 and 5.0 mM NaCl caused a slight decrease in the peak areas of the non-chlorinated oxidation products relative to the NaCl-free experiments at both 2.5 and 3.1 V/SHE (**Figure 5-3**), indicating some competition at the electrode surface between organic species and Cl^- oxidation.

The addition of 1 mM and 5 mM NaCl to solution resulted in the formation of organic chlorinated byproducts (**Figure 5-3**). The chlorinated organic byproducts consisted of a chlorinated compound with four Cl atoms and a mass of 196.7 Da detected at 2.5 V/SHE and a mono-chlorinated compound with a mass of 202.1 Da detected at 3.1 V/SHE (**Figure 5-3 and Appendix C, Figure C-6**). The chlorinated organic byproduct peak areas increased by an order of magnitude by increasing the NaCl concentration from 1 to 5 mM at both 2.5 V/SHE (**Figure 5-3a**) and 3.1 V/SHE (**Figure 5-3b**). Other chlorinated organic compounds were not detected, suggesting that the chlorinated compounds with masses of 196.7 and 202.1 Da were fairly resistant to further oxidation, oxidized to nonpolar chlorinated organic compounds that were not detected by LC-MS, and/or mineralized to CO_2, H_2O, and inorganic chlorine species (ClO_x^-, x = 1 to 4).

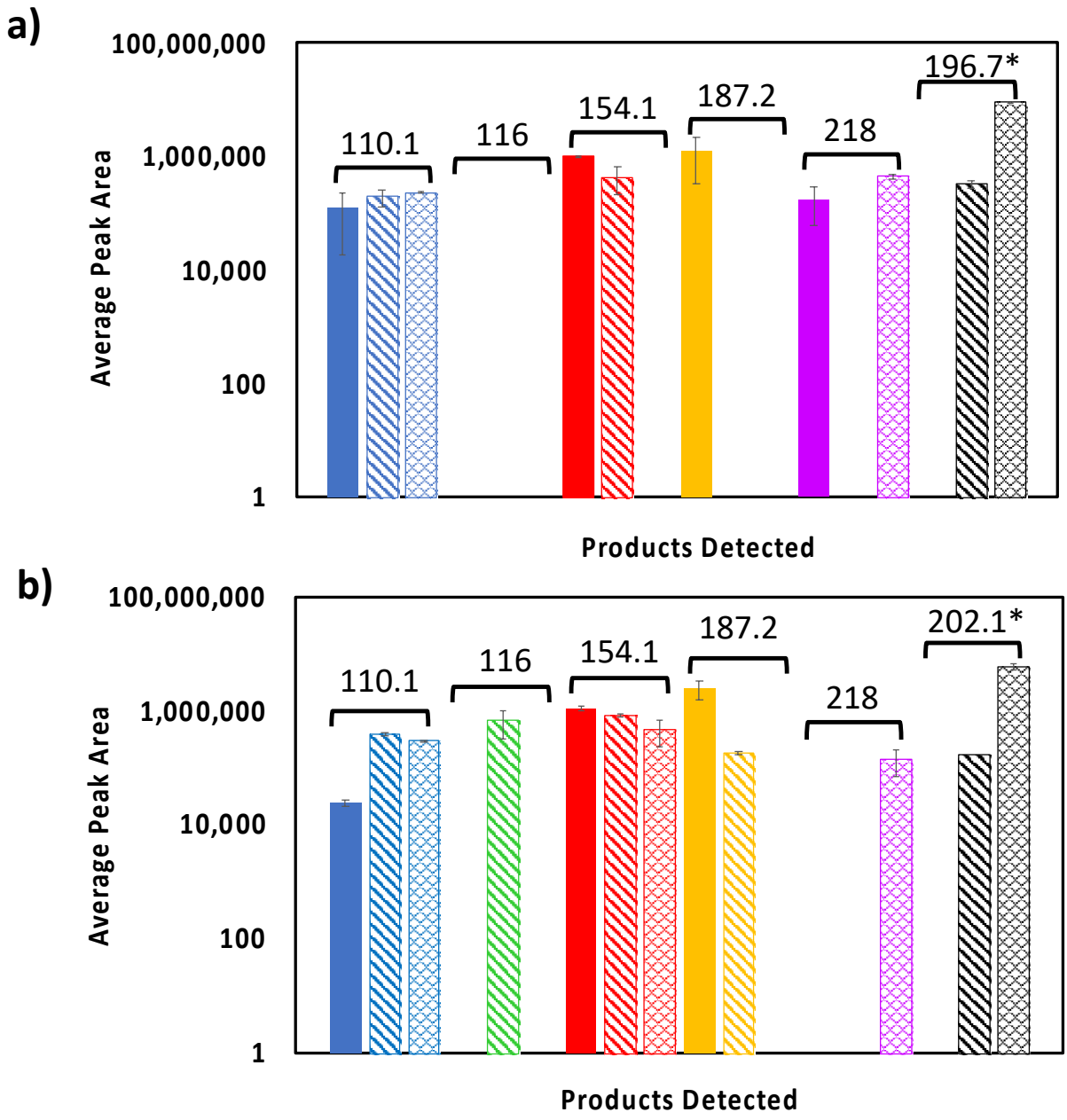

Figure 5- 3. Organic and chlorinated byproducts formation in the permeate solution during oxidation process with applied potential (a) 2.5 V/SHE and (b) 3.1 V/SHE. Mass of organic byproducts were determined by LC-MS. (Solid = 0 mM NaCl; striped = 1 mM NaCl; hatched = 5 mM NaCl; and * = chlorinated product). Table C-1 in the Appendix C contains a list of the masses of proposed structures.

5.4.3 Free Chlorine Generated Byproducts

Additional control experiments were conducted to determine if the organic chlorinated byproducts that were observed during electrochemical oxidation of resorcinol were a result of reaction with free Cl_2. Therefore, a batch experiment containing equimolar concentrations of 1 mM NaOCl and 1 mM resorcinol in the KH_2PO_4 background electrolyte with the same solution composition as electrochemical experiments was conducted. The 1:1 molar ratio of NaOCl:resorcinol was used to better reflect the anticipated solution conditions near the anode surface, where free Cl_2 concentrations would be higher and resorcinol concentrations lower compared to the bulk solution. The formation of organic chlorinated byproducts was studied using LC-MS analysis, and results are shown in the **Appendix C** (**Figure C-7** and **C-8)** for reaction times of 10 and 40 minutes. The total reaction time between free Cl_2 and resorcinol for electrochemical experiments was approximately 6 minutes, which corresponded to the time the fluid entered the REM reactor until it was quenched with $NaSO_3$. Organic chlorinated byproducts with masses of 84, 150 and 178 Da were detected in the 1 mM NaOCl/1 mM resorcinol solution (**Appendix C, Figure C-7** and **C-8**). Structures with masses of 82.5, 150.5 and 178.9 Da were proposed as possible products for the reaction between resorcinol and $HOCl/OCl^-$ (**Appendix C, Figure C-9 and Table C-1)** and were based on results from the literature.[55-65] Products include a chlorinated phenolic compound (mass = 178.9 Da) and chlorinated aliphatic compounds (masses = 150.5 and 82.5 Da). The products for direct reaction between resorcinol and $HOCl/OCl^-$ were distinctly different from those for electrochemical oxidation experiments (**Figure 5-3**), indicating that oxidation of resorcinol by $HOCl/OCl^-$ was minor in electrochemical experiments.

5.4.4 Mechanism

DFT modeling was used to interpret the experimental data and to gain insights into probable reaction pathways for the electrochemical oxidation of resorcinol and subsequent chlorinated byproduct formation. The potential dependent $\Delta G^{\ddagger}$ values for the oxidation of resorcinol (R) via direct electron transfer (DET) (reaction 5-6) were calculated using Marcus Theory (equation 5-6):

$$R \rightarrow R^{\bullet+} + e^{-} \quad (5\text{-}6)$$

The results are shown in **Figure 5-4a**, and the structure of the optimized R/ $R^{\bullet+}$ structures are shown in **Appendix C** (**Figure C-10**). Modeling determined E^{o} = 1.50 V/SHE and λ_f = 26 kJ mol^{-1}. **Figure 5-4a** shows that $\Delta G^{\ddagger}$ = 54 kJ mol^{-1} at 1.0 V/SHE and $\Delta G^{\ddagger}$ = 3.9 kJ mol^{-1} at 1.56 V/SHE. These results are consistent with experimental results where resorcinol degradation began to increase in this potential range (**Figure 5-1b**), suggesting the DET mechanism was a primary mechanism for resorcinol oxidation at anodic potentials that were too low for $OH^{\bullet}$ formation (i.e., < 2.5 V/SHE) [117]. At higher potentials, where $OH^{\bullet}$ formation increases, reaction between $OH^{\bullet}$ and resorcinol will occur with a diffusion-limited rate constant ($k_{OH^{\bullet},Res.}$ = 1.2 x 10^{10} M^{-1} s^{-1}; pH = 9) [200], indicating that it could also be a contributing mechanism for resorcinol oxidation at anodic potentials > 2.5 V/SHE. The combination of $R^{\bullet+}$ and $OH^{\bullet}$ formation and the various radical oxidation and dimerization reactions that are possible can lead to a wide range of products. The masses detected by LC-MS in the NaCl-free solutions (110.1, 116.1, 154.1, 187.2, and 218 Da) can be explained by three general pathways (**Scheme 5-1**): Pathway 1) DET reactions that lead to dimerization of $R^{\bullet}$; Pathway 2) $OH^{\bullet}$ attack of R to form ring opening products; and Pathway 3) C fragment addition to R to form substituted phenolic compounds [86, 204, 205].

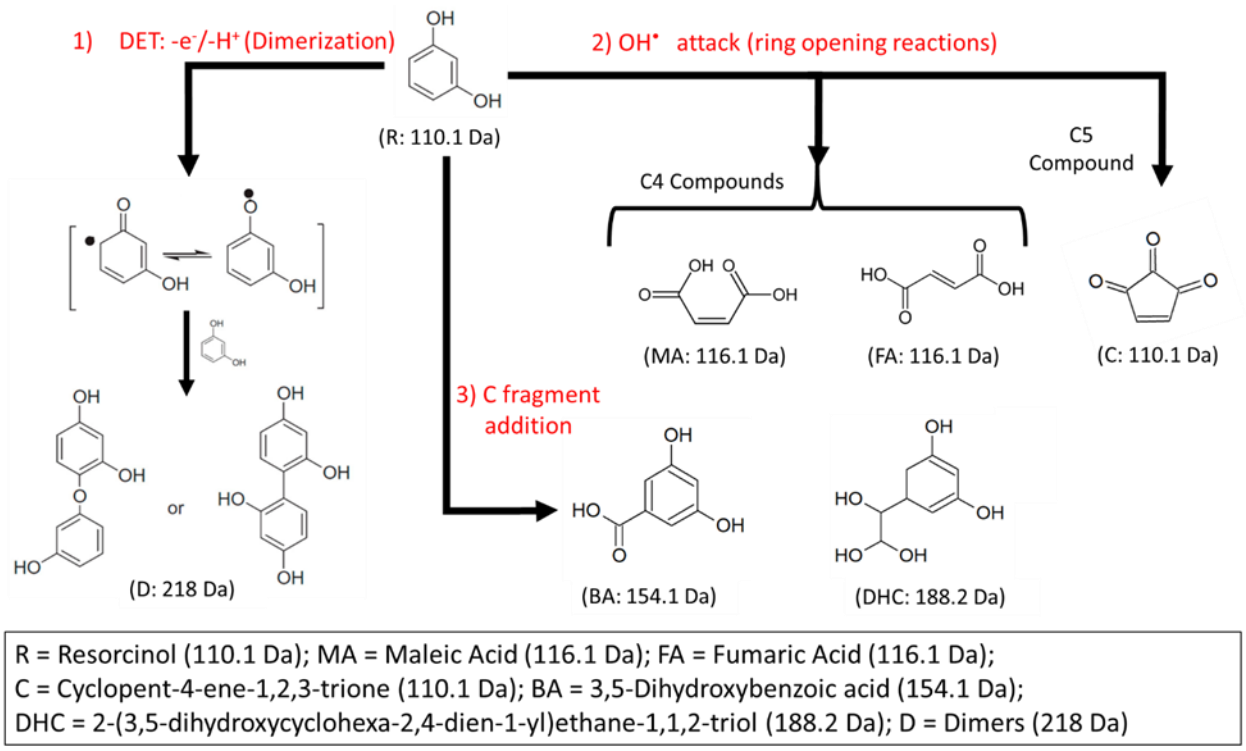

Scheme 5- 1. Suggested mechanism of resorcinol electrooxidation in NaCl-free solutions. Masses of compounds are for proposed structures and may differ slightly from masses detected by LC-MS (see Appendix C, Table C-1).

Pathway 1 is proposed to form R dimerization products with a mass of 218 Da. The 218 Da product was detected in the NaCl-free solution at 2.5 V/SHE but not at 3.1 V/SHE (**Figure 5-3**), which was attributed to a higher yield of $OH^{\bullet}$ at 3.1 V/SHE that would both break the phenolic ring of R and oxidize any dimerization products that formed. The formation of the 218 Da product was also sensitive to the NaCl concentration. For example, it was not detected in the 1 mM NaCl solutions but was detected at 5 mM NaCl at both potentials (**Figure 5-3**). The exact mechanisms responsible for these observations are unclear but are likely a result of reactions between $OH^{\bullet}$ and chlorine species, as well as competition for DET sites at the electrode surface between R, Cl^{-}, and reaction intermediates.

Pathway 2 leads to ring opening reactions with proposed C4 products of maleic acid (MA) and fumaric acid (FA), both with mass of 116.1 Da, and the C5 product of cyclopent-4-ene-1,2,3-trione (C), with a mass of 110.1 Da. Both MA and FA have been detected in prior studies of electrochemical oxidation of phenolic compounds [64, 202]. The 116 Da product was only detected at 3.1 V/SHE and in the presence of 1 mM NaCl (**Figure 5-3**), which indicates that this product was generally a fast reacting intermediate but its rate of degradation was affected by competitive reactions from Cl^-.

Pathway 3 involves the reaction between $R/R^{\bullet+}$ and C fragments that form during the electrochemical oxidation process, forming proposed products of 3,5-dihydroxybenzoic acid (BA), with a mass of 154.1 Da, and 2-(3,5-dihycroxycyclohexa-2,4-dien-1-yl)ethane-1,1,2-triol (DHC), with a mass of 188.2 Da. Both of these products were detected with similar peak areas at 2.5 and 3.1 V/SHE, but their detection was highly affected by the NaCl concentration (**Figure 5-3**). For example, at 2.5 V/SHE the 154.1 Da product was not detected at 5 mM NaCl concentration and the 187.2 Da product was not detected at either 1 or 5 mM NaCl concentrations. At 3.1 V/SHE, the 154.1 Da product was detected at both NaCl concentrations, but the 187.2 Da product was not detected at 5 mM NaCl concentration.

The reaction mechanisms responsible for organic chlorinated byproduct formation in the presence of NaCl are more complex and can involve reactions between a wide range of organic compounds and reactive chlorine species generated during the oxidation process. Based on the LC-MS experimental results, we hypothesize that a chlorinated alcohol product formed during the electrochemical oxidation of R in the presence of NaCl at 2.5 V/SHE. Since the LC-MS data suggested that this compound contained 4 Cl atoms (see **Appendix C, Figure C-6**), one possible product is $C_3H_4OCl_4$ (**Figure 5-4b)**, which has a mass of 195.9 Da and is close to the target mass

of 196.7 Da (see **Figure 5-3a**). At a potential of 3.1 V/SHE, this product was no longer observed, which suggests that it was further oxidized at this potential. **Figure 5-4b** shows the proposed chlorinated phenolic ($C_8H_7O_4Cl$) product, with a mass of 202.6 Da, which is similar to the target mass of the 202.1 Da. Furthermore, the proposed $C_8H_7O_4Cl$ product is similar to the proposed DHC compound (188.2 Da) that was assigned to the product detected at 187.2 Da (**Scheme 5-1**). The peak area for DHC decreased as a function of NaCl addition at 3.1 V/SHE (**Figure 5-3b**), suggesting that it or a similar compound could be a precursor for $C_8H_7O_4Cl$ formation.

The electrochemical pathways leading to the formation of the proposed chlorinated organic byproducts are complex and the fact that only one chlorinated product was observed at each anodic potential makes any proposed pathway speculative. However, the detection of a single compound at each potential suggests that these products are fairly recalcitrant at the given anodic potential and solution conditions. Therefore, DFT simulations were conducted to determine the potential dependent $\Delta G^{\ddagger}$ values for the oxidation of the chlorinated products via DET (equation 5-4). **Figure 5-4c** shows the potential dependent $\Delta G^{\ddagger}$ values for the chlorinated alcohol product ($C_3H_4OCl_4$), and **Figure 5-4d** shows the potential dependent $\Delta G^{\ddagger}$ values for the chlorinated phenolic product ($C_8H_7O_4Cl$). Modeling determined E^o = 3.04 V/SHE and λ_f = 34 kJ mol^{-1} for $C_3H_4OCl_4$, and E^o = 1.94 V/SHE and λ_f = 25 kJ mol^{-1} for $C_8H_7O_4Cl$. Results suggest that $C_3H_4OCl_4$ was resistant to DET at 2.5 V/SHE. For example, data in **Figure 5-4c** indicates that $\Delta G^{\ddagger}$ = 55 kJ mol^{-1} at 2.5 V/SHE and $\Delta G^{\ddagger}$ = 5.8 kJ mol^{-1} at 3.1 V/SHE for $C_3H_4OCl_4$. These findings are consistent with experimental results that showed the 196.7 Da compound was detected at 2.5 V/SHE but was not detected at 3.1 V/SHE. Furthermore, DFT calculations also indicated that the reactions between $OH^{\bullet}$ and $C_3H_4OCl_4$ were thermodynamically favorable for both H-abstraction and $OH^{\bullet}$ addition mechanisms (results not shown). By contrast, DFT simulations indicate that the $C_8H_7O_4Cl$ product

would react by DET without an activation energy at both 2.5 V/SHE and at 3.1 V/SHE (**Figure 5-4d**). Similar to other phenolic compounds, the $C_8H_7O_4Cl$ compound is also expected to react readily with $OH^{\bullet}$, indicating it was likely a transient intermediate. Therefore, its detection at 3.1 V/SHE indicates that pathway 3, which leads to C fragment addition to resorcinol (**Scheme 5-1**), was likely a primary pathway for formation of chlorinated organic compounds.

Products from the oxidation of the two detected chlorinated products were not observed experimentally. The lack of detection of additional products was likely due to the formation of nonpolar C1 and C2 chlorinated products that were not detected by LC-MS and/or further reacted to form CO_2 and Cl^- [203]. Further work is needed to characterize these nonpolar compounds and determine their concentrations relative to other EAOP electrodes.

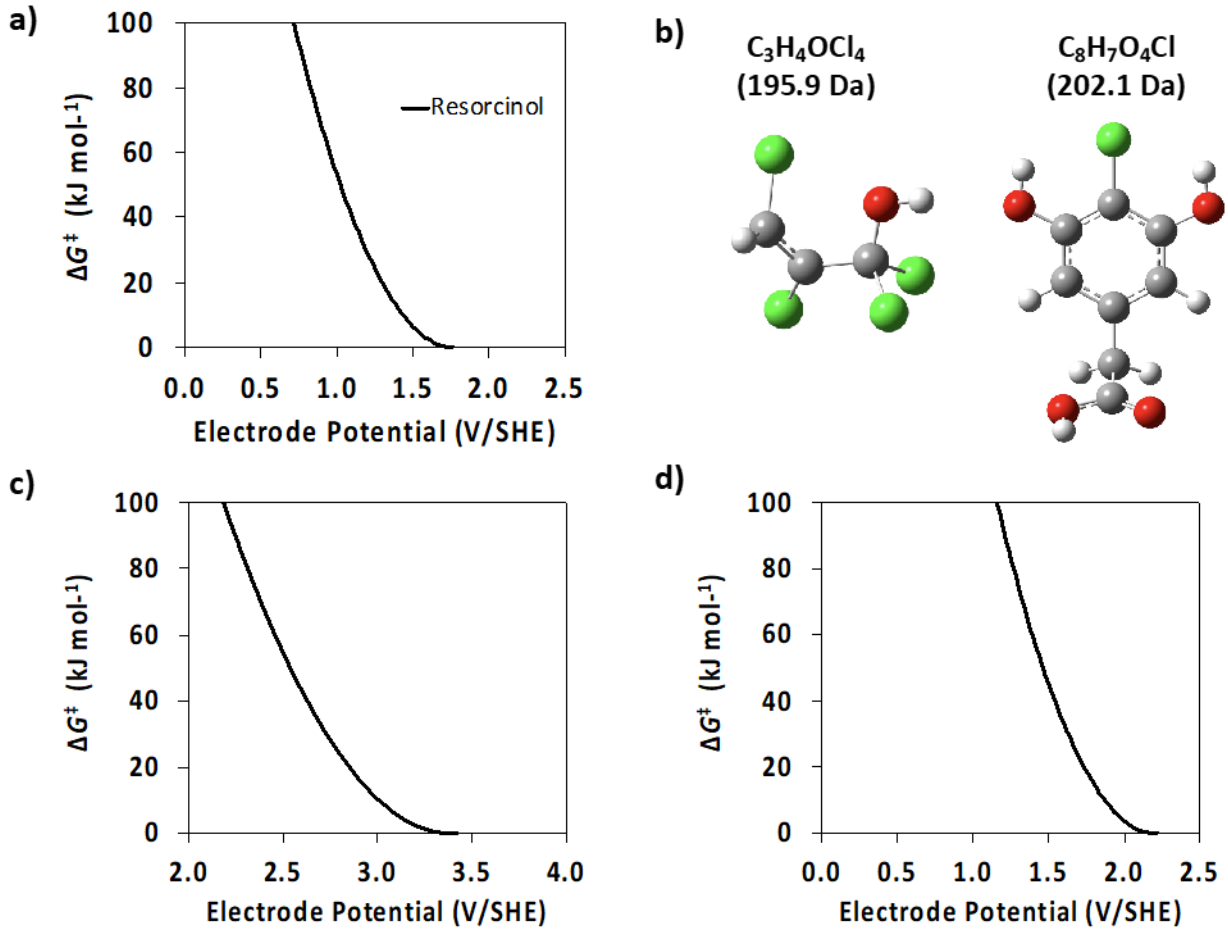

Figure 5- 4. a) Potential energy for resorcinol; b) Proposed structures for the 196.7 and 202.1 Da compounds; c) Potential energy for $C_3H_4OCl_4$; d) potential energy for $C_8H_7O_4Cl$. Atom key: carbon = grey; oxygen = red; hydrogen = white; chlorine = green.

5.4.5 Environmental Significance

The results reported in this study are the critical first step in understanding chlorinated byproduct formation on Ti_4O_7 electrodes under anodic conditions. Although it may be possible to eliminate all chlorinated organic byproducts through a combination of direct and indirect oxidation reactions, accomplishing this goal would require long residence times in the electrochemical cell, which in turn would favor inorganic chlorinated byproduct formation (e.g., ClO_4^-). The use of

Ti_4O_7 REMs for potable water treatment applications will require optimization of operating conditions and possibly a multi-barrier approach. Therefore, coupling an appropriate cathode material downstream of the Ti_4O_7 anode may be necessary to dehalogenate the halogenated organics that form under anodic conditions. Recently a carbon-composite Ti_4O_7 cathode was shown to efficiently dehalogenate a range of halogenated acetic acid compounds to below regulatory standards [204]. These tandem strategies need to be tested experimentally to determine their feasibility.

5.5 Acknowledgements

Funding for this work for BPC was provided by two National Science Foundation (CBET-1453081; CBET-1604776). Funding for CKR was provided by National Science Foundation (CBET-1451932).

6. Investigation the Effect of Microalgae Photosynthetic Activity under Different Anodic Potentials

6.1 Abstract

This research investigated low anodic potential (e.g., OCP to 1.0 V vs. Ag/AgCl) effects on algae photosynthetic activity. Oleaginous algae were used as a representative model based on the strain's high biomass, which is suitable for biofuel production. Hydroquinone (HQ) can be oxidized on the Pt UME surface and formed BQ, the n BQ can be oxidized to HQ through algae electro transport chain under light irradiation. Scanning electrochemical microscopy (SECM) provided near-surface mapping and algae current response measurements under anodic polarization during light irradiation. Results indicated that under anodic polarization, the attached algae exhibited a lower current response compared with OCP condition. Furthermore, it was observed that the current response from live attached algae does not correlate linearly with applied potentials. Normalized currents for attached live algae were decreased while applied potentials increased from OCP to 0.5 V vs Ag/AgCl, but increased at a potential of 1 V vs Ag/AgCl, which suggests that algae might limit photosynthetic activity under electrochemical pressure without incurring significant damage to the plasma membrane, cell wall and thylakoid membrane.

6.2 Introduction

Algae are a large and diverse group of photosynthetic aquatic organisms in nature which can convert solar energy into chemical energy while reducing CO_2. Also, the energy can be used to synthesize polysaccharides (sugars) and triacylglycerides (fats) through photosynthesis [21]. These molecules are the raw materials for producing bioethanol and biodiesel fuels. Oleaginous microalgae biolipids can be extracted up to around 20% of total biomass in dry weight, which are

attractive for biofuel production [22]. Algae harvesting and biolipid extraction are important steps for biofuel production but those processes can be energy-intensive and time-consuming, which include mechanical and non-mechanical techniques [13, 14]. On the other hand, algae blooms can be harmful and potential threats for water resources and human health. It affects water quality by changing the color, taste and odor. In addition, algae species can produce cyanotoxins including potent neurotoxins, hepatotoxins, cytotoxins, and endotoxins which can cause animal poisoning and rapid death by respiratory failure [15, 147].

Algae are also an ideal feedstock for the production of high energy density transportation fuels. Our previous work has resulted in the development of an innovative substoichiometric TiO_2 reactive electrochemical membrane (REM) filtration systems for algae harvesting, separation and pretreatment for lipid extraction. Charge transfer from photosysnthetic transport chain to a soluble redox couple provides the opportunity for algae viability determination [13, 34].

Quinones play a key role in fundamental biological processes as electron carriers in aerobic respiration (menaquinone or ubiquinone) or photosynthesis (plastoquinone). Recent studies have successfully shown the feasibility of harvesting the high energy photosynthetic electrons by electron mediators such as quinones, flavin mononucleotide (FMN) and phenazine methosulfate (PMS) [73]. Hydroquinone (HQ) is neutral and soluble in the cell membrane which allows it to shuttle electrons along the respiratory and photosynthetic chains. These properties allow quinones to be used as exogenous redox mediators in microbial applications to extract electrons from photosynthetic organisms [206], such as in protoplasts [207], isolated thylakoid membranes [208], isolated photosystem II complexes [209], or microbial metabolism [210].

Quantitative investigation of using p-benzoquinine (BQ) to extract photosynthetic electrons from a single living protoplast by extracellular microelectrode measurements has been

reported. Yasukawa [78] reported that carbon and gold (Au) disk microelecroedes can be used to monitor the localized concentrations of BQ and hydroquinone (HQ) near the cell under light irradiation. These results support the idea that BQ accepted two electrons from the photosynthetic respiratory electron transport chains (PSI and PSII) to form HQ. The electron transport can be monitored by reduction or oxidation current on the UME. Yue [73] used different wavelengths of light as irradiation source and found that the thylakoids have the weakest response at wavelengths in the range 500-700 nm, which is corresponding to green light. This finding indicates that the photocurrent indeed comes from the thylakoid membrane since the green color of most plants suggests the absence of absorption of green light by the chloroplast complexes. Longatte [211] used different quinones such as 2,6-dichlorobenoquinone (2,6-DCBQ), p-phenylbenoquinone (PPBQ) and other five quinones to estimate the efficiency of the exogenous quinones. 2,6-DCBQ was recommended for electrochemical applications as electron carriers in photosynthetic activities.

In our study, we focused on determining the effect of low anodic electrode potentials (< 2 V vs Ag/AgCl) on the photosynthetic activity and algae viability. Hydroquinone (HQ) was used as an exogenous redox mediator to partially short-circuit the electron transfer in algae during photosynthesis. Scanning electrochemical microscope (SECM) was used to characterize and record current responses, which were corresponding with HQ concentration at the algae surface and electron transfer through algae photosynthetic activity. Cell viability was measured and determined through direct count under microscopy.

6.3 Materia and Methods

6.3.1 Reagents

Sodium chloride (NaCl), potassium phosphate monobasic (KH_2PO_4) and (3-Aminopropyl)triethoxysilane, 98% (APTES), were purchased from Alfa Aesar (MA, USA). Hydroquinone (HQ) was purchased from Sigma-Aldrich (St. Louis, MO USA). Drisolv® anhydrous toluene was purchased from EMD Millipore (MA, USA). A MasterMet noncrystallizing colloidal silica (0.02 μm) polishing suspension was purchased from Buehler (IL, USA). Potassium phosphate dibasic anhydrous (K_2HPO_4) and SYTOX® Green nucleic acid stain - 5 mM solution in DMSO were purchased from Thermo fisher (MA, USA). Solutions were made from deionized (DI) water (18.2 MΩ cm at 21 °C). All chemicals were used as received.

6.3.2 Electrode Preparation and Characterization

Optically transparent electrode (OTE) was prepared as discussed in the previously published method [132], [212]. Briefly, OTE was fabricated at Fraunhofer USA Center for coating and Diamond Technologies (East Lansing, MI), which consisted of a BDD microcrystalline film deposited on a 2 mm thick quartz glass substrate using hot filament chemical vapor deposition (CVD) and cut into 1 cm^2 cylindrical disks using a laser cutting system (BDD/OTE). An APTES-functionalized BDD/OTE (APTES-BDD/OTE) electrode was prepared form BDD/OTE after cleaning with methanol, ethanol and water. The cleaned BDD/OTE was soaked in 5 mM APTES in anhydrous toluene and reacted for 3 h in an Ar-filled glovebox. The APTES-BDD/OTE was then rinsed three times with toluene and methanol and annealed at 120°C for 30 min to promote cross-linking of the silanes. The APTES-BDD/OTE provided the light transmittance and conductive surface for algae photosynthetic activity studies.

6.3.3 *Algae Cultivation and Attachment Process*

Oleaginous algae (Scenedesmus dimorphus or S. dimorphus) were cultured in the modified Bold's Basal Medium (MBBM) with details reported and provided previously [23]. Briefly, algae were cultured in 1-gallon LED aquarium at room temperature with 12 V recirculating pump to keep water flowing and 12h/12h light-dark cycle.

Before each experiment, algae were collected by centrifugation at 7000×g for 5 min at room temperature and washed with 100 mM potassium phosphate solution (70 mM K_2HPO_4 with 30 mM KH_2PO_4, pH = 7.6). The concentration of algae was quantified by optical density (OD) measurement at 750 nm (OD_{750}). The concentration of algae was ~10^8 cells mL^{-1} at OD_{750} = 1. After washing, algae cells were suspended in the SECM cell with 2 mL 100 mM potassium phosphate solution. Algae were set at OCP condition for 90 minutes for attachment on the APTES-BDD/OTE; then, the suspended unattached algae were washed from the system. A solution of 1 mM HQ with 100 mM phosphate (70 mM K_2HPO_4 with 30 mM KH_2PO_4, pH = 7.6) was refilled into the SECM cell. Different constant anodic potentials (OCP, 0.2, 0.5 and 1.0 V vs Ag/AgCl) were applied for 90 minutes on the substrate for investigating the electrode potential effects on algae photosynthetic activity. Post characterizations were conducted after these experiments.

6.3.4 *SYTOX® Staining Procedure*

Green fluorescence dye SYTOX® was used to label the damaged and dead cells. The dye can permeate through a compromised cell membrane and stain the nucleic acid but will not cross the membranes of uncompromised cells. The staining solution was prepared according to the manufacture [213]. Briefly, staining solution was prepared by diluting the stock solution 1:30,000 (167 nM) in a 0.85% NaCl solution and stored in the -20 ^oC freezer. Prior to staining, algae were

washed three times with a 0.85% NaCl solution. After washing, 2 µL of staining solution was added into each 200 µL of algae suspension. Algae were incubated in the staining solution at room temperature and in the dark for 20 minutes. A cover slide was placed over the OTE after staining and the algae cells were imaged at 20 individual random spots (128 by 128 µm area) using an inverted fluorescent microscope (Olympus IX73, Japan) with band-pass filter sets which have blue wide pass with excitation of 460-495 nm; emission 510-550 nm (FITC filter), and green wide long pass with excitation of 530-550 nm; emission 575 nm (TRITC filter). Algae have self-fluorescence and are observed as red dots under the TRITC filter and porated algae are observed as green dots under the FITC filter after STYOX® staining.

6.3.5 *Photosynthetic Activity Studies*

Scanning electrochemical microscopy (CHI 920D, CH instruments) was utilized for algae photocurrent measurement. Experiments used a platinum (Pt) working ultramicroelectrode (UME) with a diameter of 10 µm and an Ag/AgCl reference electrode, which were manufactured by CH instruments, Inc (TX, USA). A Pt counter electrode with a diameter of 0.5 mm was purchased from Alfa Aesar (MA, USA). A three-electrode setup was used in the SECM cell as shown in **Figure 6-1(a)**. The light source (Qoolife waterproof LED lights with 2.4 watts and wavelength of 400 to 700 nm) was positioned under the SECM cell for investigating algae photosynthetic activity. The light intensity was measured by a LX1330B digital light meter (Thousandshores Inc, CA, USA) at values of 15.7 kLux. The UME was located 2 µm above the attached algae during the photosynthetic activity measurement as shown in **Figure 6-1(b)**.

SECM was used for an investigation of algae electron-transport chain response through redox cycling of hydroquinone (HQ) between the substrate and tip in the substrate generation/tip collection (SG-TC) mode during photosynthetic activity as shown in **Figure 6-1(b)**. The current

measured at the UME increases with respect to the bulk steady-state current in the SG/TG mode, due to the oxidation of HQ to benzoquinone (BQ) at the UME and corresponding reduction back to HQ at the algae cell. The corresponding redox reaction with the standard electrode potential is shown in equation (6-1) and experiments maintained a constant potential at the UME of 0.5 V vs. Ag/AgCl for HQ oxidation. Concentration of 1 mM HQ was dissolved in the 100 mM potassium phosphate based solution (70 mM K_2HPO_4 with 30 mM KH_2PO_4, pH = 7.6). Potassium phosphate solution was prepared to use as chloride-free buffer for pH control. Traditional phosphate-buffered saline (PBS) which contains137 mM NaCl can form $Cl^{\bullet}$ or other Cl-based oxidants under applied anodic potentials, which may affect algae cells [212].

$$BQ + 2H^+ + 2e^- \leftrightarrows HQ \qquad E_o = 0.28\ V/SHE \qquad (6\text{-}1)$$

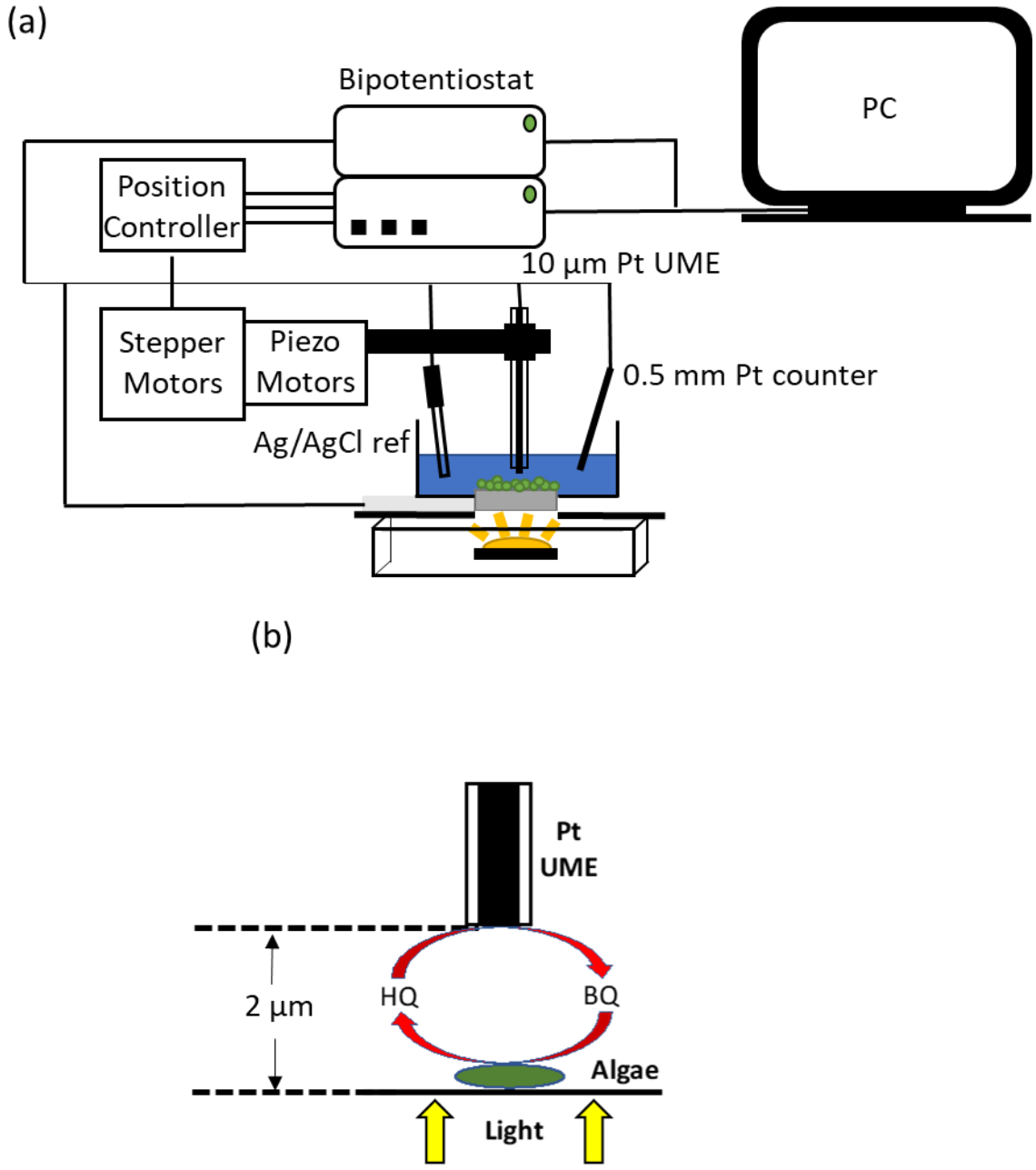

Figure 6- 1. Scanning electrochemical microscopy (SECM) setup (a) with 10 µm Pt UME, counter, reference electrode, OTE substrate with algae and light illustration with, (b) Pt UME was located 2 µm above the algae.

6.4 Results and Discussion

6.4.1 Attached Algae Surface Mapping Studies

Algae were suspended in the SECM cell for attachment and surface mapping studies. SECM surface mapping was conducted to determine hot spots of algae photosynthetic activity after applying different anodic potentials. In order to monitor the current response, the UME was held at oxidation potential of HQ (0.5 V vs. Ag/AgCl) and located 2 μm above the attached algae on the APTES-BDD/OTE. Attached algae surface mappings were conducted with and without light irradiation. The control image without attached algae is shown in **Figure 6-2(a)** and shows normalized currents < 1.0**,** which demonstrated the APTES-BDD/OTE did not reduce HQ at the OCP. Photosynthetic activity was observed during light irradiation and presented by surface mapping of the attached algae on the substrate as shown in **Figure 6-2(b)-(e).** Under the OCP and an applied potential of 0.2 V Ag/AgCl, localized areas of higher normalized current (>1) illustrated the photosynthetic activity of attached live algae on the substrate as shown in **Figure 6-2(b)** and **20(c)**. The characterization of algae that were exposed to applied potential of 0.5 V and 1 V Ag/AgCl, showed fewer hot spots and lower normalized currents, which were attributed to (1) the generation of small bubbles from water oxidation, which likely dislodged or (2) decreased algae viability and photosynthetic ability due to applied potentials as shown in **Figure 6-2(d)** and **(e)**.

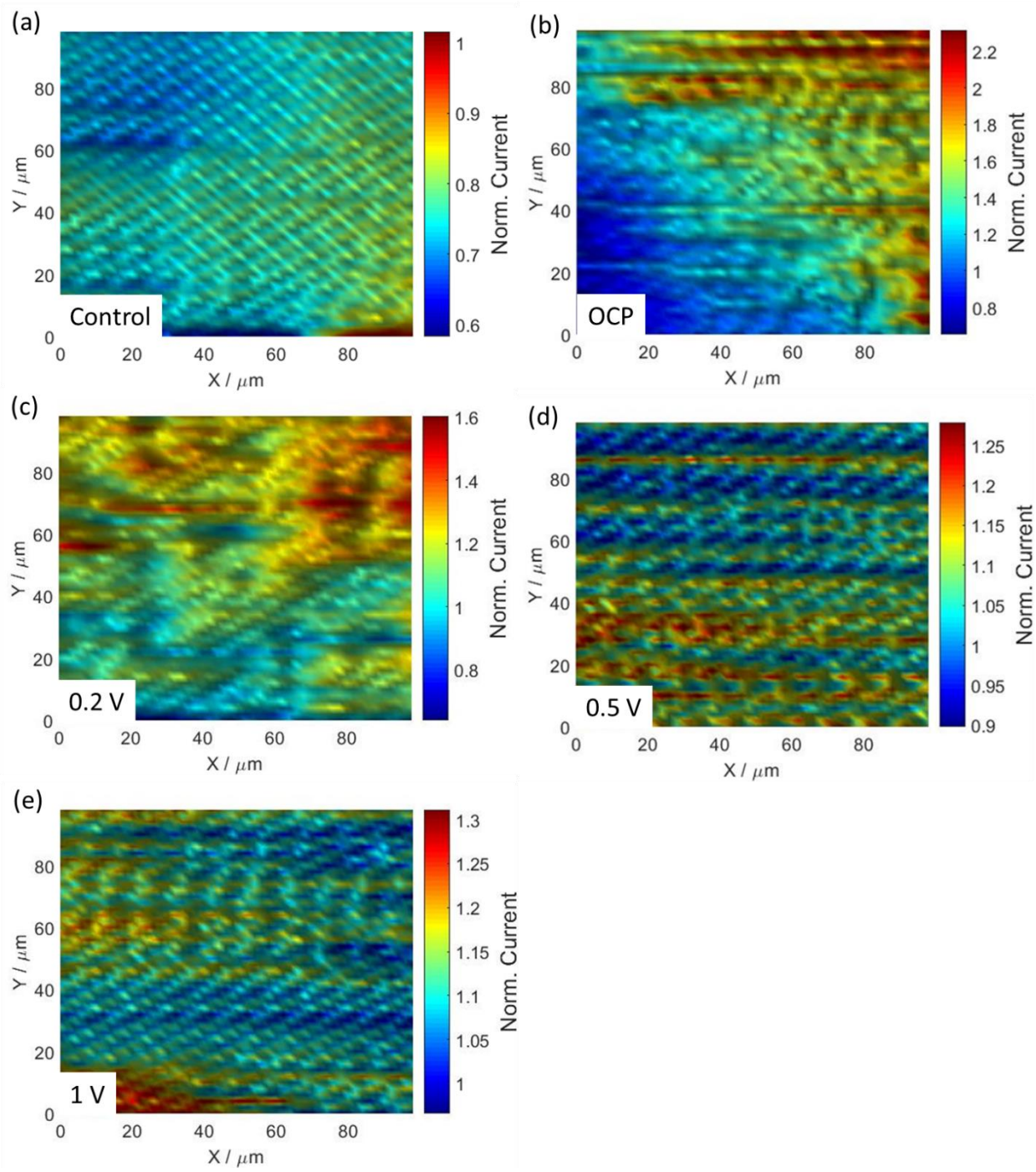

Figure 6- 2. SECM surface mapping of attached algae after applying different electrode potentials at (a) OCP, (b) 0.2 V, (c) 0.5 V and (d) 1 V vs Ag/AgCl. Figures were achieved by mapping under light irradiation diminished topographical mapping (without light irradiation).

6.4.2 *Algae Photosynthetic Studies*

After surface mapping, the UME was positioned 2 μm above the hot spots and held at an HQ oxidation potential 0.5 V vs. Ag/AgCl for monitoring algae photosynthetic activity. **Figure 6-3** shows the measured oxidation current of HQ at the Pt UME and demonstrated that a measured increase in the UME current was only observed in the presence of both algae and light irradiation. Control experiments without attached algae did not result in an increase in current under light irradiation. The oxidation current of HQ increased immediately after the light irradiation on the algae and decreased to the original level once the light was turned off. These results clearly demonstrate the ability of the algae cells to reduce the BQ redox couple from photosynthetically derived electrons, which is consistent with previous studies [73, 79, 214].

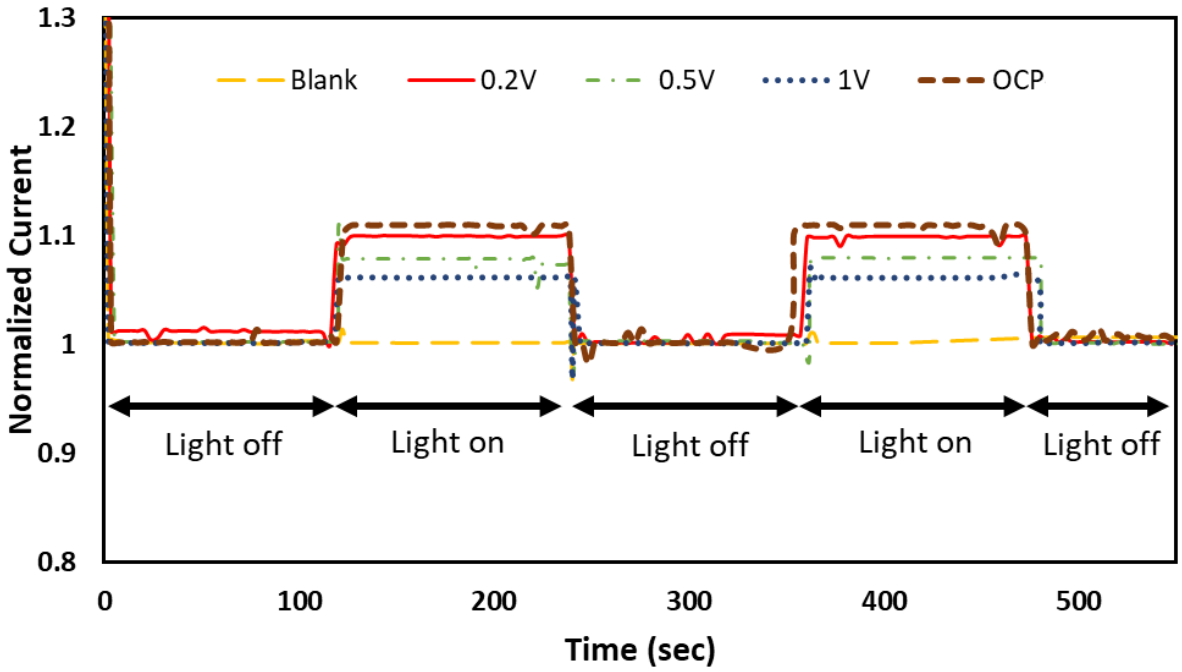

Figure 6- 3. Responses of oxidation current for 1 mM HQ upon light irradiation.

To understand the correlation between electrode potentials and algae photosynthetic responses, attached algae were stained and observed under the microscope after SECM surface mapping. Average of the total algae attachment on the APTES-BDD/OTE decreased while the applied potential increased as shown in **Figure 6-4(a),** which indicated the possibility of microbubble formation from water oxidation repulsed attached algae cells away from the APTES-BDD/OTE [212]. Also, the percentage of porated algae were determined based on the direct count after STYOX® staining. Results illustrated that less than 10% of the porated algae were observed at OCP, 0.2, and 0.5 V vs Ag/AgCl, but around 30 ± 9% of algae were porated at an applied potential of 1.0 V vs Ag/AgCl for 90 minutes as shown in **Figure 6-4(b)**. Before staining, UME was located 2 μm above the attached algae and held at HQ oxidation potential 0.5 V vs. Ag/AgCl to measure the algae photosynthetic current response under light irradiation. Normalized current was determined by measured current from UME divided by the total number of attached algae. Results as shown in **Figure 6-4(c)** illustrated that the normalized current from the attached algae decreased while the applied potential on the electrode increased. This result might be due to poration or inactivation of some of the attached algae, which reduced their photosynthetic activity. For a deeper understanding of the effects of electrode potential on the algae photosynthetic activity, normalized currents were normalized by the attached live algae numbers at each anodic potential condition as shown in **Figure 6-4(d)**. In general, live cell normalized currents decreased while applied potentials increased from OCP to 0.5 V vs Ag/AgCl, but normalized currents increased at a potential of 1 V vs Ag/AgCl. These results suggested that the attached algae cells may have lost photosynthetic ability after electrolysis at 0.5 V vs Ag/AgCl for 90 minutes but remain algae self-fluorescent, which can be observed under the microscope. In other words, attached algae at an electrode potential of 0.5 V vs Ag/AgCl might not have any significant damage of the cell wall or

plasma membrane but photosynthetic activities were inhibited. Furthermore, while applied potential increased to 1V vs Ag/AgCl, more attached algae might be porated and photosynthetic abilities were simultaneously inhibited. The error bars represent the standard deviation about the mean values.

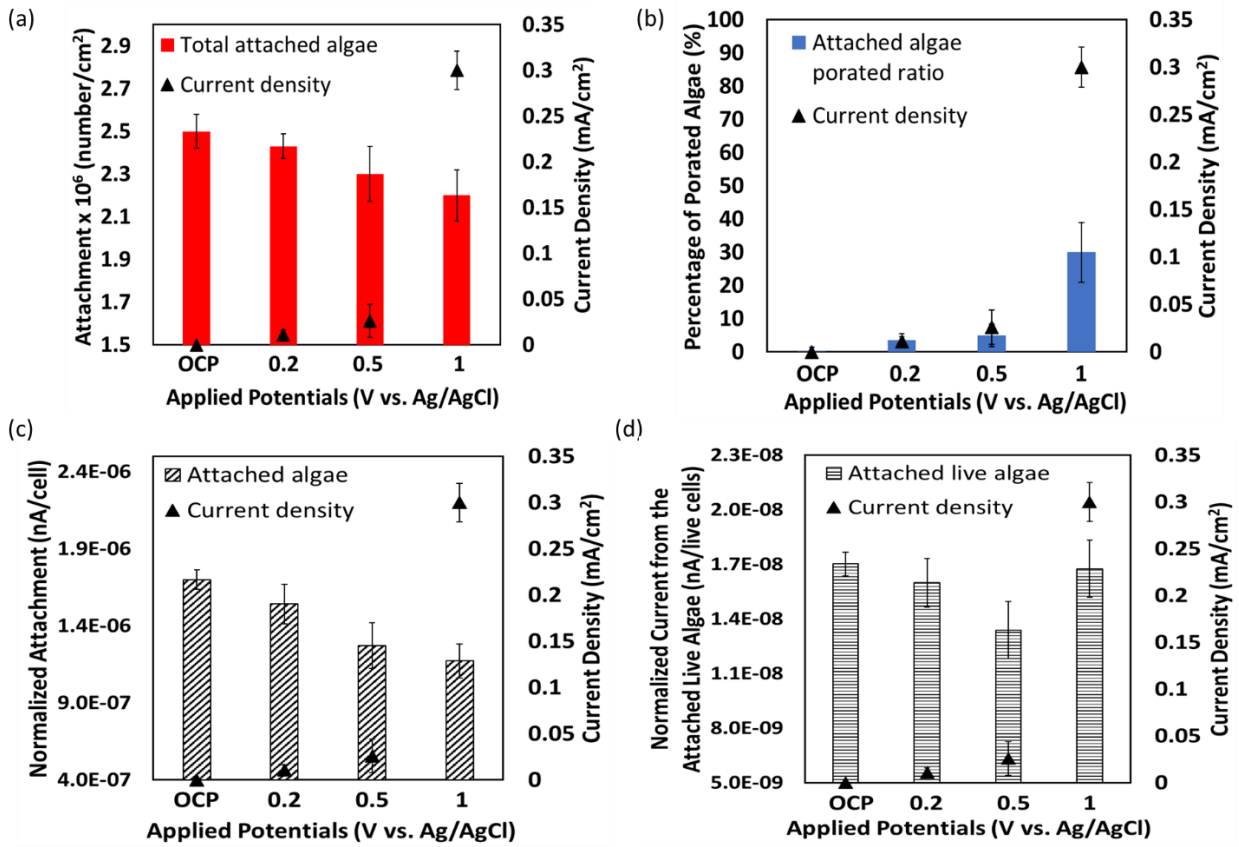

Figure 6- 4. Comparison of (a) the algae attachment potentials (bars), (b) the percentage of porated algae, (c) the normalized current from the total attached algae (bars) under light illustration and (d) the normalized current from the attached live algae (bars) under light illustration on the APTES-BDD/OTE as a function of the applied potential. The data points represent the measured current.

6.5 Conclusion

The results provide proof-of-concept data that illustrated that the BQ/HQ redox couple could be used during SECM experiments to characterize the photosynthetic activity of algae cells.

Also, the algae photocurrent measurement from the attached algae were affected by the applied anodic potentials on the electrode. However, the electrode potentials might reduce the algae photosynthesis or respiration ability for electro transport but cannot be directly observed through algae cell live/dead staining under microscope characterization. These results offered insights for monitoring algae harvesting, biomass separation and cell treatment processes for biofuel production that are relevant for reactive electrochemical membrane separation techniques.

7. CONCLUSIONS AND FUTURE RESEARCH

Work presented in this dissertation focused on understanding the mechanisms of biofouling control, chlorinated byproduct formation, and algae photosynthetic activity at electrode surfaces as a function of electrode potential and solution conditions. Research began with an emphasis on bacteria attachment and poration mechanisms at the electrode surfaces. The current state of knowledge in the field regarding biofouling control with electrochemical methods were focused on higher applied potentials (> 1.5 V vs. Ag/AgCl) but the mechanisms for bacteria poration at low applied potentials were not thoroughly understood. This research contributed to investigate bacteria poration mechanisms at electrode surfaces at low applied potentials (−0.2 to 1.0 V vs Ag/AgCl). Results from **Chapter 3** showed that electrostatic interactions between bacteria and ionic electrode functional groups facilitated bacteria attachment at the open-circuit potential (OCP). However, under polarization, the applied potential governed these electrostatic interactions and electrochemical reactions resulted in surface bubble formation and near-surface pH modulation that decreased surface attachment under anodic conditions. For bacteria poration mechanisms, a combination of pH change and oxidant formation at the OTE surfaces were the primary contributors to bacteria poration. Under cathodic conditions, the near-surface pH was 8.0 at −0.2 V vs Ag/AgCl and was possibly a contributor to bacteria poration. Oxidant production had a limited role in bacteria poration until cathodic potentials were more negative than −0.5 V vs Ag/AgCl, which corresponded to H_2O_2 formation. On the other hand, under anodic conditions, the near-surface pH was 3.1 at 1.0 V vs Ag/AgCl and a combination of H_2O_2, $Cl^{\bullet}$, $HO_2^{\bullet}$ $Cl_2^{\bullet-}$, and Cl_2 formation likely contributed to bacteria poration at potentials as low as 0.5 V vs Ag/AgCl.

Extending work from **Chapter 3** an N-propyl-2-hydroxyacetamide group functionalized BDD electrode (OH-BDD/OTE) was designed for studying chelation induced bacteria poration at

the electrode surface with low applied potentials (e.g., −0.2 to 1 V versus Ag/AgCl), which was reported in **Chapter 4**. Results suggested that divalent ions from the outer membrane of bacteria were chelated by these N-propyl-2-hydroxyacetamide functional groups. It was observed that two- to three-fold higher percentage of porated bacteria were observed on the OH-BDD/OTE compared with BDD/OTE under applied anodic potentials between 0.1 to 0.5 V vs. Ag/AgCl. DFT simulations suggested that divalent cation chelation by the 2-hydroxyacetamide functional group was thermodynamically favorable ($\Delta G = -180$ kJ mol^{-1}). Solution phase experiments were conducted by measuring bacteria surface charge in the presence of EDTA, glycolic acid (GA) and divalent cations. Results showed that additional chelators (EDTA and glycolic acid) can extract the divalent ions from the cell membrane and cause cell destabilization and showed higher negative zeta potential measurements. A mathematical model based on the nonlinear Poisson–Boltzmann equation was conducted to support the chelation hypothesis and experimental results. Results suggested that proper surface modification can improve biofouling control on electrode surfaces that operate at low applied potentials (e.g., capacitive deionization).

Electrochemical advanced oxidation processes (EAOPs) have been intensely researched as possible technologies for water treatment. Although EAOPs successfully degrade most target contaminants, chlorinated byproducts may also form during EAOPs. Chlorinated byproduct formation at a porous Magnéli phase Ti_4O_7 reactive electrochemical membrane (REM) was evaluated in **Chapter 5**. Resorcinol was used as a model organic compound, and it was oxidized in the presence of NaCl (1 and 5 mM) and as a function of electrode potential. Resorcinol mineralization was >79% in the presence and absence of NaCl at 3.1 V/SHE (residence time = 13 s). Results indicated that ~4.3% of the initial chloride was converted to inorganic byproducts (free Cl_2, ClO_2^-, ClO_3^-) in the absence of resorcinol and this value decreased to < 0.8% in the presence

of resorcinol. Perchlorate formation rates from chlorate oxidation were 115—371 μmol m^{-2} h^{-1}. A multi-chlorinated alcohol compound (C_3HCl_4OH) at 2.5 V/SHE and a mono-chlorinated phenolic compound ($C_8H_7O_4Cl$) at 3.1 V/SHE were proposed as possible structures. Results suggested that chlorinated byproducts should be carefully monitored during EAOPs and multi-barrier treatment approaches are likely necessary to prevent halogenated byproducts in the treated water.

Porous Ti_4O_7 REMs were also studied as efficient algae filtration systems. Significant algae disruption and reduced photosynthetic activity were observed under anodic oxidation by a Ti_4O_7 REM. The applied anodic potential effect on algae photosynthetic activity was investigated in **Chapter 6**. A conductive, non-porous APTES-BDD/OTE was used for primary investigation and low anodic potentials (e.g., OCP to 1.0 V vs. Ag/AgCl) were applied. The hydroquinone/benzoquinone redox couple was used in SECM measurements as a redox mediator to extract electrons from algae's electron transport chain under light irradiation, which was used as a measure of algae's photosynthetic activity. Also, algae viability was determined through microscopy. Results indicated that under anodic polarization, the attached algae exhibited a lower current response compared with the OCP condition. Furthermore, it was observed that the current response from live attached algae does not correlate linearly with applied potentials. Normalized currents for attached live algae decreased while applied potentials increased from OCP to 0.5 V vs Ag/AgCl, but increased at a potential of 1 V vs Ag/AgCl, which suggests that algae may lose photosynthetic activity before incurring significant damage to the plasma membrane, cell wall, and thylakoid membrane. This study provides insight on algae behavior in electrochemical systems by characterizing algae biological viability and monitoring their photosynthetic activity after exposure to anodic potentials.

The results and conclusion presented in this dissertation imply several opportunities for future research. Chapter 3 and 4 showed that oxidant formation and near-surface pH were two main contributors for bacteria poration at the electrode surface under low applied potentials in a batch system. In addition, chelation site surface modification can increase the attached bacteria poration ratio. In Chapter 4, it was hypothesized that when the electrode is polarized as a cathode, the electric double layers of the adsorbed bacteria cells and the electrode begin to overlap. However, the exact mechanisms of the thermodynamically favorable binding processes and double layer effects are still unclear between chelation sites, Mg^{2+} ions and the bacteria membrane surface. Future research should evaluate (1) changes of double layer capacitance between bacteria cells and polarized electrodes, and (2) the thermodynamically favorable binding processes between chelation sites, Mg^{2+} ions and the bacteria membrane surface. Electrical impedance spectroscopy (EIS) can detect small changes occurring at the solution–electrode interface. Studies using EIS as biosensor to evaluate bacteria live/dead performance [215], concentration of attached bacteria [216, 217] and redox labeled electron transfer between bacteria and electrodes [218, 219] through electrochemical cell impedance changes. Hence, EIS can be used in future research for characterizing the differences of electric double layers and charge transfer resistance between adsorbed bacteria cells and polarized electrodes. In addition, two methodologies (1) surface plasma resonance (SPR) and (2) maker molecules can be used to determine binding affinity or kinetic parameters between chelation sites, Mg^{2+} ions and the bacteria membrane surface. SPR allows qualification of associate and dissociation constants between molecules from solution to a ligand immobilized on the surface [220], which can possibly be used to determine binding affinities or kinetic parameters between Mg^{2+} ions and chelation sites. Besides, to study the binding interaction between bacteria and Mg^{2+}, lipopolysaccharide (LPS) can be extracted from bacteria outer

membrane [220, 221] and immobilized on the surface as a ligand. Therefore, binding affinity measurements between LPS with Mg^{2+} ions can also be estimated by SPR [222]. Moreover, another insightful study shows that maker molecules can also be implemented to identify binding sites on the LPS (e.g. radioactive $^{45}Ca^{2+}$ can be used as maker for negatively charged lipids). Characterizing β-radiation intensity can be used to investigate the adsorption of $^{45}Ca^{2+}$ to LPS [223]. Results of this study would be useful for comprehensive understanding of thermodynamically favorable binding processes between divalent ions, chelation sites, and the bacteria membrane surface.

Chapter 5 summarizes the results from a study on chlorinated byproduct formation on Ti_4O_7 electrodes under anodic conditions. The use of Ti_4O_7 REMs exhibit promise to eliminate formation of chlorinated byproducts, inorganic byproducts (free Cl_2, ClO_2^-, ClO_3^-) and halogenated byproducts during EAOPs. However, the study represented a simplified system and not all possible chlorinated byproducts were analyzed. Future research is needed to explore more comprehensive aqueous solutions and the range of byproducts that may form as a function of solution conditions. In addition, combining Ti_4O_7 REM with other technologies for water treatment applications should be explored in order to prevent chlorinated byproducts from remaining in the treated water. For example, studies have shown that granular activated carbon (GAC) adsorption [224], nanofiltration [71], photocatalytic dehalogenation [225, 226][225], [226], carbon nanotube (CNT) and carbon-based electrodes [226], [227] present promising results for halogenated byproduct removal. Furthermore, recently a carbon-composite Ti_4O_7 cathode was also shown to efficiently dehalogenate several halogenated acetic acid compounds. Therefore, future studies are needed to investigate Ti_4O_7 REM coupling with other methodologies after EAOPs to dehalogenate halogenated organics below regulatory standards in the permeate solution.

Chapter 6 provides insight on the correlation of photosynthetic activity and algae viability as a function of electrode potential. To extend this study, the SECM methodology used in Chapter 6 can be conducted to determine the effects of heavy metals on algae viability. Prior studies have illustrated that heavy metals present in the environment can accumulate in algae and other aquatic plants, which can inhibit growth rates and reduce photosynthesis [228–230]. Existing methods might cause algae damage or lead to inaccurate results due to indirect measurements. Hence, the current methodology provided in Chapter 6 can be implemented in future studies to evaluate the effect of different heavy metal concentrations in solution and provide direct measurements of algae photosynthetic activity and viability at low algae concentrations. Results of this study might be useful to ultimately determine the risk assessment of heavy metals in the water system through algae photosynthetic and viability measurements.

Appendices

Appendix A

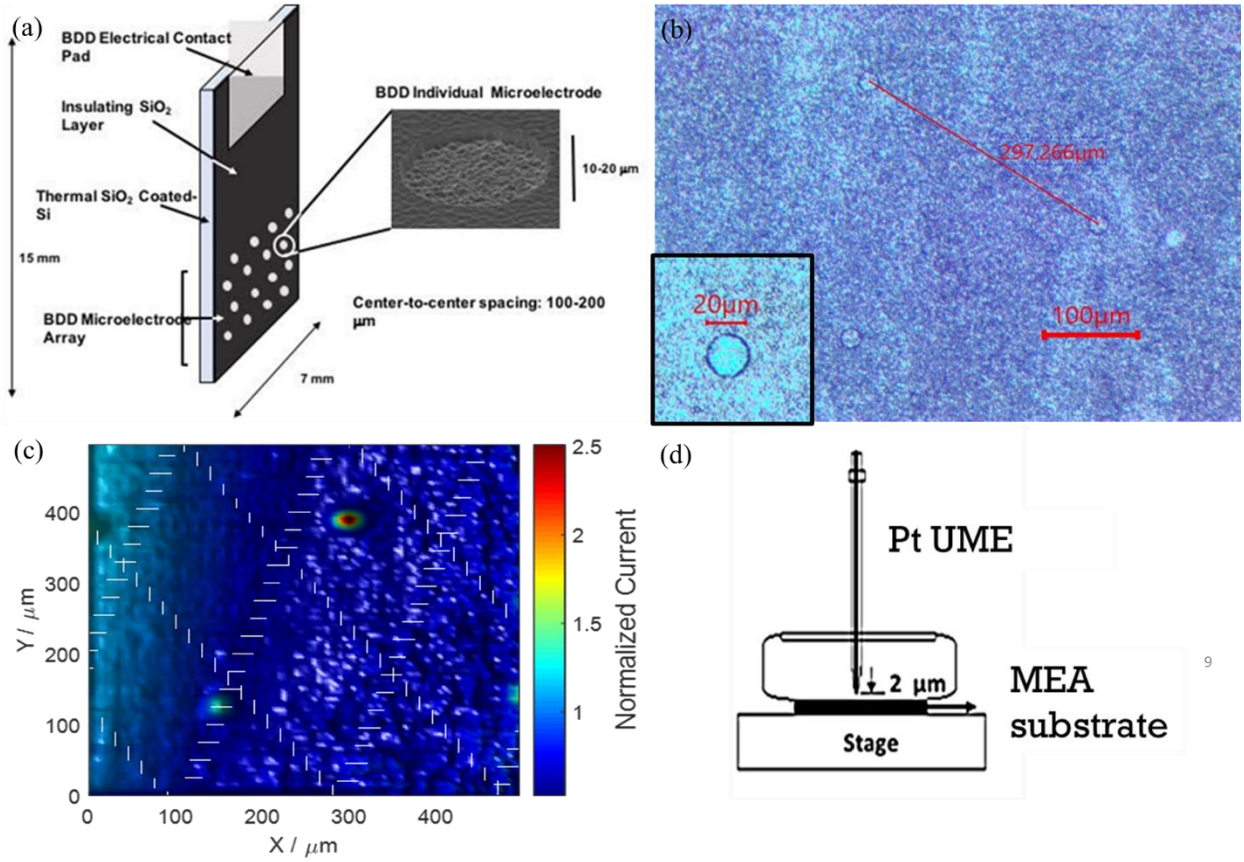

Figure A- 1. (a) Schematic of MEA (b) Microscopy images of MEA (c) Pt UME was held under cathodic potential for oxygen reduction (-0.6 V v.s Ag/AgCl) and scanned area 500×500 of MEA for positioning (d) UME was located 2µm above the MEA substrate.

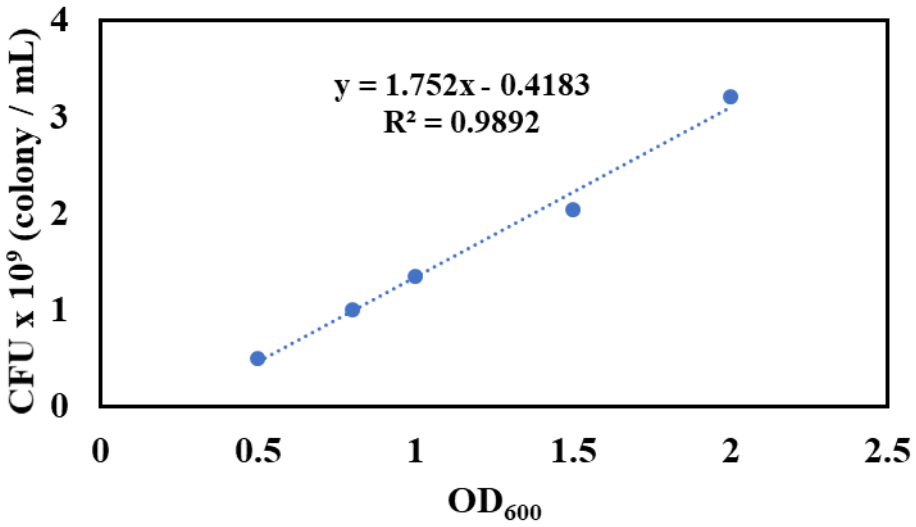

Figure A- 2. The relationship between the reading number of OD_{600} and bacteria number in 1 mL solution.

A.1 Dual staining procedure

Prior to staining, bacteria were washed three times with a 0.85% NaCl solution. The viability/cytotoxicity assay was prepared by mixing 10 µL of DMAO, 20 µL of Ethidium Homodimer-III (EthD-III), and 80 µL of 0.85% NaCl. DMAO is a green nucleic acid dye that stains both live and dead bacteria (excitation 503 nm/ emission 530 nm), while EthD-III is a red dye (excitation 530 nm/ emission 620 nm) that only stains cells with a damaged outer membrane. Freshly mixed reagent solutions were prepared before each experiment.

A.2 Bacteria attachment / poration studies

After washing with a 0.85% NaCl solution, 1 µL of reagent solution was added into each 100 µL of bacteria suspension after each attachment experiment. The bacteria were incubated in the reagent solution at room temperature and in the dark for 15 minutes. A cover slide was placed over the OTE after staining and the cells were imaged by using an inverted fluorescent microscope

(Olympus IX73, Japan) with band-pass filter sets which have blue wide pass with excitation 460-495 nm; emission 510-550 nm (FITC filter), and green wide long pass with excitation 530-550 nm; emission 575 nm (TRITC filter). Attachment and live/poration bacteria numbers under each condition with different applied potentials were counted manually and averaged from the 10 individual random spots. Each image represented one spot which captured 11754 μm^2 on the OTEs as shown in Figure S5. Live bacteria displayed green dots on the images under FITC filter and porattion bacteria displayed as red dot under TRITC filter after staining. Total attachment number was determined by combing both live and poration bacteria number on the OTEs. Duplicated experiments were utilized.**UME pH Probe Fabrication.** A 75 mg portion of iridium tetrachloride was dissolved in 50 mL of water and magnetically stirred for 30 minutes. After that, 0.5 mL 30% H_2O_2 was added and stirring was maintained for another 10 min. Oxalic acid dehydrate (250 mg) was added into the solution and stirred for 10 additional minutes. The pH of the solution was adjusted to 10.5 by addition of K_2CO_3. The solution was covered and left at room temperature for 2 days in order for iridium oxide to form. The anodic deposition was performed on a commercial 10 μm diameter Pt UME (CHI107P, CH Instrument, Inc) Prior to IrO_2 deposition, the Pt UME was polished with a 0.02 μm colloidal silica suspension on a 1200 grit polishing pad. The current density was maintained at 0.16 mA cm^{-2} for 30 minutes for the electrodeposition process. The UME was then washed with DI water and air-dried. The electrode was coated with a Nafion® film by dipping it into a 5.0 wt. % Nafion solution for 10 seconds. The film was air-dried for 20 minutes. The IrO_2 UME was immersed in pH 7.0 buffer solution for 2 days for stabilization.

A.3 Reaction-Diffusion Model

A reaction-diffusion model was developed to interpret experimental SECM data on SG-TC mode where two species, H_2O_2 and $Cl^{\bullet}$, were generated at the substrate. The model simulates the reaction and diffusion of these species between BDD and UME tip surface at steady state in two dimensions and axisymmetric configuration (see Figure A3). Given the concentration of the two species, c_1 and c_2, the following coupled differential equations illustrate the reaction and diffusion of both species:

$$\begin{cases} \frac{\partial^2}{\partial x'^2}(x'c'_1) + \frac{\partial^2}{\partial y'^2}(x'c'_1) = \frac{1}{\alpha'}c'_1c'_2x' \\ \frac{\partial^2}{\partial x'^2}(x'c'_2) + \frac{\partial^2}{\partial y'^2}(x'c'_2) = \frac{1}{\alpha'}c'_1c'_2x' + \frac{1}{\beta'}c'^2_2x' \end{cases}, \tag{A1}$$

subject to the following boundary conditions for the problem domain depicted in Figure A6

$$\begin{cases} \frac{\partial c'_1}{\partial y'} = 1,\ \frac{\partial c'_2}{\partial y'} = 1 \quad \text{along AB} \\ \frac{\partial c'_1}{\partial x'} = \frac{\partial c'_2}{\partial x'} = 0 \quad \text{along BC, FG and AI} \\ \frac{\partial c'_1}{\partial y'} = \frac{\partial c'_2}{\partial y'} = 0 \quad \text{along CD and GH} \\ c'_1 = c'_2 = 0 \quad \text{along DE and EF} \\ c'_1 = \frac{\partial c'_2}{\partial y'} = 0 \quad \text{along HI} \end{cases} \tag{A2}$$

where prime indicates nondimensionalization,

$$x' = \frac{x}{b}\ ,\ y' = \frac{y}{b}\ ,\ c'_1 = \frac{c_1}{c_0}\ ,\ c'_2 = \frac{c_2}{c_0}\ ,\ \alpha' = \frac{D^2}{k_r v_1 b^3}\ ,\ \beta' = \frac{D^2}{k_s v_1 b^3}\ ,$$

in which $b = \min(a,\ \sqrt{D/(k_r\, c_0)}\ )$, a is the UME tip radius, $c_0 = [v_1^2/(D\, k_r)]^{1/3}$ is the dimensional concentration scale, D is the diffusion coefficient (assuming both species have identical diffusivity), $k_r = k_{Cl^{\bullet},H_2O_2}$ is the second-order homogeneous reaction rate constant, $k_s = k_{Cl^{\bullet},Cl^{\bullet}}$ is the rate of reaction 12, and v_1 is the generation rate of both H_2O_2 and Cl-based oxidants

at the BDD substrate. The presence of x' in equation A1 is due to conversion of cylindrical to Cartesian coordinates. The coupled reaction-diffusion equations S1 with boundary conditions in equations A2 were solved numerically using Finite Element Method (FEM) implemented in Matlab.

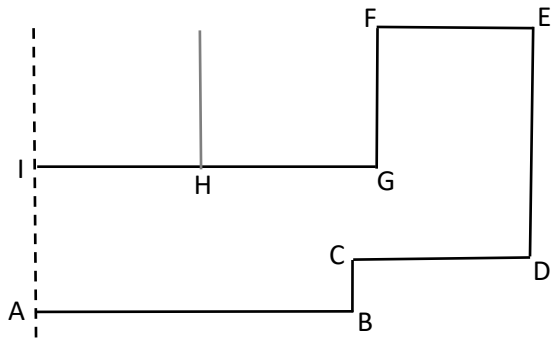

Figure A- 3. Schematic of the axisymmetric 2D geometry in which reaction-diffusion equations are solved numerically. Dashed line is the axis of symmetry, AB=31.6 is the BDD surface, BC=3.1, CD=19.0, DE=23.8 and EF=17.4 representing far boundaries in the bulk, FG = GH = 17.4 illustrate the glass sheath surface, HI=15.8 is the UME tip, and AI=9.5. All lengths are nondimensionalized by b.

A.4 APTES Modified BDD Coverage Calculation

APTES coverage ratio on the BDD was calculated based on XPS results and chemical structure. The C/N ratio of APTES was 3:1 based on the chemical structure, C/N of BDD was 59.5 and C/N of APTES-BDD was 18.5 based on the XPS results. Therefore, the coverage ratio (X) can be calculated by (C:N) APTES-BDD =(1-X) (C:N)BDD+ X(C:N)APTES.

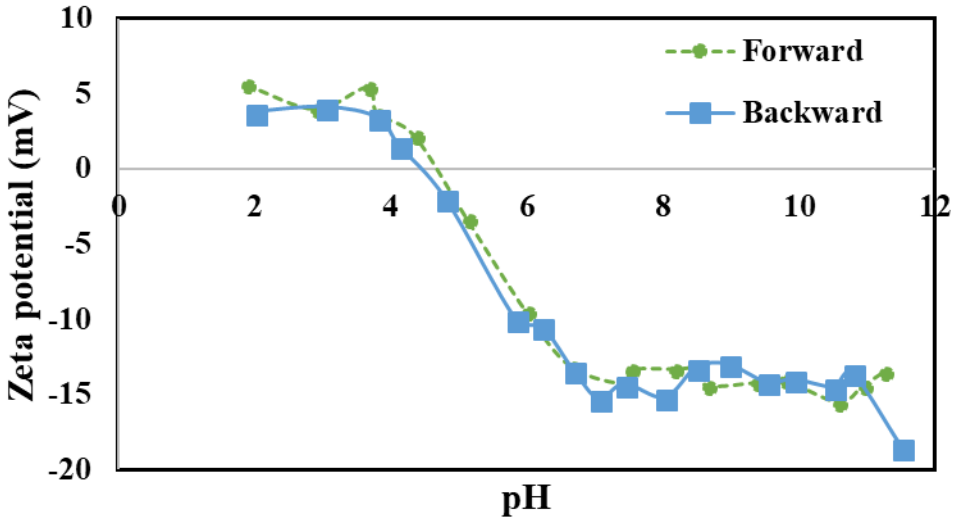

Figure A- 4. PAO1 bacteria zeta potential in different pH solutions.

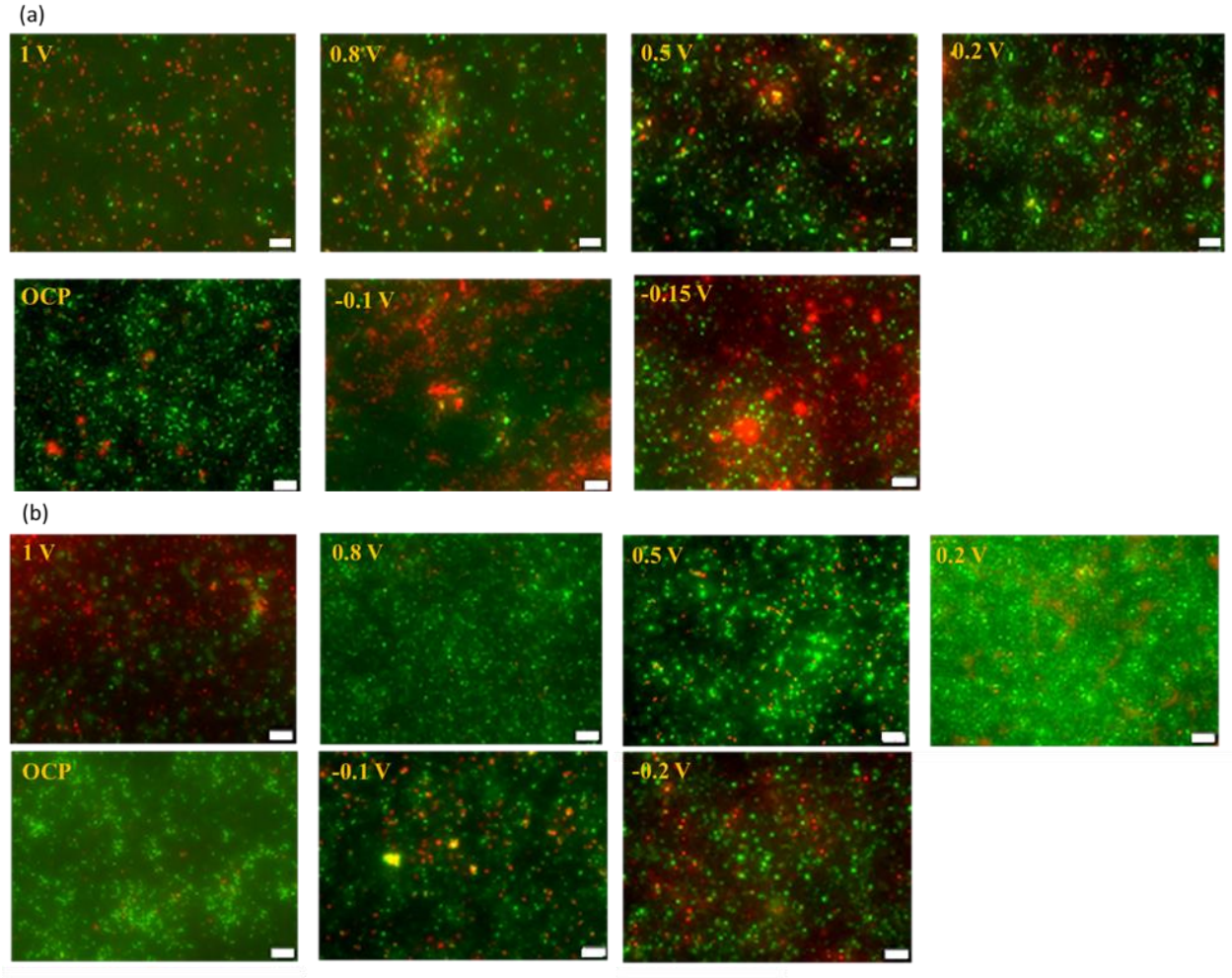

Figure A- 5. Fluorescent images showing live (green) and dead (red) POA1 cells on (a) BDD/OTE and (b) APTES-BDD/OTE electrodes under different applying potentials, which are referred to in the article. Potentials are vs. Ag/AgCl. (bar = 10 μm)

Table A- 1. The electric field in the SECM system for attachment and inactivation studies while applying different potentials on the electrode.

Working Electrode Potential (V vs. Ag/AgCl)	Cell potential (V)	Electric Field (V/m)
1	1.4	494.7
0.8	0.99	349.8
0.5	0.68	240.3
0.2	0.31	109.5
0.1	0.13	44.2
OCP	0.1	34.3
-0.05	-0.07	-23.7
-0.1	-0.11	-37.5
-0.2	-0.23	-79.9

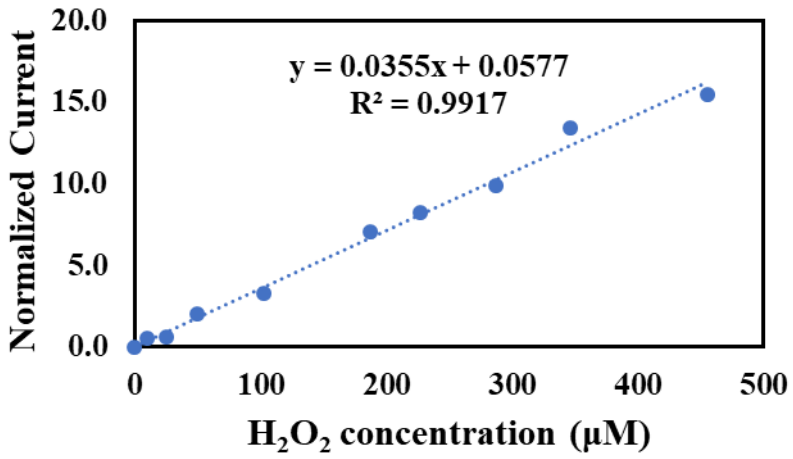

Figure A- 6. The calibration curve of H_2O_2 concentration vs. current on the Pt UME while UME was held at 0.9 V vs. Ag/AgCl (R^2 = 0.99).

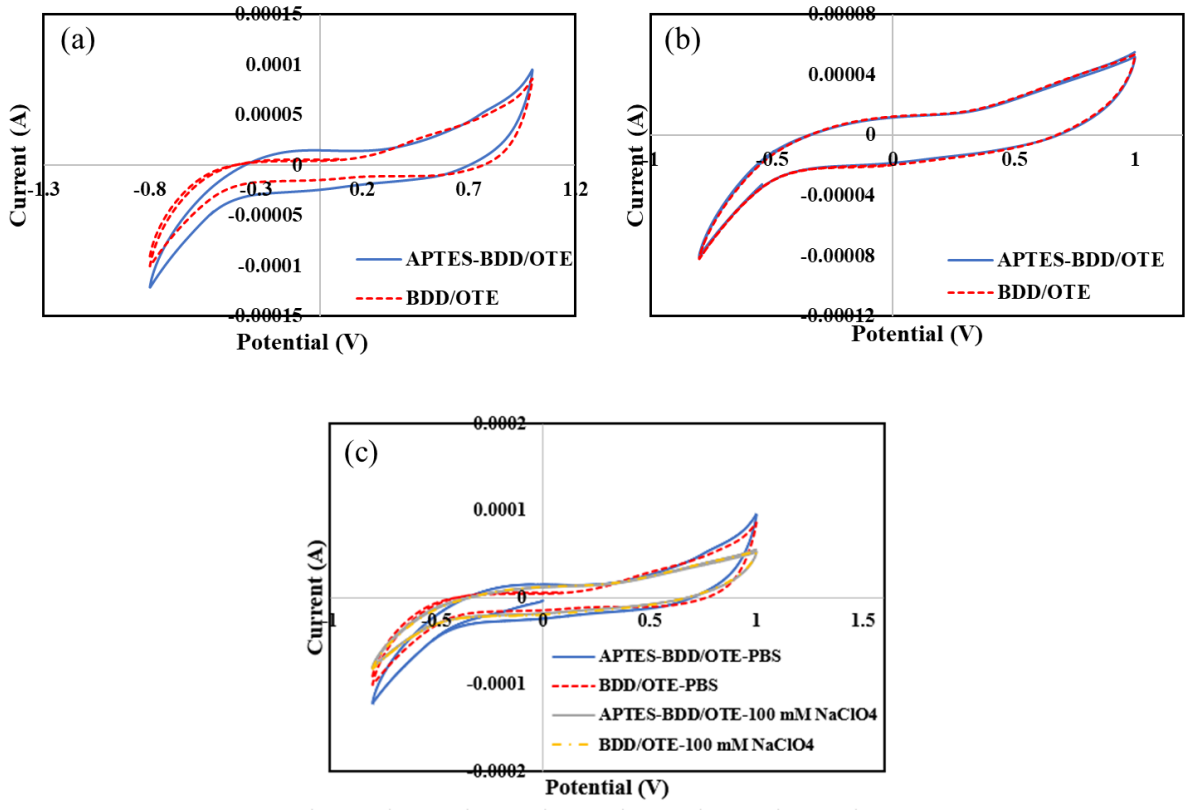

Figure A- 7. Cyclic Voltammogram (CV) curves of bare BDD/OTE and APTES-BDD/OTE in the (a) phosphate buffer solution (PBS) (b) 100 mM $NaClO_4$ and (c) the comparison of both solutions on both BDDs **.**

Appendix B

B.1 Electrode modification process

The EDC/NHS method was applied to crosslink amide with carboxylic acids [147, 148]. The mechanism of EDC/NHS reaction is shown in **Figure B-1** [231]**.** The mechanism involves the mixing of glycolic acid (1) with 1-(3-Dimethylaminopropyl)-3-ethylcarbodiimide (EDC) (2). The O-acylisourea intermediate (3) was formed by reaction between the carboxylic acid and EDC, which is usually unstable in aqueous solutions. NHS (4) was added for stabilizing the final product and improving the crosslink efficiency. The NHS reacts with the O-acylisourea intermediate and forms the semi-stable amine reactive NHS ester (5). Compound (5) crosslinks with the amino group on the APTES-BDD/OTE (6). The final N-propyl-2-hydroxyacetamide functional group was formed on the BDD/OTE (7). The process was conducted in the pH 5.0 MES buffer, which is suitable for carbodiimide reaction without primary amine or carboxyl groups present.

These reaction steps were carried out on an APTES-BDD/OTE. First, 5% volume of GA was dissolved in the 5 mM MES buffer solution in the beaker and stirred for 30 minutes until chemicals were well dissolved. 5 mM EDC was added into this solution to react with GA for another 30 minutes. Then, 5 mM water soluble NHS and APTES-BDD/OTE electrode were added into the beaker for further crosslinking process of GA on the APTES-BDD/OTE. The beaker was covered with paraffin and set in the shaker with a rotation speed of 160 rpm at room temperature for 20 hours. Last, the OH-BDD/OTE was washed by water three times to remove the unreacted GA and dried at room temperature.

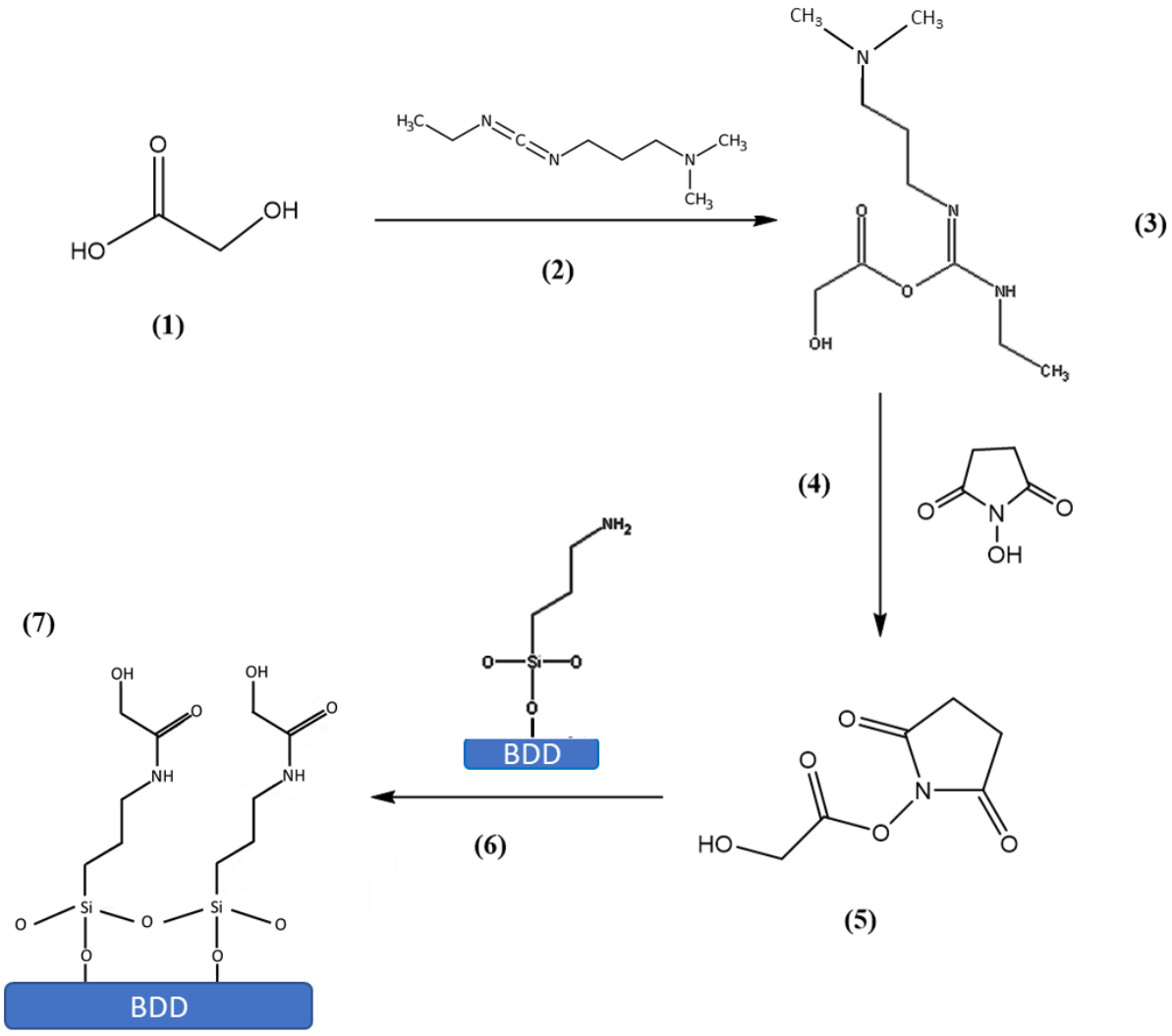

Figure B- 1. The mechanism of EDC/NHS reaction (1) glycolic acid, (2) EDC, (3) unstable reactive O-acylisourea ester, (4) NHS, (5) glycolic acid-NHS (6) APTES (7) N-propyl-2-hydroxyacetamide functional groups.

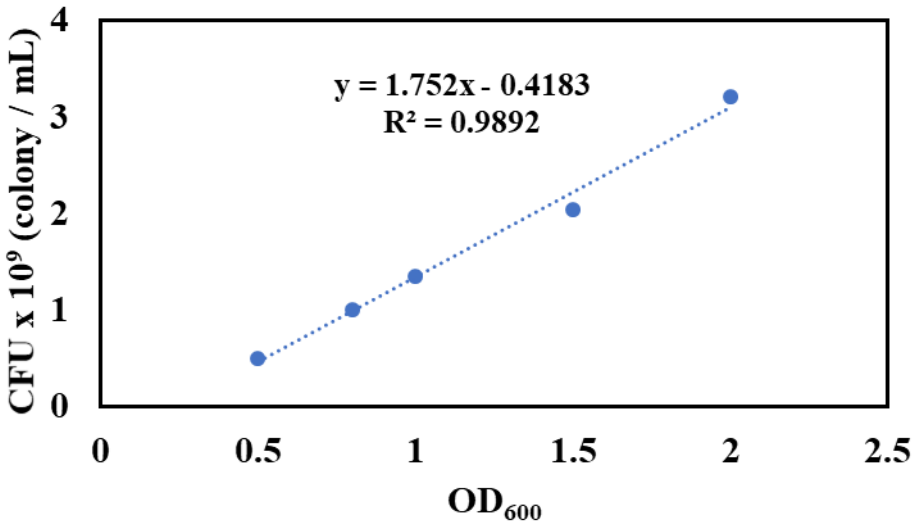

Figure B- 2. The relationship between the reading number of OD_{600} and bacteria number in 1 mL solution.

B.2 Surface modification coverage calculation

$(C:N)_{OH\text{-}BDD/OTE} = (1\text{-}X)\ (C:N)_{BDD/OTE} + X(C:N)_{APTES+GA}$

$(C:Si)_{OH\text{-}BDD/OTE} = (1\text{-}X)\ (C:Si)_{BDD/OTE} + X(C:Si)_{APTES+GA}$

Definition :

$(C:Si)_{OH\text{-}BDD/OTE}$: The Carbon and Silicon ratio on the OH-BDD/OTE based on XPS results.

$(C:Si)_{BDD/OTE}$: The Carbon and Silicon ratio on the BDD/OTE based on XPS results.

$(C:Si)_{APTES+GA:}$ The Carbon and Silicon ratio based on the chemical structure on the BDD/OTE.

For example:

Assuming one APTES compound binds with one -OH group on the BDD. Therefore, the C/Si ratio for $(C:Si)_{APTES+GA}$ is 3. The C/Si ratio on BDD/OTE and OH/BDD-OTE were measured as 64.5

and 17.4, respectively. The equation can be written as 64.5(1-X)+3X = 17.4 and the coverage can be calculated from X.

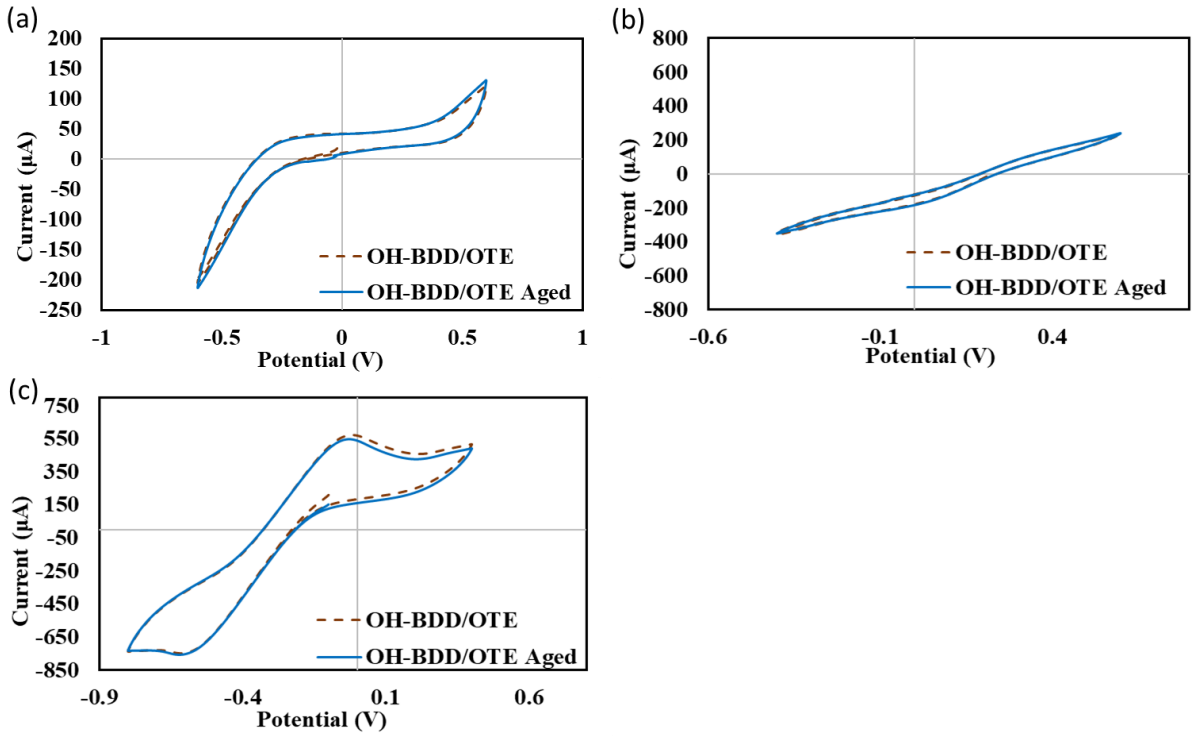

Figure B- 3. Cyclic voltammogram (CV) curves of bare BDD/OTE and OH-BDD/OTE in the (a) phosphate buffer solution (PBS) (b) PBS containing 5 mM $K_3Fe(CN)_6/K_4Fe(CN)_6$ and (c) PBS containing 5mM $Ru(NH_3)_6Cl_3/Ru(NH_3)_6Cl_2$ before and after aged. (V vs Ag/AgCl)

B.3 Titration and data analysis

Titration was applied to determine the pKa values and proton binding site concentrations (N_d) on the bacteria cell surface. The bacteria solution was place in the sealed vessel and purged with N_2 for 30 minutes before titration. The titration solution, 0.1 N NaOH was also degassed for 30 minutes before using. Approximately 4×10^{12} bacteria cells/mL was exposed in the 20 mL 0.1 M NaCl, which was adjusted to pH 2.0 by 0.1 N HCl. The titrations were conducted in the pH

range of 2.0 to 11.0 by using an auto-titrator, and a minimum of three titrations were carried out for each experiment.

The pKa values and their corresponding proton binding sites on the bacterial cell surface were determined by fitting the pK_{a_n} and ST_n values into the charge balance equation (A3) using solver in Excel (**Figure B-4**).

$$V_{\mathrm{NaOH}} = \frac{V_0}{C} \times \{\{\sum_1^n ST_n \times 10^{-pKa_n} \times \left[\left(\frac{1}{[H^+]+10^{-pKa_n}}\right) - \left(\frac{1}{[H_0^+]+10^{-pKa_n}}\right)\right]\} - ([H^+] - \frac{K_W}{[H^+]} - [H_0^+] + \frac{K_W}{[H_0^+]})\} \quad \text{(B1)}$$

where

V_{NaOH} = calculated volume of 0.1 N NaOH added in mL

K_w = water dissociation constant (1×10^{-14});

$V_0 = \text{Initial solution volume before titration (L)}; \mathrm{C} = \text{concentation of NaOH (N)};$

$ST_n = Fitting\ parameter\ of\ POA1\ site\ concentration\ (M)$;

$[H^+] = 10^{-PH}; [H_0^+] = initial\ 10^{-pH_0}; n = 4; pKa_n = dissociation\ constant;$

N_{a_i} = site numbers per unit area (#/nm^2), which was calculated according to ($\frac{ST_n}{Total\ cell\ number} \times Avogadro's\ number \times \frac{1}{cell\ surface\ area}$). The total cell number was determined by OD_{600} calibration. The surface area per cell obtained from the measured cell size and the ratio of cell numbers to dry mass were 6.77 μm^2/cell and 7.02×10^{-12} g/cell for POA1, respectively.

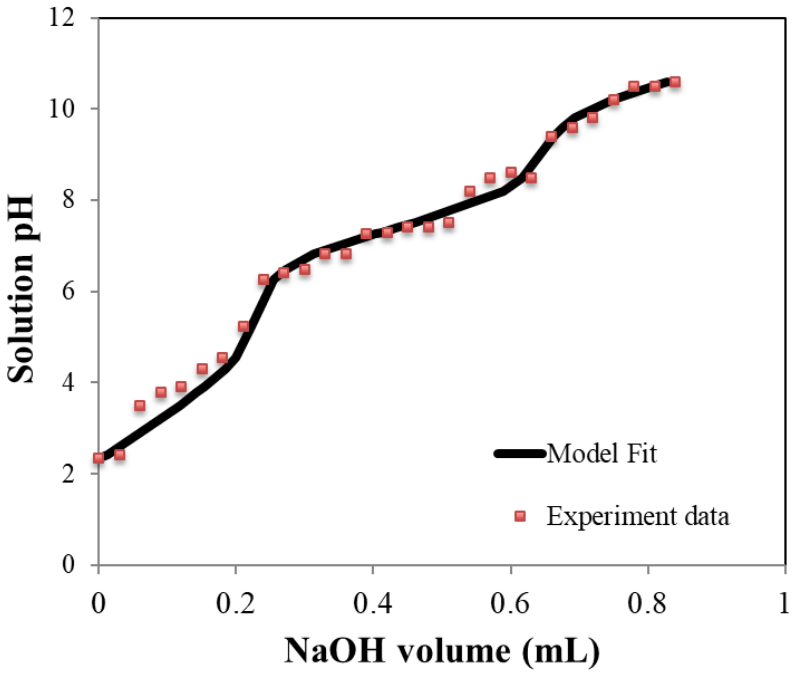

Figure B- 4. The relationship between solution pH and addition of 0.1 N NaOH volume for POA1 with experiment data and model fitting results.

Appendix C

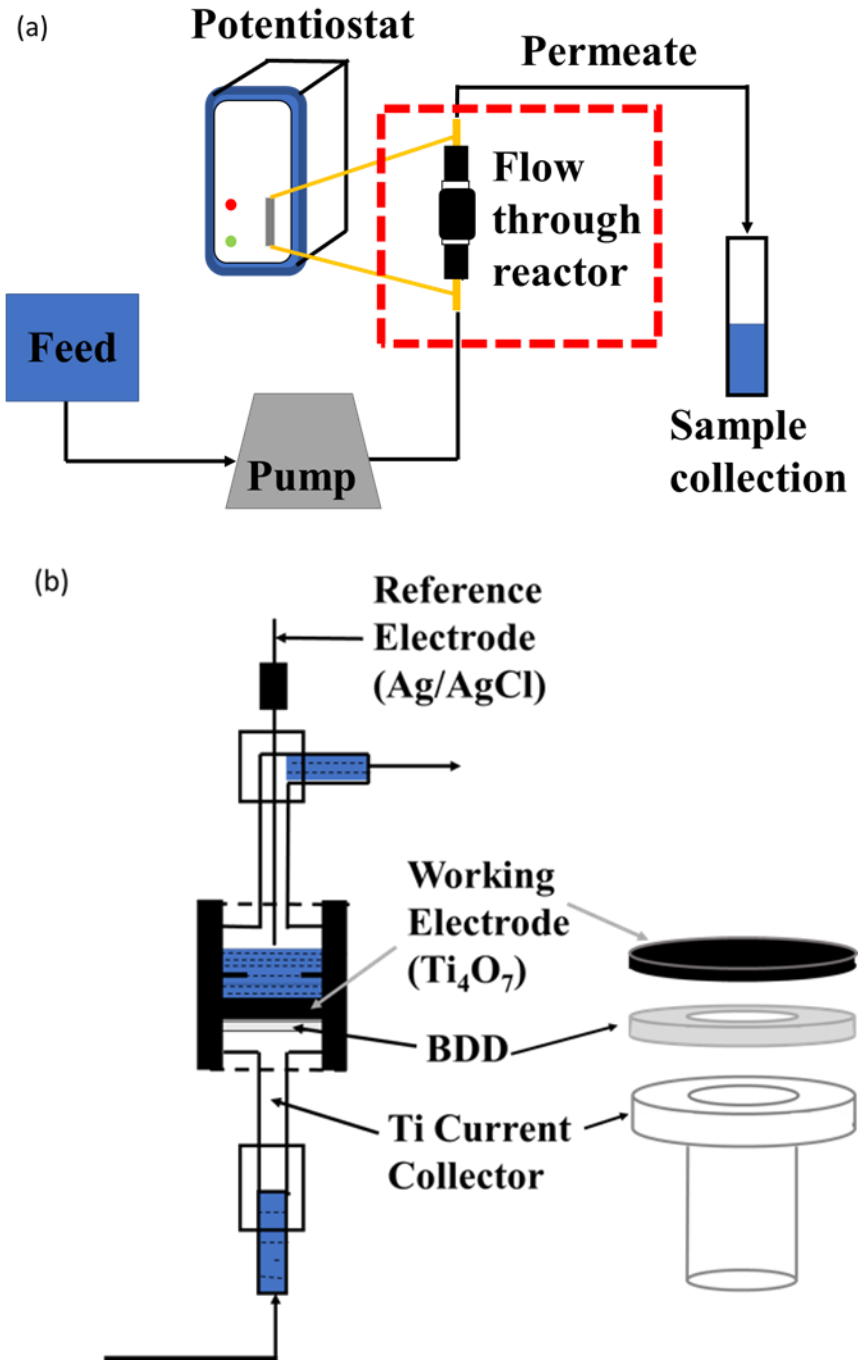

Figure C- 1. (a) The electrochemical oxidation experiment setup and (b) the details of the flow through reactor.

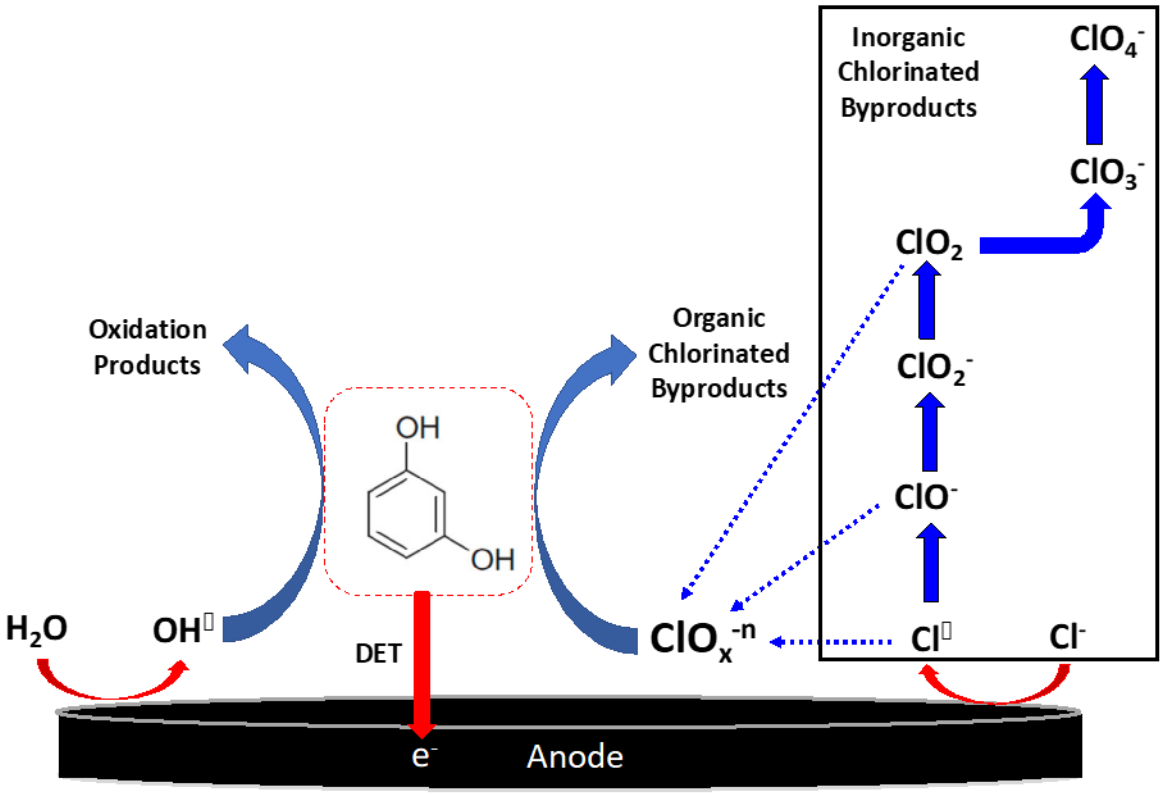

Figure C- 2. Scheme showing general pathways for resorcinol oxidation and chlorinated byproduct formation. DET = direct electron transfer.

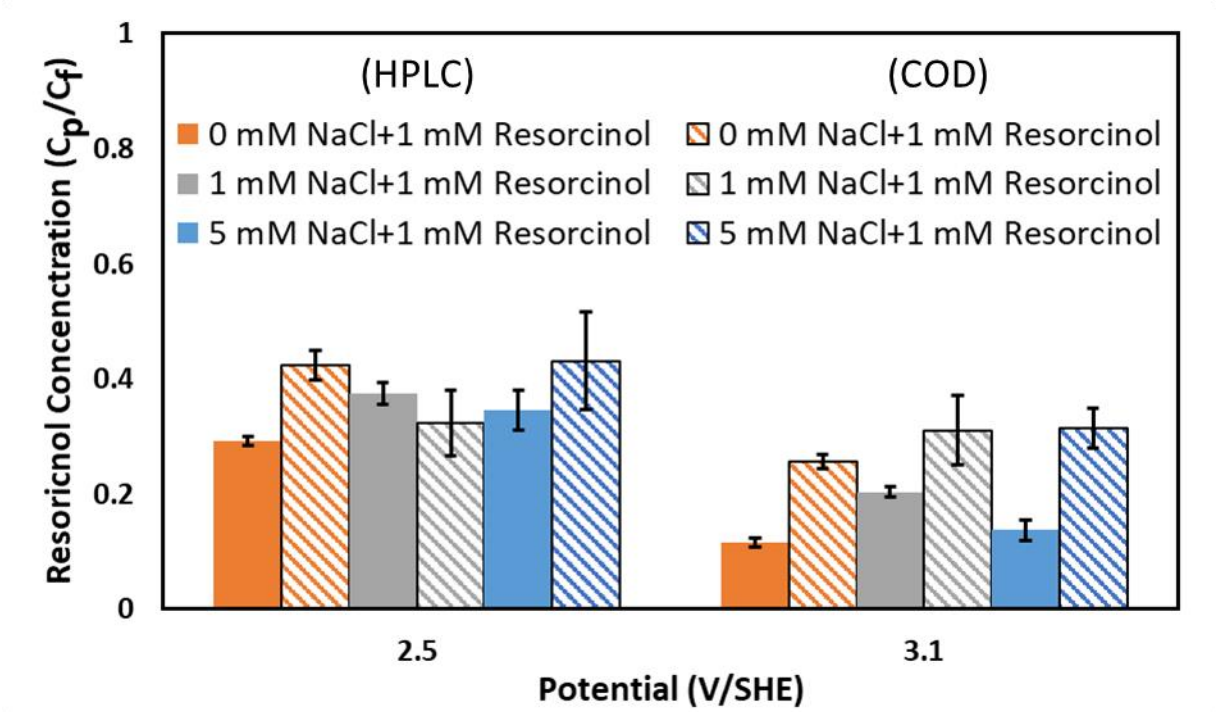

Figure C- 3. Electro-oxidation experiments mixing 1 or 5 mM of NaCl and 1 mM resorcinol. (a) Resorcinol concentration profiles measured by HPLC (solid) and COD concentration measurement (striped). All the results were analyzed from the quenching permeate solutions after electrooxidation process.

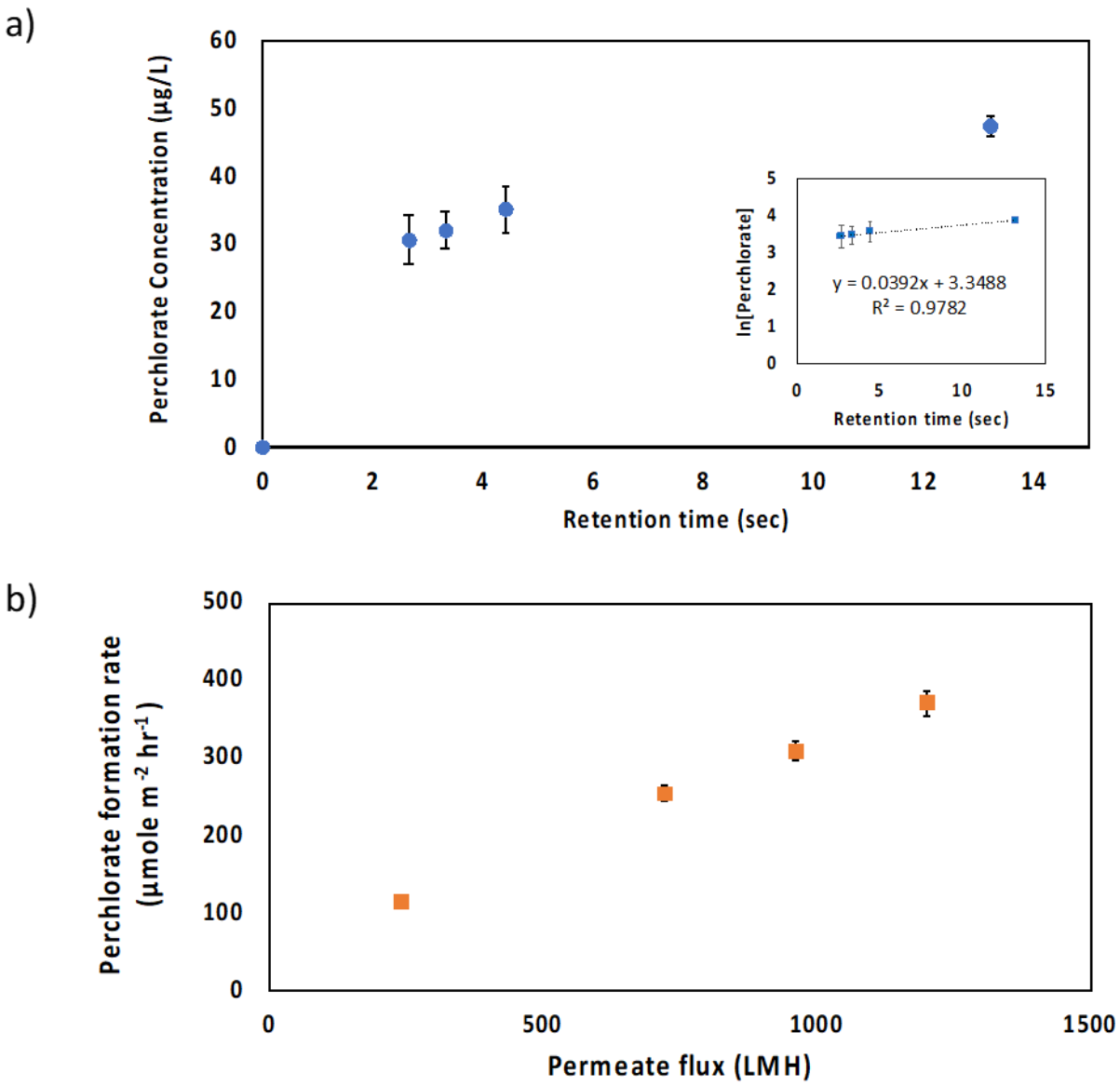

Figure C- 4. (a) Perchlorate formation kinetic fitting from 1 mM chlorate at an anode potential of 3.0 V/SHE with different retention time (inset shows calculation of first-order rate constant of 0.04 s^{-1}). (b) Perchlorate formation rates from 1 mM chlorate on the Ti_4O_7 electrode with different flow rates.

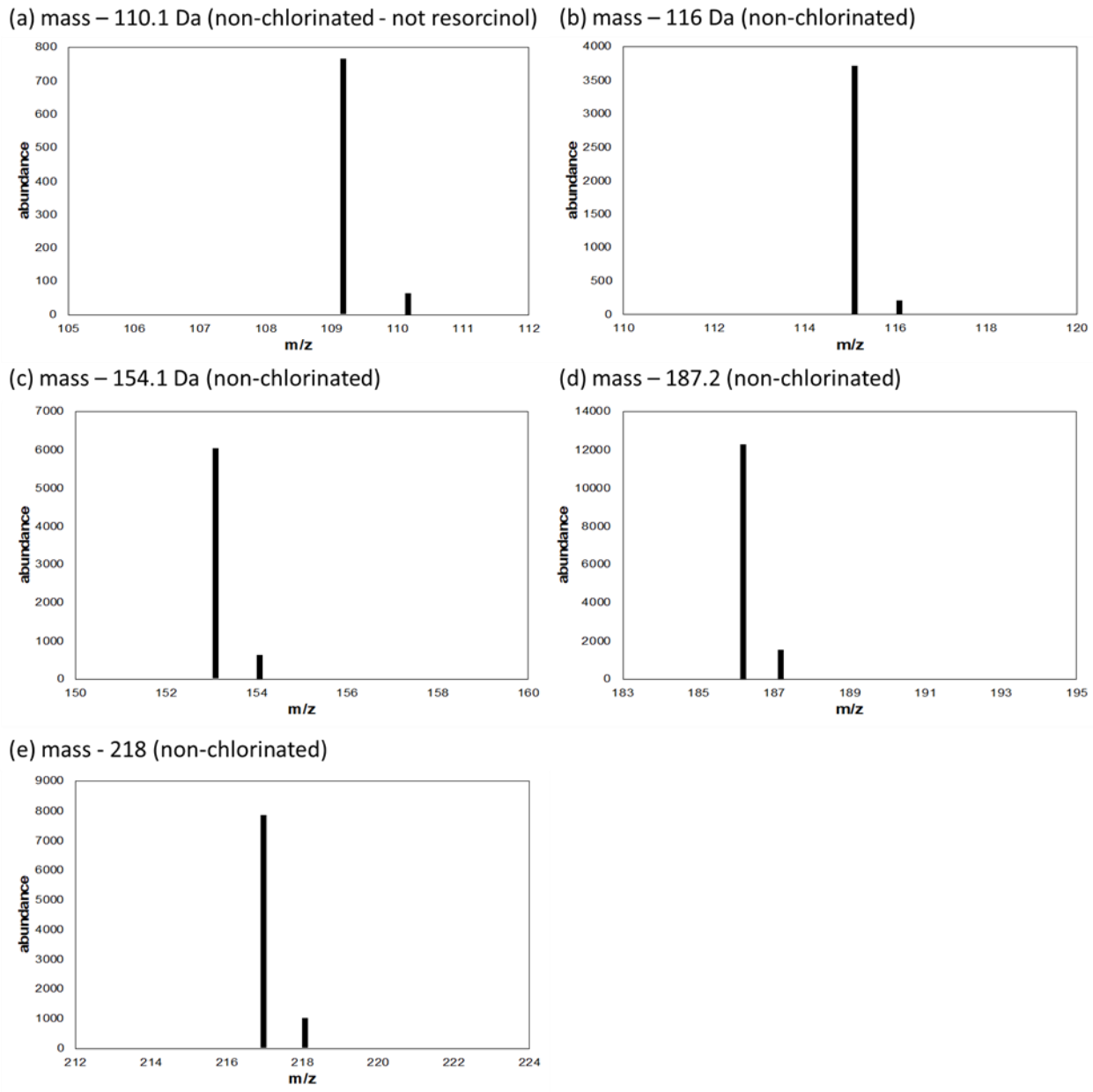

Figure C- 5. The raw LC-MS data for non-chlorinated products with mass (a) 110.1 Da, (b) 116 Da, (c) 154.1 Da, (d) 187.2 Da and (e) 218 Da. The mass of one proton (1 Da) was added to all compounds.

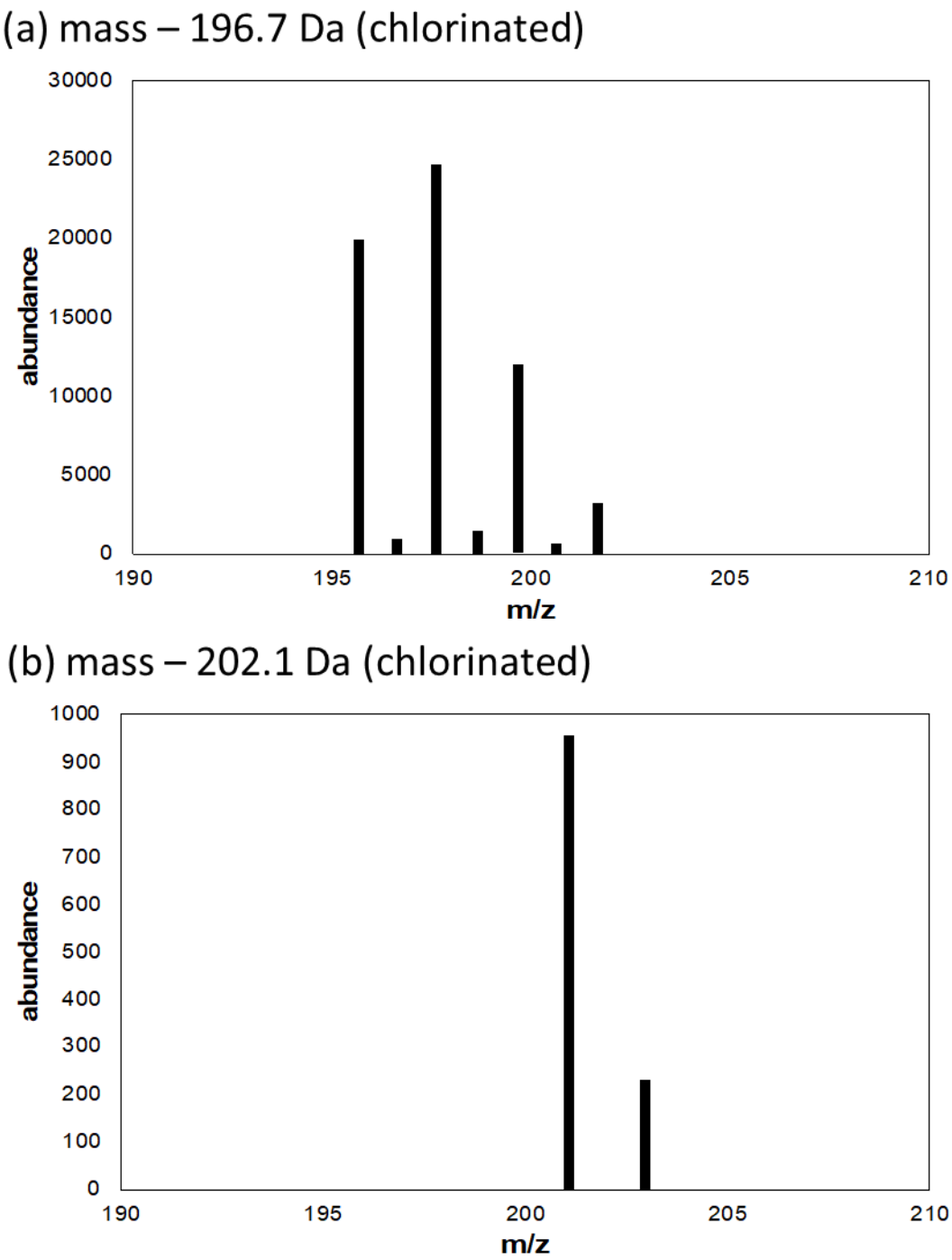

Figure C- 6. The raw LC-MS data for chlorinated products with mass (a) 196.7 Da and (b) 202.1 Da. The mass of one proton (1 Da) was added to all compounds

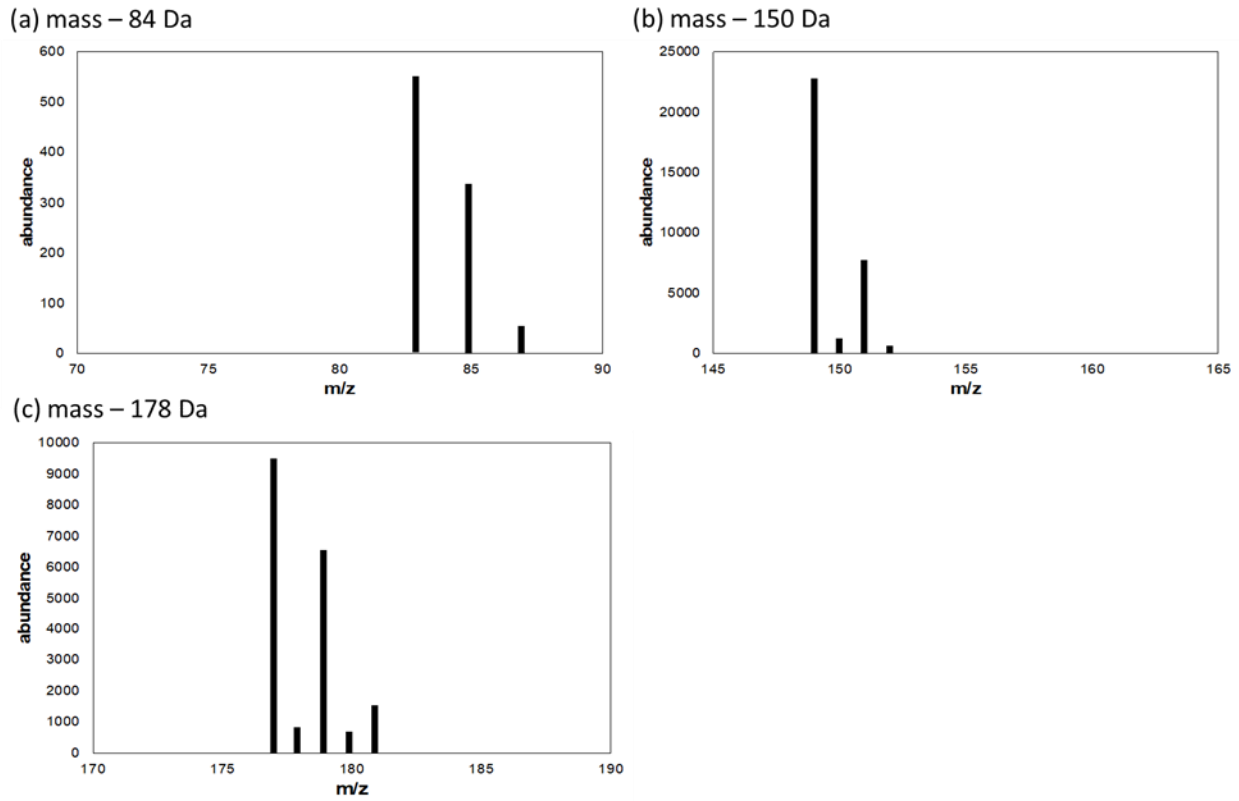

Figure C- 7. The raw LC-MS data for chlorinated products from 1 mM NaOCl/1 mM resorcinol solution with mass (a) 84 Da, (b) 150 Da and (c) 178 Da. The mass of one proton (1 Da) was added to all compounds.

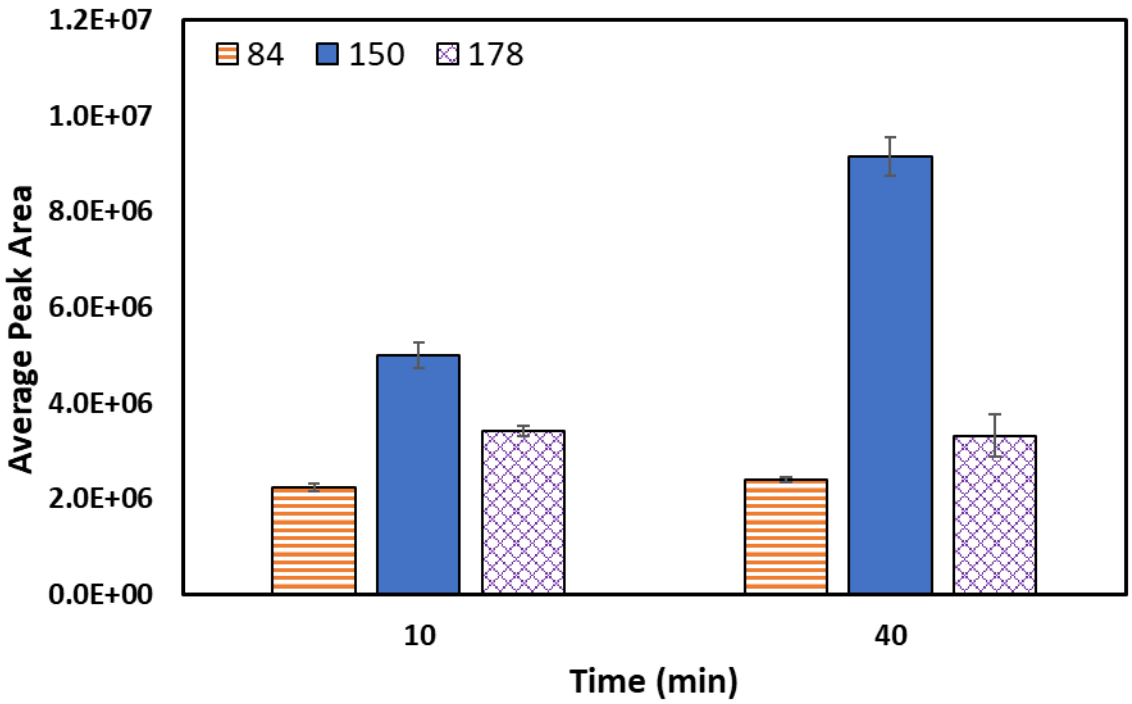

Figure C- 8. Average peak area of chlorinated byproducts from 1 mM resorcinol containing 1 mM NaOCl under batch conditions.

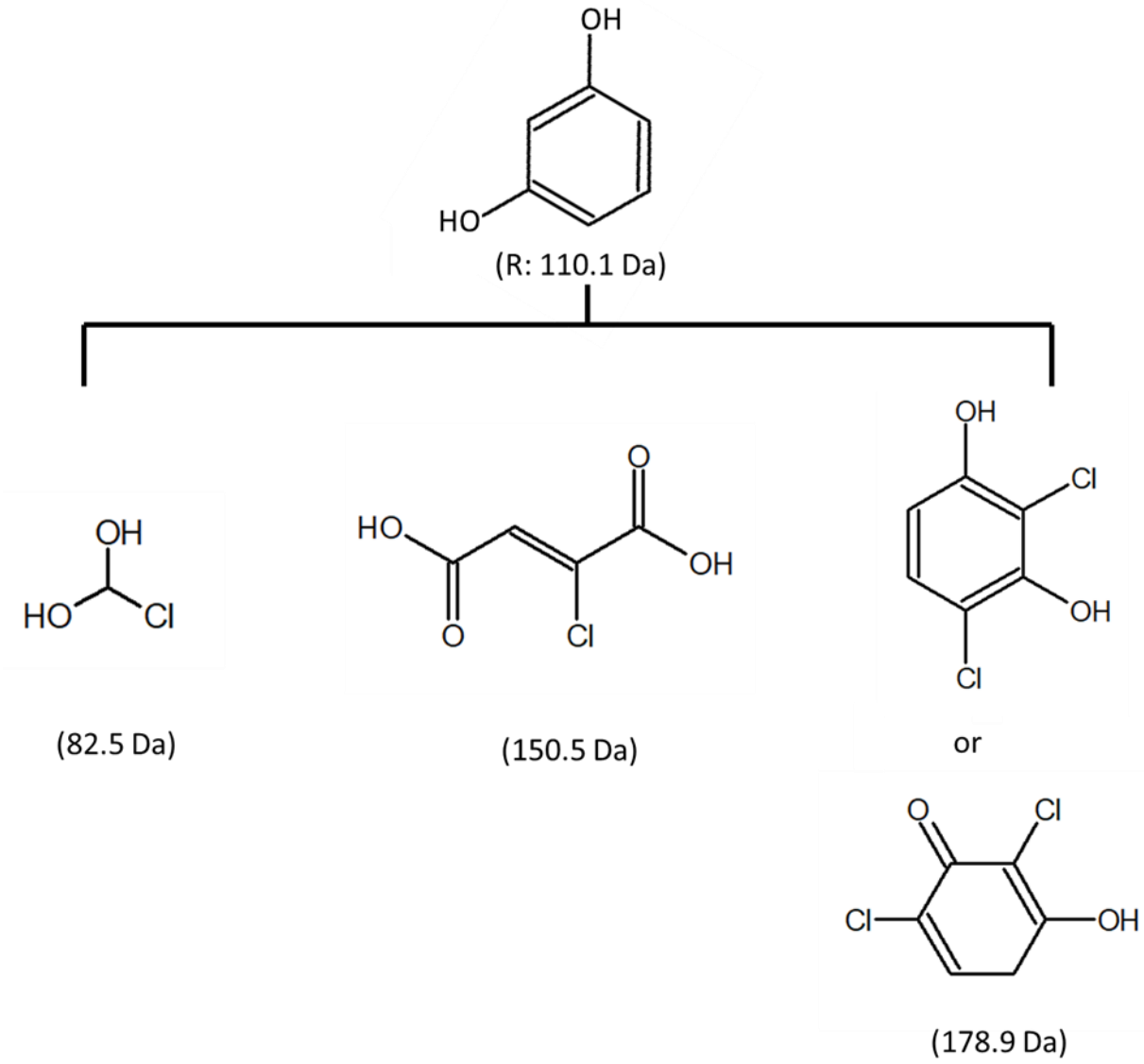

Figure C- 9. Proposed chlorinated production from the reaction between resorcinol and NaOCl under batch condition with 1 mM NaOCl/1 mM resorcinol solution at pH = 8.7.

Table C- 1. Masses of the detected and proposed organic compounds from the reaction between resorcinol and NaCl (1mM and 5 mM) under anodic potentials 2.5 and 3.1 V/SHE

#	Detected mass (Da)	Proposed mass (Da)
1	110.1 (not resorcinol)	110.1
2	116	116.1
3	154.1	154.1
4	187.2	188.2
5	218	218

Masses of the detected and proposed compounds from the reaction between resorcinol and NaOCl under batch condition with 1 mM NaOCl/1 mM resorcinol solution at pH = 8.7

#	Detected mass (Da)	Proposed mass (Da)
1	84	82.5
2	150	150.5
3	178	178.9

Masses of the detected and proposed chlorinated compounds from the reaction between resorcinol and NaCl (1mM and 5 mM) under anodic potentials 2.5 and 3.1 V/SHE.

#	Detected mass (Da)	Proposed mass (Da)
1	196.7	195.9
2	202.1	202.1

(a)

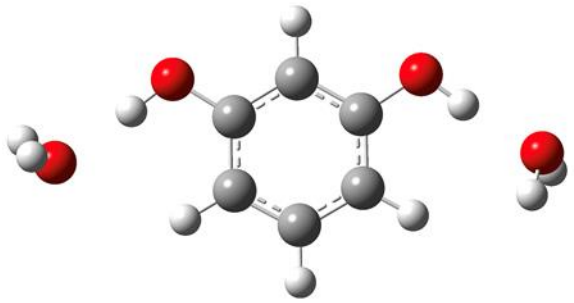

(b)

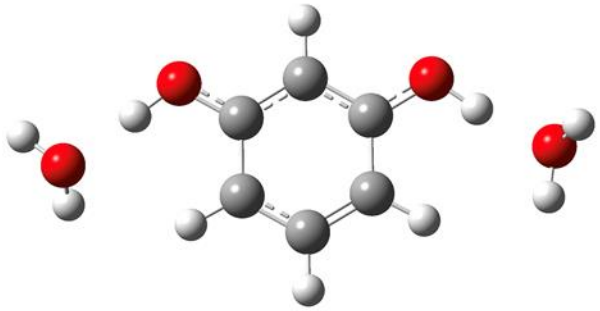

Figure C- 10. Geometric optimized structures from DFT calculations of: (a) Resorcinol + $2H_2O$ and (b) $[\text{Resorcinol} + 2H_2O]^+$. Atom Key: C = grey; O = red; H = white.

Appendix E

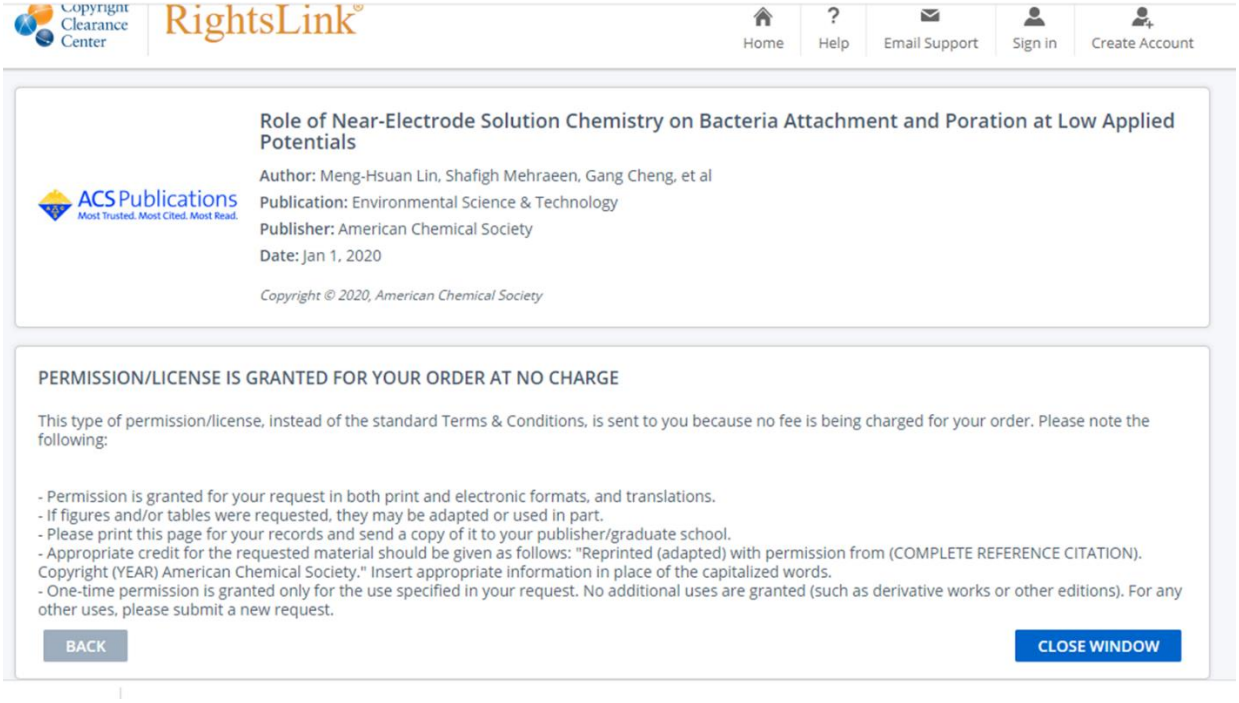

Copyright Clearance Center | RightsLink®

Home | Help | Email Support | Sign in | Create Account

Role of Near-Electrode Solution Chemistry on Bacteria Attachment and Poration at Low Applied Potentials

ACS Publications
Most Trusted. Most Cited. Most Read.

Author: Meng-Hsuan Lin, Shafigh Mehraeen, Gang Cheng, et al
Publication: Environmental Science & Technology
Publisher: American Chemical Society
Date: Jan 1, 2020

Copyright © 2020, American Chemical Society

PERMISSION/LICENSE IS GRANTED FOR YOUR ORDER AT NO CHARGE

This type of permission/license, instead of the standard Terms & Conditions, is sent to you because no fee is being charged for your order. Please note the following:

- Permission is granted for your request in both print and electronic formats, and translations.
- If figures and/or tables were requested, they may be adapted or used in part.
- Please print this page for your records and send a copy of it to your publisher/graduate school.
- Appropriate credit for the requested material should be given as follows: "Reprinted (adapted) with permission from (COMPLETE REFERENCE CITATION). Copyright (YEAR) American Chemical Society." Insert appropriate information in place of the capitalized words.
- One-time permission is granted only for the use specified in your request. No additional uses are granted (such as derivative works or other editions). For any other uses, please submit a new request.

BACK | CLOSE WINDOW

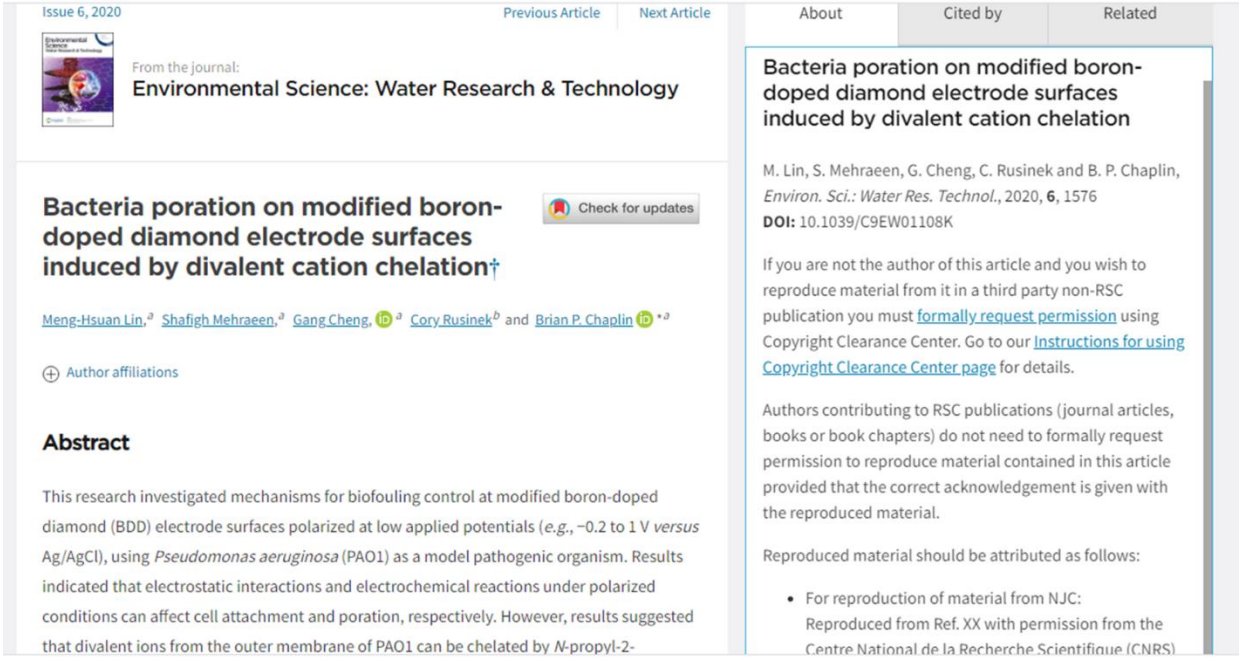

Issue 6, 2020 | Previous Article | Next Article

From the journal:
Environmental Science: Water Research & Technology

Bacteria poration on modified boron-doped diamond electrode surfaces induced by divalent cation chelation†

Check for updates

Meng-Hsuan Lin,[a] Shafigh Mehraeen,[a] Gang Cheng,[a] Cory Rusinek[b] and Brian P. Chaplin[*a]

Author affiliations

Abstract

This research investigated mechanisms for biofouling control at modified boron-doped diamond (BDD) electrode surfaces polarized at low applied potentials (*e.g.*, −0.2 to 1 V *versus* Ag/AgCl), using *Pseudomonas aeruginosa* (PAO1) as a model pathogenic organism. Results indicated that electrostatic interactions and electrochemical reactions under polarized conditions can affect cell attachment and poration, respectively. However, results suggested that divalent ions from the outer membrane of PAO1 can be chelated by *N*-propyl-2-

About | Cited by | Related

Bacteria poration on modified boron-doped diamond electrode surfaces induced by divalent cation chelation

M. Lin, S. Mehraeen, G. Cheng, C. Rusinek and B. P. Chaplin, *Environ. Sci.: Water Res. Technol.*, 2020, **6**, 1576
DOI: 10.1039/C9EW01108K

If you are not the author of this article and you wish to reproduce material from it in a third party non-RSC publication you must formally request permission using Copyright Clearance Center. Go to our Instructions for using Copyright Clearance Center page for details.

Authors contributing to RSC publications (journal articles, books or book chapters) do not need to formally request permission to reproduce material contained in this article provided that the correct acknowledgement is given with the reproduced material.

Reproduced material should be attributed as follows:

- For reproduction of material from NJC:
  Reproduced from Ref. XX with permission from the Centre National de la Recherche Scientifique (CNRS)

References

[1] T. R. Garrett, M. Bhakoo, and Z. Zhang, "Bacterial Adhesion and Biofilms on Surfaces," *Prog. Nat. Sci.*, vol. 18, no. 9, pp. 1049–1056, 2008.

[2] M. Cloutier, D. Mantovani, and F. Rosei, "Antibacterial Coatings: Challenges, Perspectives, and Opportunities," *Trends Biotechnol.*, vol. 33, no. 11, pp. 637–652, 2015.

[3] C. Liu *et al.*, "Conducting Nanosponge Electroporation for Affordable and High-Efficiency Disinfection of Bacteria and Viruses in Water," *Nano Lett.*, vol. 13, no. 9, pp. 4288–4293, 2013.

[4] H. H. Tuson and D. B. Weibel, "Bacteria-Surface Interactions.," *Soft Matter*, vol. 9, no. 18, pp. 4368–4380, 2013.

[5] M. Katsikogianni and Y. F. Missirlis, "Concise Review of Mechanisms of Bacterial Adhesion to Biomaterials and of Techniques Used in Estimating Bacteria-Material Interactions," *Eur. Cells Mater.*, vol. 8, pp. 37–57, 2004.

[6] A. Héquet, V. Humblot, J. M. Berjeaud, and C. M. Pradier, "Optimized Grafting of Antimicrobial Peptides on Stainless Steel Surface and Biofilm Resistance Tests," *Colloids Surfaces B Biointerfaces*, vol. 84, no. 2, pp. 301–309, 2011.

[7] X.-F. Sun *et al.*, "Graphene Oxide–Silver Nanoparticle Membrane for Biofouling Control and Water Purification," *Chem. Eng. J.*, vol. 281, no. 281, pp. 53–59, 2015.

[8] V. Kochkodan and N. Hilal, "A Comprehensive Review on Surface Modified Polymer Membranes for Biofouling Mitigation," *Desalination*, vol. 356, no. 356, pp. 187–207, 2015.

[9] D. Pavithra and M. Doble, "Biofilm Formation, Bacterial Adhesion and Host Response on Polymeric Implants--Issues and Prevention.," *Biomed. Mater.*, vol. 3, no. 3, p. 034003, 2008.

[10] A. Ronen, W. Duan, I. Wheeldon, S. Walker, and D. Jassby, "Microbial Attachment

Inhibition through Low-Voltage Electrochemical Reactions on Electrically Conducting Membranes," *Environ. Sci. Technol.*, vol. 49, no. 21, pp. 12741–12750, 2015.

[11] A. T. Poortinga, J. Smit, H. C. Van Der Mei, and H. J. Busscher, "Electric Field Induced Desorption of Bacteria from a Conditioning Film Covered Substratum," *Biotechnol. Bioeng.*, vol. 76, no. 4, pp. 395–399, 2001.

[12] Z.-Y. Huo, X. Xie, T. Yu, Y. Lu, C. Feng, and H.-Y. Hu, "Nanowire-Modified Three-Dimensional Electrode Enabling Low-Voltage Electroporation for Water Disinfection," *Environ. Sci. Technol*, vol. 50, no. 14, pp. 7641–7649, 2016.

[13] A. Matilainen and M. Sillanpää, "Removal of Natural Organic Matter from Drinking Water by Advanced Oxidation Processes," *Chemosphere*, vol. 80, no. 4, pp. 351–365, 2010.

[14] C. D. Vecitis, M. H. Schnoor, M. Saifur Rahaman, J. D. Schiffman, and M. Elimelech, "Electrochemical Multiwalled Carbon Nanotube Filter for Viral and Bacterial Removal and Inactivation," *Environ. Sci. Technol*, vol. 45, pp. 3672–3679, 2011.

[15] I. Levchuk, J. J. Rueda Márquez, and M. Sillanpää, "Removal of Natural Organic Matter (NOM) from Water by Ion Exchange – A Review," *Chemosphere*, vol. 192, pp. 90–104, 2018.

[16] W. Gan, Y. Ge, H. Zhu, H. Huang, and X. Yang, "ClO_2 Pre-Oxidation Changes the Yields and Formation Pathways of Chloroform and Chloral Hydrate from Phenolic Precursors during Chlorination," *Water Res.*, vol. 148, pp. 250–260, 2019.

[17] W. A. Arnold, J. Bolotin, U. von Gunten, and T. B. Hofstetter, "Evaluation of Functional Groups Responsible for Chloroform Formation during Water Chlorination Using Compound Specific Isotope Analysis," *Environ. Sci. Technol.*, vol. 42, no. 21, pp. 7778–7785, 2008.

[18] Y. H. Chuang, D. L. McCurry, H. H. Tung, and W. A. Mitch, "Formation Pathways and Trade-Offs between Haloacetamides and Haloacetaldehydes during Combined Chlorination and Chloramination of Lignin Phenols and Natural Waters," *Environ. Sci. Technol.*, vol. 49, no. 24, pp. 14432–14440, 2015.

[19] S. Lin, R. J. Llukkonen, R. E. Thom, J. G. Bastian, M. T. Lukasewycz, and R. M. Carlson, "Increased Chloroform Production from Model Components of Aquatic Humus and Mixtures of Chlorine Dioxide/Chlorine," *Environ. Sci. Technol.*, vol. 18, no. 12, pp. 932–935, 1984.

[20] D. Rana and T. Matsuura, "Surface Modifications for Antifouling Membranes," *Chem. Rev.*, vol. 110, no. 4, pp. 2448–2471, 2010.

[21] R. Slade and A. Bauen, "Micro-Algae Cultivation for Biofuels: Cost, Energy Balance, Environmental Impacts and Future Prospects," *Biomass and Bioenergy*, vol. 53, pp. 29–38, 2013.

[22] J. D. Tibocha-Bonilla, C. Zuñiga, R. D. Godoy-Silva, and K. Zengler, "Advances in Metabolic Modeling of Oleaginous Microalgae," *Biotechnol. Biofuels*, vol. 11, p. 241, 2018.

[23] L. Hua *et al.*, "Effects of anodic oxidation of a substoichiometric titanium dioxide reactive electrochemical membrane on algal cell destabilization and lipid extraction," *Bioresour. Technol.*, vol. 203, pp. 112–117, 2016.

[24] L. Hua, H. Cao, Q. Ma, X. Shi, X. Zhang, and W. Zhang, "Microalgae Filtration Using an Electrochemically Reactive Ceramic Membrane: Filtration Performances, Fouling Kinetics, and Foulant Layer Characteristics," *Environ. Sci. Technol.*, vol. 54, no. 3, pp. 2012–2021, 2020.

[25] C. T. T. Binh, C. G. Peterson, T. Tong, K. A. Gray, J. F. Gaillard, and J. J. Kelly,

"Comparing Acute Effects of A Nano-TiO_2 Pigment on Cosmopolitan Freshwater Phototrophic Microbes Using High-throughput Screening," *PLoS One*, vol. 10, no. 4, 2015.

[26] J. Mansouri, S. Harrisson, and V. Chen, "Strategies for Controlling Biofouling in Membrane Filtration Systems: Challenges and Opportunities," *J. Mater. Chem.*, vol. 20, no. 22, pp. 4567–4586, 2010.

[27] Y. Oren, "Capacitive Deionization (CDI) for Desalination and Water Treatment — Past, Present and Future (a review)," *Desalination*, vol. 228, no. 1–3, pp. 10–29, 2008.

[28] G. A. Gagnon, J. L. Rand, K. C. O'Leary, A. C. Rygel, C. Chauret, and R. C. Andrews, "Disinfectant Efficacy of Chlorite and Chlorine Dioxide in Drinking Water Biofilms," *Water Res.*, vol. 39, no. 9, pp. 1809–1817, 2005.

[29] X. Chen and P. S. Stewart, "Biofilm Removal Caused by Chemical Treatments," *Water Res.*, vol. 34, no. 17, pp. 4229–4233, 2000.

[30] I. Banerjee, R. C. Pangule, and R. S. Kane, "Antifouling Coatings: Recent Developments in the Design of Surfaces That Prevent Fouling by Proteins, Bacteria, and Marine Organisms," *Adv. Mater.*, vol. 23, no. 6, pp. 690–718, 2011.

[31] S. Shrivastava, T. Bera, A. Roy, G. Singh, P. Ramachandrarao, and D. Dash, "Characterization of Enhanced Antibacterial Effects of Novel Silver Nanoparticles," *Nanotechnology*, vol. 18, no. 22, pp. 225103–225112, 2007.

[32] Z.-Y. Huo *et al.*, "Carbon-Nanotube Sponges Enabling Highly Efficient and Reliable Cell Inactivation by Low-Voltage Electroporation," *Environ. Sci. Nano*, vol. 4, no. 10, pp. 2010–2017, 2017.

[33] S. Pandit, S. Shanbhag, M. Mauter, Y. Oren, and M. Herzberg, "The Influence of Electric Fields on Biofouling of Carbonaceous Electrodes," *Environ. Sci. Technol.*, vol. 51, no. 17,

pp. 10022–10030, 2017.

[34] S. Jain, A. Sharma, and B. Basu, “Vertical Eectric Field Induced Bacterial Growth Inactivation on Amorphous Carbon Electrodes,” *Carbon N. Y.*, vol. 81, pp. 193–202, 2015.

[35] H. Särkkä, M. Vepsäläinen, and M. Sillanpää, “Natural Organic Matter (NOM) Removal by Electrochemical Methods — A review,” *J. Electroanal. Chem.*, vol. 755, pp. 100–108, 2015.

[36] V. K. Sharma *et al.*, “Impact of Metal Ions,Metal Oxides, and Nanoparticles on the Formation of Disinfection Byproducts during Chlorination,” *Chem. Eng. J.*, vol. 317, pp. 777–792, 2017.

[37] M. Sillanpää, M. C. Ncibi, A. Matilainen, and M. Vepsäläinen, “Removal of Natural Organic Matter in Drinking Water Treatment by Coagulation: A Comprehensive Review,” *Chemosphere*, vol. 190, pp. 54–71, 2018.

[38] B. K. Mayer and D. R. Ryan, “Impact on Disinfection Byproducts Using Advanced Oxidation Processes for Drinking Water Treatment,” *Appl. ofAdvanced Oxid. Process. Drink. Water Treat.*, pp. 345–386, 2017.

[39] O. M. Cornejo, M. F. Murrieta, L. F. Castañeda, and J. L. Nava, “Characterization of the Reaction Environment in Flow Reactors Fitted with BDD Electrodes for Use in Electrochemical Advanced Oxidation Processes: A Critical Review,” *Electrochim. Acta*, vol. 331, no. 135373, pp. 1–14, 2020.

[40] A. H. Henke, T. P. Saunders, J. A. Pedersen, and R. J. Hamers, “Enhancing Electrochemical Efficiency of Hydroxyl Radical Formation on Diamond Electrodes by Functionalization with Hydrophobic Monolayers,” *Langmuir*, vol. 35, no. 6, pp. 2153–2163, 2019.

[41] P. C. S. Hayfield, *Development of a New Material- Monolithic Ti_4O_7 Ebonex® Ceramic*.

Royal Society of Chemistry, 2002.

[42] Y. Jing, S. Almassi, S. Mehraeen, R. J. LeSuer, and B. P. Chaplin, “The Roles of Oxygen Vacancies, Electrolyte Composition, Lattice Structure, and Doping Density on the Electrochemical Reactivity of Magnéli phase TiO_2 Anodes,” *J. Mater. Chem. A*, vol. 6, no. 46, pp. 23828–23839, 2018.

[43] T. X. H. Le, H. Haflich, A. D. Shah, and B. P. Chaplin, “Energy-Efficient Electrochemical Oxidation of Perfluoroalkyl Substances Using a Ti_4O_7 Reactive Electrochemical Membrane Anode,” *Environ. Sci. Technol. Lett.*, vol. 6, no. 8, pp. 504–510, 2019.

[44] L. Guo, Y. Jing, and B. P. Chaplin, “Development and Characterization of Ultrafiltration TiO2 Magnéli Phase Reactive Electrochemical Membranes,” *Environ. Sci. Technol.*, vol. 50, no. 3, pp. 1428–1436, 2016.

[45] C. A. Martínez-Huitle and E. Brillas, “Electrochemical Alternatives for Drinking Water Disinfection,” *Angew. Chemie - Int. Ed.*, vol. 47, no. 11, pp. 1998–2005, 2008.

[46] H. C. Flemming, “Biofouling in Water Systems - Cases, Causes and Countermeasures,” *Appl. Microbiol. Biotechnol.*, vol. 59, no. 6, pp. 629–640, 2002.

[47] M. Dargahi, Z. Hosseinidoust, N. Tufenkji, and S. Omanovic, “Investigating Electrochemical Removal of Bacterial Biofilms from Stainless Steel Substrates,” *Colloids Surfaces B Biointerfaces*, vol. 117, pp. 152–157, 2014.

[48] A. J. van der Borden, H. van der Werf, H. C. van der Mei, and H. J. Busscher, “Electric-Current-Induced Detachment of Staphylococcus Epidermidis Strains from Surgical Stainless Steel.,” *J. Biomed. Mater. Res. B. Appl. Biomater.*, vol. 68, no. 2, pp. 160–164, 2004.

[49] M. S. Rahaman, C. D. Vecitis, and M. Elimelech, “Electrochemical Carbon-Nanotube Filter

Performance Toward Virus Removal and Inactivation in the Presence of Natural Organic Matter," *Environ. Sci. Technol.*, vol. 46, no. 3, pp. 1556–1564, 2012.

[50] S. T. Sultana, J. T. Babauta, and H. Beyenal, "Electrochemical Biofilm Control : A Review," *Biofouling*, vol. 31, pp. 745–758, 2015.

[51] S. W. P. Wijnhoven *et al.*, "Nano-Silver – A Review of Available Data and Knowledge Gaps in Human and Environmental Risk Aassessment," *Nanotoxicology*, vol. 3, no. 2, pp. 109–138, 2009.

[52] Y. L. Ong, A. Razatos, G. Georgiou, and M. M. Sharma, "Adhesion Forces Between E. coli Bacteria and Biomaterial Surfaces," *Langmuir*, vol. 15, no. 8, pp. 2719–2725, 1999.

[53] L. Guo, K. Ding, K. Rockne, M. Duran, and B. P. Chaplin, "Bacteria Inactivation at A Sub-Stoichiometric Titanium Dioxide Reactive Electrochemical Membrane," *J. Hazard. Mater.*, vol. 319, pp. 137–146, 2016.

[54] C. Belfiore, P. Castellano, and G. Vignolo, "Reduction of Escherichia coli Population Following Treatment with Bacteriocins From Lactic Acid Bacteria and Chelators," *Food Microbiol.*, vol. 24, no. 3, pp. 223–229, 2007.

[55] E. Banin, K. M. Brady, and E. P. Greenberg, "Chelator-Induced Dispersal and Killing of Pseudomonas aeruginosa Cells in a Biofilm," *Appl. Environ. Microbiol.*, vol. 72, no. 3, pp. 2064–2069, 2006.

[56] J. M. Hamilton-Miller, "Damaging Effects of Ethylenediaminetetra-Acetate and Penicillins on Permeability Barriers in Gram-negative Bacteria.," *Biochem. J.*, vol. 100, no. 3, pp. 675–82, 1966.

[57] M. A. Asbell and R. G. Eagon, "Role of Multivalent Cations in the Organization, Structure, and Assembly of the Cell Wall of Pseudomonas aeruginosa," *J. Bacteriol.*, vol. 92, no. 2,

pp. 380–387, 1966.

[58] R. E. Wooley and M. S. Jones, “Action of EDTA-Tris and Antimicrobial Agent Combinations on Selected Pathogenic Bacteria,” *Vet. Microbiol.*, vol. 8, no. 3, pp. 271–280, 1983.

[59] S. M. M. Kabir and J. Koh, “Effect of Chelating Agent in Disperse Dye Dyeing on Polyester Fabric,” *Fibers Polym.*, vol. 18, no. 12, pp. 2315–2321, 2017.

[60] S. K. Jeong, J. Y. Ko, J. T. Seo, S. K. Ahn, C. W. Lee, and S. H. Lee, “Stimulation of Epidermal Calcium Gradient Loss and Increase in TNF-α and IL-1α Expressions by Glycolic Acid in Murine Epidermis,” *Exp. Dermatol.*, vol. 14, no. 8, pp. 571–579, 2005.

[61] J. Liedtka, “Glycolic Acid Pharmacy Compounding Advisory Committee Meeting,” 2016.

[62] A. W. Zularisam, A. F. Ismail, and R. Salim, “Behaviours of Natural Organic Matter in Membrane Filtration for Surface Water Treatment — A Review,” *Desalination*, vol. 194, no. 1–3, pp. 211–231, 2006.

[63] Environmental Protection Agency (EPA), “The Third Unregulated Contaminant Monitoring Rule (UCMR 3): Data Summary,” 2017.

[64] B. P. Chaplin, “Critical Review of Electrochemical Advanced Oxidation Processes for Water Treatment Applications,” *Environ. Sci. Process. Impacts*, vol. 16, no. 6, pp. 1182–1203, 2014.

[65] A. Y. Bagastyo, D. J. Batstone, I. Kristiana, B. I. Escher, C. Joll, and J. Radjenovic, “Electrochemical Treatment of Reverse Osmosis Concentrate on Boron-Doped Electrodes in Undivided and Divided Cell Configurations,” *J. Hazard. Mater.*, vol. 279, pp. 111–116, 2014.

[66] Á. Anglada, A. Urtiaga, I. Ortiz, D. Mantzavinos, and E. Diamadopoulos, “Boron-doped

Diamond Anodic Treatment of Landfill Leachate: Evaluation of Operating Variables and Formation of Oxidation By-products," *Water Res.*, vol. 45, no. 2, pp. 828–838, 2011.

[67] J. Boudreau, D. Bejan, and N. J. Bunce, "Competition Between Electrochemical Advanced Oxidation and Electrochemical Hypochlorination of Acetaminophen at Boron-Doped Diamond and Ruthenium Dioxide Based Anodes," *Can. J. Chem.*, vol. 88, no. 5, pp. 418–425, 2010.

[68] M. E. H. Bergmann, J. Rollin, and T. Iourtchouk, "The Occurrence of Perchlorate during Drinking Water Electrolysis using BDD Anodes," *Electrochim. Acta*, vol. 54, no. 7, pp. 2102–2107, 2009.

[69] O. Azizi, D. Hubler, G. Schrader, J. Farrell, and B. P. Chaplin, "Mechanism of Perchlorate Formation on Boron-Doped Diamond Film Anodes," *Environ. Sci. Technol*, vol. 45, pp. 10582–10590, 2011.

[70] D. K. Hubler, J. C. Baygents, B. P. Chaplin, and J. Farrell, "Understanding Chlorite and Chlorate Formation Associated with Hypochlorite Generation at Boron Doped Diamond Film Anodes," *J. Electrochem. Soc.*, vol. 161, no. 12, pp. E182–E189, 2014.

[71] P. C. Singer, "Control of Disinfection By-Products in Drinking Water," *J. Environ. Eng.*, vol. 120, no. 4, pp. 727–744, Jul. 1994.

[72] A. Florentin, A. Hautemanière, and P. Hartemann, "Health Effects of Disinfection By-Products in Chlorinated Swimming Pools," *Int. J. Hyg. Environ. Health*, vol. 214, no. 6, pp. 461–469, 2011.

[73] Y. Yu, F. Zuo, and C.-Z. Li, "The Peak Effect of the Photocurrent on the Concentration of Electron Mediator (Para-Benzoquinone) in Thylakoids," *Electrochim. Acta*, vol. 113, pp. 603–608, 2013.

[74] E. E.-D. M. El-Giar and D. O. Wipf, “Microparticle-Based Iridium Oxide Ultramicroelectrodes for pH Sensing and Imaging,” *J. Electroanal. Chem.*, vol. 609, no. 2, pp. 147–154, 2007.

[75] D. O. Wipf, F. Ge, T. W. Spaine, and J. E. Baur, “Microscopic Measurement of pH with Iridium Oxide Microelectrodes,” *Anal. Chem.*, vol. 72, no. 20, pp. 4921–4927, Oct. 2000.

[76] A. Fog and R. Buck, “Electronic Semiconducting Oxides as pH Sensors,” *Sensors and Actuators*, vol. 5, pp. 137–146, 1984.

[77] C. Cai, B. Liu, M. V Mirkin, H. A. Frank, and J. F. Rusling, “Scanning Electrochemical Microscopy of Living Cells. 3. Rhodobacter sphaeroides,” *Anal. Chem*, vol. 74, pp. 114–119, 2002.

[78] T. Yasukawa, I. Uchida, and T. Matsue, “Microamperometric Measurements of Photosynthetic Activity in a Single Algal Protoplast,” *Biophys. J.*, vol. 76, pp. 1129–1135, 1999.

[79] G. Longatte *et al.*, “Evaluation of Photosynthetic Electrons Derivation by Exogenous Redox Mediators,” *Biophys. Chem.*, vol. 205, pp. 1–8, 2015.

[80] Y. Li, X. Ning, Q. Ma, D. Qin, and X. Lu, “Recent Advances in Electrochemistry by Scanning Electrochemical Microscopy,” *TrAC Trends Anal. Chem.*, vol. 80, pp. 242–254, 2016.

[81] S. Bergner, P. Vatsyayan, and F.-M. Matysik, “Recent Advances in High Resolution Scanning Electrochemical Microscopy of Living Cells – A Review,” *Anal. Chim. Acta*, vol. 775, pp. 1–13, 2013.

[82] W. S. Roberts, D. J. Lonsdale, J. Griffiths, and S. P. J. Higson, “Advances in the Application of Scanning Electrochemical Microscopy to Bioanalytical Systems,” *Biosens. Bioelectron.*,

vol. 23, no. 3, pp. 301–318, 2007.

[83] S. A. Amemiya Jidong Guo Hui Xiong Darrick Gross, "Biological Applications of Scanning Electrochemical Microscopy: Chemical Imaging of Single Living Cells and Beyond," *Anal Bioanal Chem*, vol. 386, pp. 458–471, 2006.

[84] Z.-Q. Liu, A. D. Shah, E. Salhi, J. Bolotin, and U. von Gunten, "Formation of Brominated Trihalomethanes during Chlorination or Ozonation of Natural Organic Matter Extracts and Model Compounds in Saline Water," *Water Res.*, vol. 143, pp. 492–502, 2018.

[85] C. S. Santos, A. S. Lima, D. Battistel, S. Daniele, and M. Bertotti, "Fabrication and Use of Dual-function Iridium Oxide Coated Gold SECM Tips. An Application to pH Monitoring above a Copper Electrode Surface during Nitrate Reduction," *Electroanalysis*, vol. 28, pp. 1441–1447, 2016.

[86] J. O. Park, C. Paik, and R. C. Alkire, "Scanning Microsensors for Measurement of Local pH Distributions at the Microscale," *J. Electrochem. Soc.*, vol. 143, no. 8, p. L174, 1996.

[87] S. Bause *et al.*, "Development of An Iridium-based pH Sensor for Bioanalytical Applications," *J Solid State Electrochem*, vol. 22, pp. 51–60, 2018.

[88] A. J. Bard, X. Li, and W. Zhan, "Chemically Imaging Living Cells by Scanning Electrochemical Microscopy," *Biosens. Bioelectron.*, vol. 22, no. 4, pp. 461–472, 2006.

[89] H. Shiku *et al.*, "Oxygen Consumption of Single Bovine Embryos Probed by Scanning Electrochemical Microscopy," *Anal. Chem*, vol. 73, pp. 3751–3758, 2001.

[90] E. Abucayon *et al.*, "Investigating Catalase Activity Through Hydrogen Peroxide Decomposition by Bacteria Biofilms in Real Time Using Scanning Electrochemical Microscopy," *Anal. Chem*, vol. 86, pp. 498–505, 2014.

[91] F. Turcu, A. Schulte, G. Hartwich, and W. Schuhmann, "Label-Free Electrochemical

Recognition of DNA Hybridization by Means of Modulation of the Feedback Current in SECM," *Angew. Chemie Int. Ed.*, vol. 43, no. 26, pp. 3482–3485, 2004.

[92] S. Srivastava and A. Bhargava, "Biofilms and Human Health," *Biotechnol. Lett.*, vol. 38, no. 1, pp. 1–22, 2016.

[93] T. Pradeep and Anshup, "Noble Metal Nanoparticles for Water Purification: A Critical Review," *Thin Solid Films*, vol. 517, no. 24, pp. 6441–6478, 2009.

[94] A. Ronen, W. Duan, I. Wheeldon, S. Walker, and D. Jassby, "Microbial Attachment Inhibition through Low-Voltage Electrochemical Reactions on Electrically Conducting Membranes," *Environ. Sci. Technol.*, vol. 49, no. 21, pp. 12741–12750, 2015.

[95] G. Pankratova and L. Gorton, "Electrochemical Communication between Living Cells and Conductive Surfaces," *Curr. Opin. Electrochem.*, vol. 5, no. 1, pp. 193–202, 2017.

[96] C. Bruguera-Casamada, I. Sirés, E. Brillas, and R. M. Araujo, "Effect of Electrogenerated Hydroxyl Radicals, Active Chlorine and Organic Matter on the Electrochemical Inactivation of Pseudomonas aeruginosa using BDD and Dimensionally Stable Anodes," *Sep. Purif. Technol.*, vol. 178, pp. 224–231, May 2017.

[97] G. Cheng, Z. Zhang, S. Chen, J. D. Bryers, and S. Jiang, "Inhibition of Bacterial Adhesion and Biofilm Formation on Zwitterionic Surfaces," *Biomaterials*, vol. 28, no. 29, pp. 4192–4199, 2007.

[98] C. A. Rusinek, M. F. Becker, R. Rechenberg, and T. Schuelke, "Fabrication and Characterization of Boron Doped Diamond Microelectrode Arrays of Varied Geometry," *Electrochem. commun.*, vol. 73, pp. 10–14, 2016.

[99] P. Gayen and B. P. Chaplin, "Selective Electrochemical Detection of Ciprofloxacin with a Porous Nafion/Multiwalled Carbon Nanotube Composite Film Electrode," *ACS Appl.*

Mater. Interfaces, vol. 8, pp. 1615–1626, 2016.

[100] J. R. Wayment and J. M. Harris, "Controlling Binding Site Densities on Glass Surfaces," *Anal. Chem.*, vol. 78, no. 22, pp. 7841–7849, 2006.

[101] A. Alghunaim, E. T. Brink, E. Y. Newby, and B. Zhang Newby, "Retention of poly(N-isopropylacrylamide) on 3-aminopropyltriethoxysilane," *Biointerphases*, vol. 12, no. 02C405, pp. 1–9, 2017.

[102] A. F. Stalder, G. Kulik, D. Sage, L. Barbieri, and P. Hoffmann, "A Snake-based Approach to Accurate Determination of both Contact Points and Contact Angles," *Colloids Surfaces A Physicochem. Eng. Asp.*, vol. 286, no. 1–3, pp. 92–103, 2006.

[103] A.-G. Rincón and C. Pulgarin, "Effect of pH, Inorganic Ions, Organic Matter and H_2O_2 on E. coli K12 Photocatalytic Inactivation by TiO_2 Implications in Solar Water Disinfection," *Appl. Catal. B Environ.*, vol. 51, pp. 283–302, 2004.

[104] P. Abdel-Sayed *et al.*, "Anti-Microbial Dendrimers against Multidrug-Resistant P. aeruginosa Enhance the Angiogenic Effect of Biological Burn-wound Bandages," *Sci. Rep.*, vol. 6, no. 1, pp. 22020–22030, Apr. 2016.

[105] M. S. Bhave, A. M. Hassanbhai, P. Anand, K. Q. Luo, and H. S. Teoh, "Effect of Heat-Inactivated Clostridium sporogenes and Its Conditioned Media on 3-Dimensional Colorectal Cancer Cell Models," *Sci. Rep.*, vol. 5, no. 1, pp. 15681–15693, 2015.

[106] A. N. Bezbaruah and T. C. Zhang, "Fabrication of Anodically Electrodeposited Iridium Oxide Film pH Microelectrodes for Microenvironmental Studies," *Anal. Chem.*, vol. 74, no. 22, pp. 5726–5733, 2002.

[107] S. A. M. Marzouk, S. Ufer, R. P. Buck, T. A. Johnson, L. A. Dunlap, and W. E. Cascio, "Electrodeposited Iridium Oxide pH Electrode for Measurement of Extracellular

Myocardial Acidosis during Acute Ischemia," *Anal. Chem.*, vol. 70, no. 23, pp. 5054–5061, 1998.

[108] G. Beamson and D. Briggs, *High resolution XPS of organic polymers: The Scienta ESCA 300 database.*, vol. 20, no. 3. Wiley-Blackwell, 1992.

[109] J. S. Lee, D. H. Shin, and J. Jang, "Electronic Supplementary Information (ESI) for Polypyrrole-coated Manganese Dioxide with Multiscale Architectures for Ultrahigh Capacity energy storage," *Energy Environ. Sci.*, vol. 8, pp. 3030–3039, 2015.

[110] L. D. Renner and D. B. Weibel, "Physicochemical Regulation of Biofilm Formation.," *MRS Bull.*, vol. 36, no. 5, pp. 347–355, 2011.

[111] S. Khodaparast, M. K. Kim, J. E. Silpe, and H. A. Stone, "Bubble-Driven Detachment of Bacteria from Confined Microgeometries," *Environ. Sci. Technol.*, vol. 51, no. 3, pp. 1340–1347, Feb. 2017.

[112] M. Giladi *et al.*, "Microbial Growth Inhibition by Alternating Electric Fields," *Antimicrob. Agents Chemother.*, vol. 52, no. 10, pp. 3517–3522, 2008.

[113] P. Jain and S. Sinha, "Neutrophiles: Acid Challenge and Comparison with Acidophiles," *Internet J. Microbiol. T*, vol. 7, no. 1, pp. 1–10, 2008.

[114] M. M. Benjamin and A. R. Datta, "Acid Tolerance of Enterohemorrhagic Escherichia coli," *Appl. Environ. Microbiol.*, vol. 61, no. 4, pp. 1669–1672, 1995.

[115] P. C. Foller and C. W. Tobias, "The Anodic Evolution of Ozone," *J. Electrochem. Soc.*, vol. 129, no. 3, pp. 506–515, 1982.

[116] R. A. Barnes and A. L. Torres, "Electrochemical Concentration Cell Ozone Soundings at Two Sites during the Stratospheric Ozone Intercomparison Campaign," *J. Geophys. Res.*, vol. 100, no. D5, pp. 9245–9253, 1995.

[117] A. Kapałka, G. Fóti, and C. Comninellis, “The Importance of Electrode Material in Environmental Electrochemistry: Formation and Reactivity of Free Hydroxyl Radicals on Boron-Doped Diamond Electrodes,” *Electrochim. Acta*, vol. 54, no. 7, pp. 2018–2023, 2009.

[118] L. M. Da Silva, L. A. De Faria, and J. F. C. Boodts, “Electrochemical Ozone Production: Influence of the Supporting Electrolyte on Kinetics and Current Efficiency,” *Electrochim. Acta*, vol. 48, no. 6, pp. 699–709, 2003.

[119] Y. Yang and J. J. Pignatello, “Participation of the Halogens in Photochemical Reactions in Natural and Treated Waters,” *Molecules*, vol. 22, no. 10, pp. 1684–1708, 2017.

[120] D. Wu, D. Wong, and B. Di Bartolo, “Evolution of Cl_2 in Aqueous NaCl Solutions,” *J. Photochem.*, vol. 14, no. 4, pp. 303–310, 1980.

[121] X.-Y. Yu and J. R. Barker, “Hydrogen Peroxide Photolysis in Acidic Aqueous Solutions Containing Chloride Ions. I. Chemical Mechanism,” *J . Phys. Chem. A.*, vol. 107, no. 9, pp. 1313–1324, 2003.

[122] B. M. Matthew and C. Anastasio, “A Chemical Probe Technique for the Determination of Reactive Halogen Species in Aqueous Solution: Part 1 - Bromide Solutions,” *Atmos. Chem. Phys.*, vol. 6, no. 9, pp. 2423–2437, 2006.

[123] T. X. Wang and D. W. Margerum, “Kinetics of Reversible Chlorine Hydrolysis: Temperature Dependence and General-Acid/Base-Assisted Mechanisms,” *Inorg. Chem.*, vol. 33, no. 6, pp. 1050–1055, Mar. 1994.

[124] R. E. Connick, “The Interaction of Hydrogen Peroxide and Hypochlorous Acid in Acidic Solutions Containing Chloride Ion,” *J. Am. Chem. Soc.*, vol. 69, no. 6, pp. 1509–1514, Jun. 1947.

[125] T. Abee, L. Krockel, and C. Hill, “Bacteriocins: Modes of Action and Potentials in Food

Preservation and Control of Food Poisoning," *Int. J. Food Microbiol.*, vol. 28, no. 2, pp. 169–185, 1995.

[126] P. E. Granum, J. M. Tomas, and J. E. Alouf, "A Survey of Bacterial Toxins Involved in Food Poisoning: a Suggestion for Bacterial Food Poisoning Toxin Nomenclature," *Int. J. Food Microbiol.*, vol. 28, no. 2, pp. 129–144, 1995.

[127] Y. H. An and R. J. Friedman, "Concise Review of Mechanisms of Bacterial Adhesion to Biomaterial Surfaces," *J. Biomed. Mater. Res.*, vol. 43, no. 3, pp. 338–348, 1998.

[128] Q. Zhang, J. Nghiem, G. J. Silverberg, and C. D. Vecitis, "Semiquantitative Performance and Mechanism Evaluation of Carbon Nanomaterials as Cathode Coatings for Microbial Fouling Reduction," *Appl. Environ. Microbiol.*, vol. 81, pp. 4744–4755, 2005.

[129] I. Gall, M. Herzberg, and Y. Oren, "The Effect of Electric Fields on Bacterial Attachment to Conductive Surfaces," *Soft Matter*, vol. 9, no. 8, pp. 2443–2452, 2013.

[130] J. P. Busalmen, S. R. De Sánchez, and S. R. De Sa, "Electrochemical Polarization-Induced Changes in the Growth of Individual Cells and Bofilms of Pseudomonas Fluorescens (ATCC 17552)," *Appl. Environ. Microbiol.*, vol. 71, pp. 6235–6240, 2005.

[131] D. He, C. E. Wong, W. Tang, P. Kovalsky, and T. D. Waite, "Faradaic Reactions in Water Desalination by Batch-mode Capacitive Deionization," *Environ. Sci. Technol Lett.*, vol. 3, pp. 222–226, 2016.

[132] M.-H. Lin, S. Mehraeen, G. Cheng, C. Rusinek, and B. P. Chaplin, "The Role of Near Electrode Solution Chemistry on Bacteria Attachment and Inactivation at Low Applied Potentials," *Environ. Sci. Technol*, vol. 54, no. 1, pp. 446–455, 2020.

[133] H.-L. Alakomi, M. Saarela, and I. M. Helander, "Effect of EDTA on Salmonella Enterica Serovar Typhimurium Involves a Component not Assignable to Lipopolysaccharide

Release," *Microbiology*, vol. 149, no. 8, pp. 2015–2021, 2003.

[134] H. Mulcahy, L. Charron-Mazenod, and S. Lewenza, "Extracellular DNA Chelates Cations and Induces Antibiotic Resistance in Pseudomonas aeruginosa Biofilms," *PLoS Pathog.*, vol. 4, no. 11, p. e1000213 (1-12), Nov. 2008.

[135] K. J. Thomas and C. V. Rice, "Revised Model of Calcium and Magnesium Binding to the Bacterial Cell Wall," *BioMetals*, vol. 27, no. 6, pp. 1361–1370, 2014.

[136] S. K. Maier, S. Scherer, and M. J. Loessner, "Long-Chain Polyphosphate Causes Cell Lysis and Inhibits Bacillus Cereus Septum Formation, Which is Dependent on Divalent Cations," *Appl. Environ. Microbiol.*, vol. 65, no. 9, pp. 3942–3949, 1999.

[137] P. Corbisier *et al.*, "Whole Cell- and Protein-based Biosensors for the Detection of Bioavailable Heavy Metals in Environmental Samples," *Anal. Chim. Acta*, vol. 387, no. 3, pp. 235–244, 1999.

[138] D. J. R. Conroy, P. A. Millner, D. I. Stewart, and K. Pollmann, "Biosensing for the Environment and Defence: Aqueous Uranyl Detection using Bacterial Surface Layer Proteins," *Sensors*, vol. 10, no. 5, pp. 4739–4755, 2010.

[139] J. Maly *et al.*, "Immobilisation of Engineered Molecules on Electrodes and Optical Surfaces," *Mater. Sci. Eng. C*, vol. 22, no. 2, pp. 257–261, 2002.

[140] A. Loukanov, A. Angelov, Y. Takahashi, I. Nikolov, and S. Nakabayashi, "Carbon Nanodots Chelated with Metal Ions as Efficient Electrocatalysts for Enhancing Performance of Microbial Fuel Cell based on Sulfate Reducing Bacteria," *Colloids Surfaces A Physicochem. Eng. Asp.*, vol. 574, pp. 52–61, 2019.

[141] A. Y. Bhagirath, Y. Li, D. Somayajula, M. Dadashi, S. Badr, and K. Duan, "Cystic Fibrosis Lung Environment and Pseudomonas Aeruginosa Infection," *BMC Pulm. Med.*, vol. 16, no.

1, pp. 174–190, 2016.

[142] P. Gayen and B. P. Chaplin, “Fluorination of Boron-Doped Diamond Film Electrodes for Minimization of Perchlorate Formation,” *ACS Appl. Mater. Interfaces*, vol. 9, pp. 27638–27648, 2017.

[143] Y. Hong and D. G. Brown, “Alteration of Bacterial Surface Electrostatic Potential and pH upon Adhesion to A Solid Surface and Impacts to Cellular Bioenergetics,” *Biotechnol. Bioeng.*, vol. 105, no. 5, pp. 965–972, 2010.

[144] Y. Hong and D. G. Brown, “Electrostatic Behavior of the Charge-regulated Bacterial Cell Surface,” *Langmuir*, vol. 24, no. 9, pp. 5003–5009, 2008.

[145] H. . Frisch, M. J.; Trucks, G. W.; Schlegel, H. B.; Scuseria, G. E.; Robb, M. A.; Cheeseman, J. R.; Scalmani, G.; Barone, V.; Petersson, G. A.; Nakatsuji, “Gaussian 16 Rev. B.01. Wallingford, CT 2016.”

[146] A. V. Marenich, C. J. Cramer, and D. G. Truhlar, “Universal Solvation Model Based on Solute Electron Density and on a Continuum Model of the Solvent Defined by the Bulk Dielectric Constant and Atomic Surface Tensions,” *J. Phys. Chem. B*, vol. 113, no. 18, pp. 6378–6396, 2009.

[147] J. Lyklema, *Fundamentals of interface and colloid science: liquid-fluid interfaces*. Academic Press, 2000.

[148] A. Poortinga, R. Bos, and W. Norde, “Electric Double Layer Interactions in Bacterial Adhesion to Surfaces,” *Surf. Sci. Rep.*, vol. 47, no. 1, pp. 3–32, 2002.

[149] A. T. Poortinga, R. Bos, W. Norde, and H. J. Busscher, “Electric Double Layer Interactions in Bacterial Adhesion to Surfaces,” *Surf. Sci. Rep.*, vol. 47, no. 1, pp. 1–32, 2002.

[150] T. W. Healy and L. R. White, “Ionizable Surface Group Models of Aqueous Interfaces,”

Adv. Colloid Interface Sci., vol. 9, no. 4, pp. 303–345, 1978.

[151] R. J. Hunter, *Zeta potential in colloid science : principles and applications*. New York: Academic Press, 1981.

[152] Y.-I. Chang and C.-Y. Hsieh, "The Effect of Cationic Electrolytes on the Electrophoretic Properties of Bacterial Cells," *Colloids and Surfaces*, vol. 53, no. 1, pp. 21–31, 1991.

[153] W. Richard, D. Evrard, and P. Gros, "Kinetic Study of Redox Probes on Glassy Carbon Electrode Functionalized by 4-nitrobenzene Diazonium," *Int. J. Electrochem. Sci*, vol. 14, pp. 453–469, 2019.

[154] P. Chen and R. L. McCreery, "Control of Electron Transfer Kinetics at Glassy Carbon Electrodes by Specific Surface Modification," *Anal. Chem.*, vol. 68, no. 22, pp. 3958–3965, 1996.

[155] Y. Hong and D. G. Brown, "Cell Surface Acid–Base Properties of Escherichia coli and Bacillus brevis and Variation as a Function of Growth Phase, Nitrogen source and C:N ratio," *Colloids Surfaces B Biointerfaces*, vol. 50, no. 2, pp. 112–119, 2006.

[156] N. H. Lam, Z. Ma, and B.-Y. Ha, "Electrostatic Modification of the Lipopolysaccharide Layer: Competing Effects of Divalent Cations and Polycationic or Polyanionic Molecules," *Soft Matter*, vol. 10, no. 38, pp. 7528–7544, 2014.

[157] A. T. Poortinga, R. Bos, and H. J. Busscher, "Electrostatic Interactions in the Adhesion of an Ion-penetrable and Ion-impenetrable Bacterial Strain to Glass," *Colloids Surfaces B Biointerfaces*, vol. 20, no. 2, pp. 105–117, 2001.

[158] P. L. Mccarty, J. Bae, and J. Kim, "Domestic Wastewater Treatment as a Net Energy Producer-Can This be Achieved?," *Environ. Sci. Technol*, vol. 45, pp. 7100–7106, 2011.

[159] C. H. Comninellis and C. Pulgarin, "Anodic Oxidation of Phenol for Waste Water

Treatment," *J. Appl. Electrochem.*, vol. 21, pp. 703–708, 1991.

[160] C. A. Martínez-Huitle and S. Ferro, "Electrochemical Oxidation of Organic Pollutants for the Wastewater Treatment: Direct and Indirect Processes," *Chem. Soc. Rev.*, vol. 35, pp. 1324–1340, 2006.

[161] E. Brillas and I. Sirés, "Electrochemical Removal of Pharmaceuticals from Water Streams: Reactivity Elucidation by Mass Spectrometry," *TrAC Trends Anal. Chem.*, vol. 70, pp. 112–121, 2015.

[162] C. E. Schaefer *et al.*, "Electrochemical Transformations of Perfluoroalkyl Acid (PFAA) Precursors and PFAAs in Groundwater Impacted with Aqueous Film Forming Foams," *Environ. Sci. Technol.*, vol. 52, no. 18, pp. 10689–10697, 2018.

[163] C. E. Schaefer, C. Andaya, A. Urtiaga, E. R. Mckenzie, and C. P. Higgins, "Electrochemical Treatment of Perfluorooctanoic Acid (PFOA) and Perfluorooctane Sulfonic Acid (PFOS) in Groundwater Impacted by Aqueous Film Forming Foams (AFFFs)," *J. Hazard. Mater.*, vol. 295, pp. 170–175, 2015.

[164] A. Y. Bagastyo, D. J. Batstone, I. Kristiana, W. Gernjak, C. Joll, and J. Radjenovic, "Electrochemical Oxidation of Reverse Osmosis Concentrate on Boron-Doped Diamond Anodes at Circumneutral and Acidic pH," *Water Res.*, vol. 46, no. 18, pp. 6104–6112, 2012.

[165] A. Y. Bagastyo, D. J. Batstone, K. Rabaey, and J. Radjenovic, "Electrochemical Oxidation of Electrodialysed Reverse Osmosis Concentrate on Ti/Pt-IrO_2, Ti/SnO_2-Sb and Boron-Doped Diamond Electrodes," *Water Res.*, vol. 47, no. 1, pp. 242–250, 2013.

[166] D. K. Hubler, J. C. Baygents, B. P. Chaplin, and J. Farrell, "Understanding Chlorite and Chlorate Formation Associated with Hypochlorite Generation at Boron Doped Diamond Film Anodes," *J. Electrochem. Soc.*, vol. 161, no. 12, pp. E182–E189, 2014.

[167] Environmental Protection Agency (EPA), “National Primary Drinking Water Regulations: Proposed Perchlorate Rule,” 2018.

[168] D. of E. P. Massachusetts, “Drinking Water Standard for Perchlorate,” 2006.

[169] D. of T. and S. California, “Perchlorate Maximum Contaminant Level (MCL) Review,” 2015.

[170] C. Trellu *et al.*, “Electro-oxidation of Organic Pollutants by Reactive Electrochemical Membranes,” *Chemosphere*, vol. 208, pp. 159–175, 2018.

[171] A. M. Zaky and B. P. Chaplin, “Porous Substoichiometric TiO_2 Anodes as Reactive Electrochemical Membranes for Water Treatment,” *Environ. Sci. Technol.*, vol. 47, no. 12, pp. 6554–6563, 2013.

[172] A. M. Zaky and B. P. Chaplin, “Mechanism of p-Substituted Phenol Oxidation at a Ti_4O_7 Reactive Electrochemical Membrane,” *Environ. Sci. Technol.*, vol. 48, no. 10, pp. 5857–5867, May 2014.

[173] P. Gayen, C. Chen, J. T. Abiade, and B. P. Chaplin, “Electrochemical Oxidation of Atrazine and Clothianidin on Bi-doped SnO 2 -Ti_nO_{2n-1} Electrocatalytic Reactive Electrochemical Membranes,” *Environ. Sci. Technol.*, vol. 52, no. 21, pp. 12675–12684, Nov. 2018.

[174] S. N. Misal, M. H. Lin, S. Mehraeen, and B. P. Chaplin, “Modeling Electrochemical Oxidation and reduction of sulfamethoxazole using electrocatalytic reactive electrochemical membranes,” *J. Hazard. Mater.*, vol. 384, pp. 1–12, Feb. 2020.

[175] P. Cañizares, F. Martínez, M. Díaz, J. García-Gómez, and M. A. Rodrigo, “Electrochemical Oxidation of Aqueous Phenol Wastes Using Active and Nonactive Electrodes,” *J. Electrochem. Soc.*, vol. 149, no. 8, pp. D118–D124, Jun. 2002.

[176] H. Nady, M. M. El-Rabiei, and G. M. A. El-Hafez, “Electrochemical Oxidation Behavior

of Some Hazardous Phenolic Compounds in Acidic Solution," *Egypt. J. Pet.*, vol. 26, no. 3, pp. 669–678, 2017.

[177] T. A. Enache and A. M. Oliveira-Brett, "Phenol and Para-substituted Phenols Electrochemical Oxidation Pathways," *J. Electroanal. Chem.*, vol. 655, no. 1, pp. 9–16, 2011.

[178] S. Nayak and B. P. Chaplin, "Fabrication and Characterization of Porous, Conductive, Monolithic Ti_4O_7 Electrodes," *Electrochim. Acta*, vol. 263, pp. 299–310, 2018.

[179] S. Almassi, Z. Li, W. Xu, C. Pu, T. Zeng, and B. P. Chaplin, "Simultaneous Adsorption and Electrochemical Reduction of N-Nitrosodimethylamine Using Carbon-Ti_4O_7 Composite Reactive Electrochemical Membranes," *Environ. Sci. Technol.*, vol. 53, no. 2, pp. 928–937, 2019.

[180] D. Snoeyink, Vernon L., Jenkins, *Water Chemistry*. John Wiley and Sons: New York, 1980.

[181] T. Mikolajczyk, B. Pierozynski, L. Smoczynski, and W. Wiczkowski, "Electrodegradation of Resorcinol on Pure and Catalyst-Modified in Foam Anodes, Studied under Alkaline and Neutral pH Conditions," *Molecules*, vol. 23, no. 6, pp. 1293–1304, 2018.

[182] R. L. Yates and D. C. Havery, "Determination of Phenol, Resorcinol, Salicylic Acid and α-Hydroxy Acids in Cosmetic Products and Salon Preparations," *J. Cosmet. Sci.*, vol. 50, no. 5, pp. 315–325, 1999.

[183] HACH, "Chemical Oxygen Demand, Dichromate Method," 2014.

[184] Y. Zhao and D. G. Truhlar, "The M06 Suite of Density Functionals for Main Group Thermochemistry, Thermochemical Kinetics, Noncovalent Iinteractions, Excited States, and Transition Elements: Two New Functionals and Systematic Testing of Four M06-class Functionals and 12 Other Functionals," *Theor. Chem. Acc.*, vol. 120, no. 1–3, pp. 215–241,

2008.

[185] A. V. Marenich, C. J. Cramer, and D. G. Truhlar, “Universal Solvation Model Based on Solute Electron Density and on a Continuum Model of the Solvent Defined by the Bulk Dielectric Constant and Atomic Surface Tensions,” *J. Phys. Chem. B*, vol. 113, no. 18, pp. 6378–6396, 2009.

[186] Y. Jing and B. P. Chaplin, “Mechanistic Study of the Validity of Using Hydroxyl Radical Probes to Characterize Electrochemical Advanced Oxidation Processes,” *Environ. Sci. Technol.*, vol. 51, no. 4, pp. 2355–2365, 2017.

[187] C. P. Kelly, C. J. Cramer, and D. G. Truhlar, “Aqueous Solvation Free Energies of Ions and Ion-water Clusters Based on An Accurate Value for the Absolute Aqueous Solvation Free Energy of the Proton,” *J. Phys. Chem. B*, vol. 110, no. 32, pp. 16066–16081, 2006.

[188] M. D. Tissandier *et al.*, “The Proton’s Absolute Aqueous Enthalpy and Gibbs Free Energy of Solvation from Cluster-ion Solvation Data,” *J. Phys. Chem. A*, vol. 102, no. 40, pp. 7787–7794, 1998.

[189] A. J. Bard and L. R. Faulkner, *Electrochemical Methods: Fundamentals and Applications, 2nd Edition | Wiley*, Second. John Wiley and Sons, 2001.

[190] V. Vaissier, P. Barnes, J. Kirkpatrick, and J. Nelson, “Influence of Polar Medium on the Reorganization Energy of Charge Transfer between Dyes in a Dye Sensitized Film,” *Phys. Chem. Chem. Phys.*, vol. 15, no. 13, pp. 4804–4814, Apr. 2013.

[191] A. Donaghue and B. P. Chaplin, “Effect of Select Organic Compounds on Perchlorate Formation at Boron-doped Diamond Film Anodes,” *Environ. Sci. Technol.*, vol. 47, no. 21, pp. 12391–12399, 2013.

[192] J. J. Rook, “Chlorination Reactions of Fulvic Acids in Natural Waters,” *Environ. Sci.*

Technol., vol. 11, no. 5, pp. 478–482, 1977.

[193] N. Y. Tretyakova, A. T. Lebedev, and V. S. Petrosyan, "Degradative Pathways for Aqueous Chlorination of Orcinol," *Environ. Sci. Technol.*, vol. 28, no. 4, pp. 606–613, 1994.

[194] D. E. Jackson, R. A. Larson, and V. L. Snoeyink, "Reactions of Chlorine and Chlorine Dioxide with Resorcinol in Aqueous Solution and Adsorbed on Granular Activated Carbon," *Water Res.*, vol. 21, no. 7, pp. 849–857, 1987.

[195] F. Ge, L. Zhu, and H. Chen, "Effects of pH on the Chlorination Process of Phenols in Drinking Water," *J. Hazard. Mater.*, vol. 133, no. 1–3, pp. 99–105, 2006.

[196] S. Tak and B. Prakash Vellanki, "Natural Organic Matter as Precursor to Disinfection Byproducts and its Removal using Conventional and Advanced Processes: State of the Art Review," *J. Water Heal.*, vol. 16, no. 5, pp. 681–703, 2018.

[197] A. A. Hussein *et al.*, "Mechanistic Investigations on Pinnick Oxidation: A Density Functional Theory Study," *R. Soc. Open Sci.*, vol. 7, no. 2, p. 191568, 2020.

[198] M. Nihemaiti, J. Le Roux, C. Hoppe-Jones, D. A. Reckhow, and J.-P. Croué, "Formation of Haloacetonitriles, Haloacetamides, and Nitrogenous Heterocyclic Byproducts by Chloramination of Phenolic Compounds," *Phenolic Compd. Environ. Sci. Technol. Am. Chem. Soci-ety*, vol. 51, no. 1, pp. 655–663, 2017.

[199] K. H. J Air Pollut, S. D. Boyce, and J. F. Hornlg, "Reaction Pathways of Trihalomethane Formation from the Halogenation of Dihydroxyaromatic Model Compounds for Humic Acid," *Anal. Tech. Environ. Chem-istry II*, vol. 17, no. 37, pp. 297–309, 1983.

[200] G. V. Buxton, C. L. Greenstock, W. P. Helman, and A. B. Ross, "Critical Review of Rate Constants for Reactions of Hydrated Electrons, Hydrogen Atoms and Hydroxyl Radicals (·OH/·O− in Aqueous Solution," *J. Phys. Chem. Ref. Data*, vol. 17, no. 2, pp. 513–886,

1988.

[201] T. A. Enache and A. M. Oliveira-Brett, “Phenol and Para-substituted Phenols Electrochemical Oxidation Pathways,” *J. Electroanal. Chem.*, vol. 655, no. 1, pp. 9–16, 2011.

[202] B. Nasr, G. Abdellatif, P. Cañizares, C. Sáez, J. Lobato, and M. A. Rodrigo, “Electrochemical Oxidation of Hydroquinone, Resorcinol, and Catechol on Boron-Doped Diamond Snodes,” *Environ. Sci. Technol.*, vol. 39, no. 18, pp. 7234–7239, 2005.

[203] E. Oturan, N. Oturan, and M. A. Oturan, “An Unprecedented Route of OH Radical Reactivity Evidenced by An Electrocatalytical Process: Ipso-substitution with Perhalogenocarbon Compounds,” *Appl. Catal. B Environ.*, vol. 226, pp. 135–146, 2018.

[204] S. Almassi, P. R. V. Samonte, Z. Li, W. Xu, and B. P. Chaplin, “Mechanistic Investigation of Haloacetic Acid Reduction using Carbon-Ti_4O_7 Composite Reactive Eelectrochemical Membranes,” *Environ. Sci. Technol.*, vol. 54, no. 3, pp. 1982–1991, 2020.

[205] E. Segev *et al.*, “Dynamic Metabolic Exchange Governs a Marine Algal-Bacterial Interaction,” *Elife*, vol. 5, pp. 1–28, 2016.

[206] M. Rosenbaum, Z. He, and L. T. Angenent, “Light Energy to Bioelectricity: Photosynthetic Microbial Fuel cells,” *Current Opinion in Biotechnology*, vol. 21, no. 3. pp. 259–264, 2010.

[207] T. Yasukawa, T. Kaya, and T. Matsue, “Imaging of Photosynthetic and Respiratory Activities of a Single Algal Protoplast by Scanning Electrochemical Microscopy,” *Chem. Lett.*, vol. 28, no. 9, pp. 975–976, Sep. 1999.

[208] K. Mckelvey, S. Martin, C. Robinson, and P. R. Unwin, “Quantitative Local Photosynthetic Flux Measurements at Isolated Chloroplasts and Thylakoid Membranes Using Scanning Electrochemical Microscopy (SECM) Molecular Assembly and Organisation in Cells

(MOAC) Doctoral Training Centre," *J. Phys. Chem. B*, vol. 117, pp. 7878–7888, 2013.

[209] A. Badura *et al.*, "Photo-induced Electron Transfer between Photosystem 2 via Cross-linked Redox Hydrogels," *Electroanalysis*, vol. 20, no. 10, pp. 1043–1047, 2008.

[210] B. E. Logan *et al.*, "Microbial Fuel Cells: Methodology and Technology," *Environmental Science and Technology*, vol. 40, no. 17. 2006.

[211] G. Longatte *et al.*, "Investigation of Photocurrents Resulting from a Living Unicellular Algae Suspension with Quinones Over Time," *Chem. Sci.*, vol. 9, pp. 8271–8281, 2018.

[212] M. H. Lin, S. Mehraeen, G. Cheng, C. Rusinek, and B. P. Chaplin, "Role of Near-Electrode Solution Chemistry on Bacteria Attachment and Poration at Low Applied Potentials," *Environ. Sci. Technol.*, vol. 54, pp. 446–455, 2020.

[213] ThermoFisher, "SYTOX® Green Nucleic Acid Stain Protocol - US."

[214] G. Longatte, F. Rappaport, F.-A. Wollman, M. Guille-Collignon, and F. Lemaître, "Mechanism and Analyses for Extracting Photosynthetic Electrons using Exogenous Quinones – What Makes a Good Extraction pathway?," *Photochem. Photobiol. Sci.*, vol. 15, no. 8, pp. 969–979, 2016.

[215] J. Xing *et al.*, "Antimicrobial Peptide Functionalized Conductive Nanowire Array Electrode as a Promising Candidate for Bacterial Environment Application," *Adv. Funct. Mater.*, vol. 29, no. 23, p. 1806353, Jun. 2019.

[216] M. Tolba, M. U. Ahmed, C. Tlili, F. Eichenseher, M. J. Loessner, and M. Zourob, "A Bacteriophage Endolysin-based Electrochemical Impedance Biosensor for the Rapid Detection of Listeria Cells," *Analyst*, vol. 137, pp. 5749–5756, 2012.

[217] Y. Xu, X. Xie, Y. Duan, L. Wang, Z. Cheng, and J. Cheng, "A Review of Impedance Measurements of Whole Cells," *Biosens. Bioelectron.*, vol. 77, pp. 824–836, 2016.

[218] M. Grossi and B. Riccò, “Electrical Impedance Spectroscopy (EIS) for Biological Analysis and Food Characterization: A Review,” *J. Sensors Sens. Syst.*, vol. 6, no. 2, pp. 303–325, 2017.

[219] A. Santos, “Fundamentals and Applications of Impedimetric and Redox Capacitive Biosensors,” *J. Anal. Bioanal. Tech.*, vol. S7, no. 12, pp. 1–15, 2014.

[220] W. Mohd, E. Mustaqim, M. Daniyal, S. Saleviter, and Y. W. Fen, “Development of Surface Plasmon Resonance Spectroscopy for Metal Ion Detection,” *Sensors Mater.*, vol. 30, no. 9, pp. 2023–2038, 2018.

[221] P. Sondhi, M. H. U. Maruf, and K. J. Stine, “Nanomaterials for Biosensing Lipopolysaccharide,” *Biosensors*, vol. 10, no. 1. p. 2, 2020.

[222] M. J. Knape *et al.*, “Divalent Metal Ions Mg^{2+} and Ca^{2+} Have Distinct Effects on Protein Kinase A Activity and Regulation,” *ACS Chem. Biol*, vol. 01, p. 8, 2015.

[223] S. O. Hagge, M. U. Hammer, A. Wiese, U. Seydel, and T. Gutsmann, “Calcium Adsorption and Displacement: Characterization of Lipid Monolayers and Their Interaction with Membrane-Active Peptides/Proteins,” *BMC Biochem.*, vol. 7, pp. 1–13, 2006.

[224] J. Jiang, X. Zhang, X. Zhu, and Y. Li, “Removal of Intermediate Aromatic Halogenated DBPs by Activated Carbon Adsorption: A New Approach to Controlling Halogenated DBPs in Chlorinated Drinking Water,” *Environ. Sci. Technol.*, vol. 51, no. 6, pp. 3435–3444, 2017.

[225] H. Sakamoto, J. Imai, Y. Shiraishi, S. Tanaka, S. Ichikawa, and T. Hirai, “Photocatalytic Dehalogenation of Aromatic Halides on Ta_2O_5-Supported Pt-Pd Bimetallic Alloy Nanoparticles Activated by Visible Light,” *ACS Catal.*, vol. 7, no. 8, pp. 5194–5201, 2017.

[226] A. Elhage, P. Costa, A. Nasim, A. E. Lanterna, and J. C. Scaiano, “Photochemical

Dehalogenation of Aryl Halides: Importance of Halogen Bonding," *J. Phys. Chem. A*, vol. 123, no. 47, pp. 10224–10229, 2019.

[227] Y.-P. Li, H.-B. Cao, and Y. Zhang, "Reductive Dehalogenation of Haloacetic Acids by Hemoglobin-Loaded Carbon Nanotube Electrode," *Water Res.*, vol. 41, pp. 197–205, 2007.

[228] Y. Li *et al.*, "Reductive Dehalogenation of Disinfection Byproducts by An Activated Carbon-based Electrode System," *Water Res.*, vol. 98, pp. 354–362, 2016.

[229] A. K. Zeraatkar, H. Ahmadzadeh, A. F. Talebi, N. R. Moheimani, and M. P. Mchenry, "Potential Use of Algae for Heavy Metal Bioremediation, A Critical Review," *J. enviroment Manag.*, vol. 181, pp. 817–831, 2016.

[230] R. Tu, W. Jin, T. Xi, Q. Yang, S.-F. Han, and E.-F. Abomohra, "Effect of Static Magnetic Field on the Oxygen Production of Scenedesmus Obliquus Cultivated in Municipal Wastewater," *Water Res.*, vol 86, pp132-138, 2015.

[231] C. Park, C. L.-N. Vo, T. Kang, E. Oh, and B.-J. Lee, "New Method and Characterization of Self-assembled Gelatin–oleic Nanoparticles using a Desolvation Method via Carbodiimide/N-hydroxysuccinimide (EDC/NHS) Reaction," *Eur. J. Pharm. Biopharm.*, vol. 89, pp. 365–373, 2015.

[232] M. K. Walsh, X. Wang, and B. C. Weimer, "Optimizing the Immobilization of Single-Stranded DNA onto Glass Beads," *J. Biochem. Biophys. Methods*, vol. 47, pp. 221–231, 2001.

CV/VITA

Meng-Hsuan (Irene) Lin

mlin40@uic.edu

EDUCATION

University of Illinois at Chicago (UIC) — Chicago, IL
Ph.D. Candidate, Chemical Engineering — **Expected: July 2020**
Dissertation: Environmental Effects of Bacteria, Algae, and Biomolecules on Electrode Surfaces

National Yang Ming University — Taipei, Taiwan
Master of Science, Biomedical Engineering — May 2013
Thesis: Drug Vehicle with Multimodal Imaging Functionality

Chung Yuan Christian University — Taoyuan, Taiwan
Bachelor of Science, Chemical Engineering — May 2011

ACADEMIC EXPERIENCE

UIC Chemical Engineering Department-Chaplin Lab (Electrochemistry & Water treatment)
Chicago, IL
PhD Researcher and Teaching Assistant — *2015-Current*

- Studied the mechanisms of biofilm control and bacteria inactivation on electrode surfaces for water treatment applications.
- Conducted research focused on chlorinated byproduct formation at Magnéli phase Ti_4O_7 electrodes during electrochemical advanced oxidation processes.
- Developed methods to study algae viability at a boron-doped diamond (BDD) electrode surface under different environmental conditions using photosynthetic activity monitoring.
- Instructed thermodynamics discussion classes for ~35 undergrad students.

National Yang Ming University-Nano-Biomaterial Research Lab (Drug delivery)
Taipei, Taiwan
Department of Biomedical Engineering, Master's Researcher — *2011-2013*

- Studied multi-functional drug carrier design for cervical cancer treatment, which combined magnetic targeting, ultrasound diagnose and drug release.
- Studied the size control, preparation and properties of polymersome, micelle and albumin-based microbubble for drug efficient enhancement at tumor angiogenesis.
- Synthesized inorganic zinc oxide (~100 nm) and lipophilic superparamagnetic iron oxide (~10 nm) nanoparticles as quantum dots for magnetic resonance purposes and hydrophobic drug loading.
- Operated in vitro and in vivo (nude mice) MRI and histochemistry stain for cervical cancer and drug internal circulation studies.

Chung Yuan Christian University-R&D Center for Membrane Technology
Taoyuan, Taiwan
Department of Chemical Engineering, Undergraduate Researcher — *2009-2011*

- Studied the membrane selectivity of CO_2/N_2 by gas chromatography.

- Controlled and characterized the pore structure of SiOCH films deposited from Octamethylcyclotetrasiloxane (OMCTS) on the commercial cellulose membrane by plasma polymerization technique with PECVD.

WORKING EXPERIENCE

National Taiwan University Taipei, Taiwan
Department of Chemical Engineering, Teaching Staff *2014-2015*

- Instructor, Unit Operation Lab courses for ~100 senior undergraduate students.
- Organized NTU alumni activities and fundraising.

Chunghwa Chemical & Pharmaceutical Co. Ltd. Hsinchu, Taiwan
R&D Researcher *2013-2014*

- Conducted hematology and antihistamine generic drugs analysis including drug assay, uniformities, impurities, dissolution and water content for quality control and batch manufacture purposes.

Taipei Medical University Hospital Taipei, Taiwan
Division of Rehabilitation Medicine, Research Assistant (Intern) *Summer 2013*

- Recorded electroencephalography (EEG) and MRI data from patients' brains during simple exercise (treadmill and indoor fitness) to assist in melancholia studies.
- Conducted tender point test for fibromyalgia syndrome patients for recovery record.

SKILLS

Laboratory Instrument Operation & Analysis

- High-performance liquid chromatography (HPLC), Ion chromatography (IC), Gas chromatography (GC)
- X-ray photoelectron spectroscopy (XPS), Transmission electron microscopy (TEM), Scanning electron microscope (SEM), Scanning electrochemical microscopy (SECM), Atomic force microscopy (AFM)
- Fourier-transform infrared spectroscopy (FTIR), Differential scanning calorimetry (DSC), UV-vis, Thermogravimetric analysis (TGA), Nuclear magnetic resonance (NMR), X-ray powder diffraction (XRD), Energy Dispersive X-ray Spectroscopy (EDS)
- Enzyme-linked immunosorbent assay (ELISA), Cytoviva, Confocal
- Chemical oxygen demand (COD), Electroencephalography (EEG), Plasma-enhanced chemical vapor deposition (PECVD)

Animal, Cell and Bacteria Operation

- Nude mice tail injection, Tumor-induced, Restraint, Anesthesia and Sacrifice
- Bacteria and cell culture, (3-(4,5-Dimethylthiazol-2-yl)-2,5-Diphenyltetrazolium Bromide) (MTT) assay for metabolism activity determination, Reactive oxygen species (ROS) detection, and Lactate dehydrogenase (LDH) analysis

Pharmaceutical and Chemical Process

- Drug assay, Uniformities, Impurities, Dissolution and Water content.
- Inorganic nanoparticles synthesis and Chemical polymer grafting.

PUBLICATIONS

1. **M-H. Lin**, D. M. Bulman, C. K. Remucal and Brian P. Chaplin,"Organic and Inorganic Chlorine-containing Byproduct Formation during the Electrochemical Advanced Oxidation Process at Magnéli Phase Ti4O7 Electrodes" (Submitted)
2. **M-H. Lin**, S. Mehraeen, G. Cheng, C. Rusinek, and B. P. Chaplin, "Bacteria Poration on Modified Boron-Doped Diamond Electrode Surfaces Induced by Divalent Cation Chelation" Environ. Sci.: Water Res. Technol., 2020
3. **M-H. Lin**, S. Mehraeen, G. Cheng, C. Rusinek, and B. P. Chaplin, "The Role of Near Electrode Solution Chemistry on Bacteria Attachment and Poration at Low Applied Potentials" Environ Sci Technol, 2020, 54, 446−455.
4. S. Misal, **M-H. Lin**, S. Mehraeen, and B. P. Chaplin, "Modeling Electrochemical Oxidation and Reduction of Sulfamethoxazole using Electrocatalytic Reactive Electrochemical Membranes" J. Hazard. Mater, 384, 121420 p1-12, 2020.
5. A. Pendse, S. Cetindag, **M-H. Lin** et.al "Charged Layered Boron Nitride-Nanoflake Membranes for Efficient Ion Separation and Water Purification" Small, 1904590 p1-8, 2019 (***Selected as cover page***)
6. T-Y. Liu, M-Y. Wu, **M-H. Lin**, and F-Y. Yang, "A novel ultrasound-triggered drug vehicle with multimodal imaging functionality" Acta Biomaterialia, 9(3), 5453-5463, 2013.
7. C-H. Lo, **M-H. Lin**, K-S. Liao, M. De Guzman, H-A. Tsai, V. Rouessac, T-C. Wei, K-R. Lee, and J-Y. Lai, "Control of pore structure and characterization of plasma-polymerized SiOCH films deposited from octamethylcyclotetrasiloxane (OMCTS)" Journal of Membrane Science, 365, (1–2), 418-425, 2010.